Title
An Experimental Investigation of High-Velocity Non-Spherical Polydisperse Particle-Laden Flows

Author
Li, Alice Kate

Publication Date
2020

UNIVERSITY OF CALIFORNIA,
IRVINE

AN EXPERIMENTAL INVESTIGATION OF HIGH-VELOCITY NON-SPHERICAL POLYDISPERSE PARTICLE-LADEN FLOWS

THESIS

submitted in partial satisfaction of the requirements for the degree of

MASTER OF SCIENCE
in Mechanical and Aerospace Engineering

by
ALICE KATE LI

Thesis Committee:

PROFESSOR G. SCOTT SAMUELSEN, CHAIR

PROFESSOR FARYAR JABBARI

PROFESSOR VINCENT G. MCDONELL

2020

DEDICATION

To the Li fam, friends, and a Bes.

TABLE OF CONTENTS

LIST OF FIGURES vi

LIST OF TABLES x

ACRONYMS xi

ACKNOWLEDGEMENTS ii

ABSTRACT OF THE THESIS iii

1. INTRODUCTION 1
   - 1.1 Overview 1
   - 1.2 Goal 2
   - 1.3 Objectives 2

2. BACKGROUND 3
   - 2.1 Turbomachinery Studies 3
   - 2.2 Potentials of Real-Time Sensor Implementation 4
   - 2.3 Previous Sensor Development 5
   - 2.4 Previous High-Velocity Dust-Laden Facilities 6
   - 2.5 Particle-Laden Flow Studies 6
   - 2.6 Methods for Characterizing Particles in Particle-Laden Flows 7
   - 2.7 Methods for Particle Sizing 8
   - 2.8 The Challenge of Sizing Non-Spherical Particles 8
   - 2.9 Summary 9

3. APPROACH 10

4. METHODOLOGY 14
   - 4.1 Test Dust Contaminant 14
   - 4.2 Equations Governing Particle-Laden Flows 16
   - 4.2.1 Pneumatic Dilute-Phase Solids Conveying 16
   - 4.3 Experimental Setup 18
   - 4.3.1 Generating High-Velocity Flow 19
   - 4.3.2 Particle Ingestion 20

4.3.3 Sensitivity of Particle Size Distribution to Particle Feeding 22
4.4 Laser Diagnostics Setup 23
4.4.1 Malvern Insitec ST97 Laser Diffraction System 26
4.4.1.1 Refractive Index Sensitivity 26
4.4.2 Sympatec HELOS 28
4.4.3 Nominal Particle Size Distribution Data 29
4.4.4 Laser Diffraction Limitations 33
4.5 Design of Experiments 34
4.5.1 DoE1- Screening DoE 36
4.5.2 DoE2 – Response Surface with Malvern Insitec ST97 40
4.5.3 DoE3 – Response Surface with Sympatec 42
4.5.4 Particle Ingestion through Side Wall 43
4.5.5 Reduced Rig Diameter 43
4.5.6 Data Acquisition and Model Selection 44
4.5.7 Uncontrollable Factors 46
4.6 Rig Plume Imaging 47
4.7 Evaluation of Forces Acting on a Particle in an Air Stream 47
5. RESULTS AND DISCUSSION 51
5.1 Single-Phase Flow Validations 51
5.2 DoE1 – Screening Factors 55
5.2.1 Factors Governing Dv10, Dv50, and Dv90 56
5.2.2 Factors Governing D32 59
5.2.3 Factors Governing Transmission 61
5.2.4 Outcomes of DoE1 65
5.3 DoE2 – Response Surface with Malvern Insitec ST97 67
5.3.1 Factors Governing Transmission Higher Loads 68
5.3.2 Factors Governing Dv10, Dv50, and Dv90 Higher Loads 70
5.3.3 Factors Governing D32 and D43 at Higher Loads 74
5.3.4 DoE2 Particle Size Distributions 77

5.4 DoE3 – Response Surface with Sympatec HELOS 81
5.4.1 Factors Governing Transmission at Lower Loads 82
5.4.2 Factors Governing Particle Sizes at Lower Loads 83
5.4.3 DoE3 Particle Size Distributions 85
5.4.4 Mie Theory and Fraunhofer Theory Particle Size Distribution Comparisons .90
5.5 Horizontal Particle Injection 92
5.5.1 Factors Governing Transmission 92
5.5.2 Factors Governing Dv10, Dv50, and Dv90 94
5.5.3 Factors Governing D32 and D43 98
5.6 Particle Size Distributions for Horizontal Particle Injection 100
5.7 Reduced Rig Diameter 103
5.8 Imaging Rig Exit Profile 106
5.9 Evaluation of Forces Acting on Particle in Air Stream 107
6. SUMMARY, CONCLUSIONS, RECOMMENDATIONS 116
6.1 Summary 116
6.2 Conclusions 118
6.3 Recommendations 120
REFERENCES 121
APPENDIX 126

LIST OF FIGURES

Figure 1. First stage turbine blade degradation from particulate ingestion [13]. 4
Figure 2. Leading edge erosion of a NASA DC-8-72 after volcanic eruption encounter. 4
Figure 3. Cumulative particle size distribution of AMTD and AFRL 03......15
Figure 4. Microscopic image of polydisperse AMTD......16
Figure 5. Microscopic image of 75 μm glass beads......16
Figure 6. Saltation velocities for various particle diameters, mass loadings of Φ = 2 and Φ = 15, and pipe diameters of D = 1 inch, and D 0.75 inch. 18
Figure 7. High-velocity particle-ingestion experimental rig. 20
Figure 8. Eductor flow. 21
Figure 9. Path of light upon encountering a particle. Line type selected does not signify any light phenomena. 25
Figure 10. Laser diffraction illustration. 25
Figure 11. Scattering angle for large and small particles. Adapted from Malvern Insitec RTSizer manual......25
Figure 12. PSD of test dust for varying real refractive index coefficients. 27
Figure 13. PSD of test dust for varying imaginary refractive index coefficients. 27
Figure 14. PSD of procured AMTD using Microtrac S3500. 30
Figure 15. Particle size distribution from two dispersion units: Microtrac and Sympatec. 31
Figure 16. Higher and lower level laser beam location for DoE1. 39
Figure 17. Three levels of laser beam location for DoE2, with 10 mm diameter beam. 41
Figure 18. Three levels of laser beam location for DoE3, with 12.8 mm diameter beam. 43
Figure 19. Horizontal velocity profile......52
Figure 20. Vertical velocity profile. 52
Figure 21. Vertical velocity profile for various mean velocities......54
Figure 22. Normalized vertical velocity profiles for various mean velocities. 54
Figure 23. Predicted versus actual Dv10 model points. 58
Figure 24. Predicted versus actual Dv50 model points. 58
Figure 25. Main effect plot of Dv10 versus flow velocity. 58
Figure 26. Main effect plot of Dv10 versus particle feed rate. 58
Figure 27. Main effect plot of Dv10 versus laser beam location. 58

Figure 28. Interaction plot of particle distribution median for combinations of flow velocity and laser beam location. 59
Figure 29. Predicted versus actual D32 model points. 60
Figure 30. Interaction plot of D32 for combinations of flow velocity and laser beam location. 60
Figure 31. Interaction plot of D32 for combinations of eductor pressure and rig length. 60
Figure 32. Predicted versus actual transmission model points. 63
Figure 33. Main effect plot of transmission versus feed rate. 63
Figure 34. Main effect plot of transmission versus eductor pressure. 63
Figure 35. Interaction plot of transmission for combinations of flow velocity and laser beam location. 64
Figure 36. Predicted versus actual transmission model points. 69
Figure 37. Main effect plot of transmission versus flow velocity. 69
Figure 38. Main effect plot of transmission versus laser beam location. 69
Figure 39. Main effect plot of transmission and particle feed rate. 69
Figure 40. Predicted versus actual Dv10 model points. 70
Figure 41. Interaction plot of Dv10 for combinations of flow velocity and laser beam location. 71
Figure 42. Predicted versus actual median model points. 72
Figure 43. Main effect plot of particle distribution median versus flow velocity. 73
Figure 44. Main effect plot of particle distribution median versus laser beam location. 73
Figure 45. Predicted versus actual Dv90 model points. 73
Figure 46. Main effect plot of Dv90 versus flow velocity. 74
Figure 47. Main effect plot of Dv90 versus laser beam location. 74
Figure 48. Predicted versus actual D32 model points. 75
Figure 49. Interaction plot of D32 for combinations of flow velocity and laser beam location. 76
Figure 50. Predicted versus actual D43 model points. 76
Figure 51. Main effect plot of D43 versus laser beam location. 76
Figure 52. Main effect plot of D43 versus laser beam location. 76
Figure 53. Particle size distribution for DoE3 conditions at centerline and 1.50 g/s for various flow velocities. Cumulative distribution curves follow the left axis, and converge to 100%, while non-cumulative plots follow the right axis. 79
Figure 54. Particle size distribution for DoE2 conditions at 200 m/s and 1.50g/s particle feed rate for various laser beam locations. 80

Figure 55. Particle size distribution for DoE2 conditions at 200 m/s and centerline with varying feed rates. 80
Figure 56. Predicted versus actual transmission model points. 82
Figure 57. Main effect plot of transmission versus flow velocity. 83
Figure 58 Main effect plot of transmission versus particle feed rate. 83
Figure 59. Predicted versus actual Dv10 model points. 84
Figure 60. Main effect plot of Dv10 versus flow velocity. 85
Figure 61. Main effect plot of Dv10 versus laser beam location. 85
Figure 62. Particle size distribution for DoE3 conditions at centerline and 1.5 g/s for various flow velocities. AMTD corresponds to the distribution for sand particles, as received from PTI, when fed through the Sympatec RODOS dispersion unit. 88
Figure 63. Particle size distribution for DoE3 conditions at 200 m/s and at the centerline for various feed rates. 88
Figure 64. Particle size distribution for DoE3 conditions at 200 m/s and 1.5 g/s for various laser beam locations. 89
Figure 65. Particle size distribution for DoE3 conditions at 100 m/s and 1.5 g/s for various laser beam locations. 89
Figure 66. Particle size distribution comparison between three laser diffraction systems: Microtrac with Mie theory, Malvern with Mie theory, and Sympatec using Fraunhofer theory. 91
Figure 67. Predicted versus actual transmission model points. 94
Figure 68. Interaction plot of transmission for combinations of flow velocity and laser beam location. 94
Figure 69. Main effect plot of transmission versus particle feed rate. 94
Figure 70. Predicted versus actual Dv10 model points. 96
Figure 71. Predicted versus actual Dv50 model points. 96
Figure 72. Main effect plot of Dv10 versus laser beam location. 96
Figure 73. Main effect plot of Dv10 versus laser beam location. 96
Figure 74. Interaction plot of Dv50 for combinations of flow velocity and laser beam location. 97
Figure 75. Main effect plot of Dv50 versus laser beam location. 97
Figure 76. Predicted versus actual Dv90 model points. 98
Figure 77. Main effect plot of Dv90 versus flow velocity. 98
Figure 78. Predicted versus actual D32 model points. 99
Figure 79. Predicted versus actual D43 model points. 99
Figure 80. Main effect plot of D32 versus flow velocity. 99
Figure 81. Main effect plot of D32 versus laser beam location. 99

Figure 82. Main effect plot of D43 versus flow velocity...100
Figure 83. Main effect plot of D43 versus laser beam location..................................100
Figure 84. Particle size distribution for horizontal particle injection at the centerline for 1.50 g/s for various flow velocities. 102
Figure 85. Particle size distribution for horizontal particle injection at 200 m/s for 1.50 g/s for various laser beam location. 102
Figure 86. Particle size distribution for horizontal particle injection at 200 m/s and the centerline at various particle feed rates. 103
Figure 87. Particle size distribution for reduced rig conditions at 220 m/s for 1.33 g/s for various laser beam locations. 105
Figure 88. Particle size distribution for reduced rig conditions at the centerline for 1 g/s for various flow velocities. 105
Figure 89. Contour plots of rig exit plume at various testing conditions.................107
Figure 90. Drag coefficients for various particle sizes, sphericities, and flow velocities. 108
Figure 91. Ratio of horizontal versus vertical force components for various particle sizes, sphercities, and flow velocities...109

LIST OF TABLES

Table 1. Sand composition for AMTD and AFRL 03. 15
Table 2. Published Particle Size Distribution of AMTD. 30
Table 3. Summary of laser diffraction systems used. 33
Table 4. Summary of testing conditions for two levels for DoE1....................39
Table 5. Summary of testing conditions for three levels for DoE2. 41
Table 6. Summary of testing conditions for three levels for DoE3. 43
Table 7. Summary of testing conditions for particle sizing through reduced rig diameter, at 1 g/s. 44
Table 8. Laser beam edge location during measurement....................54
Table 9. Response model equation coefficients for DoE1. 55
Table 10. Response model equation coefficients for DoE2. 67
Table 11. Response model equation coefficients for DoE3. 82
Table 12. Response model equation coefficients for horizontal particle injection cases. 92

ACRONYMS

AFRL - Air Force Research Laboratory

AMTD - Arizona Medium Test Dust

ANOVA - Analysis of variance

Cd - Drag coefficient

CMAS - Calcium-magnesium aluminosilicate

D32 - Sauter mean diameter

D43 - DeBroukere mean

DoE - Design of Experiments

Dv10 - Diameter of 10th percentile of distribution

Dv50 - Diameter of median of distribution

Dv90 - Diameter of 90th percentile of distribution

EPCS - Ensemble particle concentration and size

LFE - Laminar flow element

PDI - Phase-Doppler interferometry

PIV - Particle image velocimetry

PSD - Particle size distribution

PTI - Powder Technology Inc.

Re - Fluid Reynolds number

Rep - Particle Reynolds number

RI - Refractive index

SDC - Sample delivery controller (from Microtrac)

St - Stokes number

ACKNOWLEDGEMENTS

First, a very big thank you to my committee members, Prof. Jabbari, Prof. McDonell, and Prof. Samuelsen. Thank you for your patience and time in reviewing this work. Thank you for being a part of this journey.

Thank you, Prof. Samuelsen, for providing me the opportunity to conduct research as a graduate student at APEP. Being part of a lab with such a unique structure has meant working with students, faculty, and staff, with diverse backgrounds and interests, leaving me with great memories and experiences that I shall treasure.

Thank you, Prof. McDonell, for your guidance for the past three years of research. I am thankful for the undergraduate research opportunity since it opened the doors for graduate school and some interesting projects, including this work. I have enjoyed every project that I have been a part of.

Thank you, Max Venaas, for your help in the lab. I appreciate your patience and your willingness to help, all the time. You will have one less person to be bugged by now! Thank you, Andy Smith, for always enthusiastically answering my questions on laser diffraction, and being a part of my Sympatec related experimental investigations. Thank you, Hal Technology, for this collaboration, and the Navy for project funding. To APEPers, thank you for the laughs, discussions on class questions, research questions, and life questions. Thanks for the friendships and some good memories.

Finally, thank you again, Prof. Samuelsen and Prof. McDonell for supporting my future research endeavors. I shall bring all I have learnt at APEP onto my next journey.

ABSTRACT OF THE THESIS

An Experimental Investigation of High-Velocity Non-Spherical
Polydisperse Particle-Laden Flows

By
Alice Kate Li

Master of Science in Mechanical and Aerospace Engineering
University of California, Irvine, 2020

Professor G. Scott Samuelsen, Chair

The intake of fine particles such as volcanic ash and sand into gas turbine engines is detrimental in several ways, such as prompting premature wear of turbine blades from surface erosion and corrosion; causing deposits to melt on blades and vanes; and creating material build up in engines. To aid the development of commercial real-time sensors designed to monitor particle ingestion (e.g., particle size, particle concentration, and species composition), a high-velocity particle-laden environment is developed to simulate engine inlet conditions using polydisperse non-spherical reference particles. The environment is then used to perform an experimental investigation to characterize particle sizes across the rig profile for various flow velocities and particle loads, using two laser-diffraction systems. Design of Experiments is used to develop a test plan and statistically resolve the data. The rig produces repeatable flows simulating particle-laden engine inlet conditions with fluid velocities between 100 m/s – 200 m/s and Reynolds numbers of 1.74 x 10^5 – 3.48 x 10^5, for polydisperse reference particles of 0.25 µm – 178 µm and particle Reynolds numbers of 4.4 – 2700, injected into flows at 0.5 g/s – 1.67 g/s, equivalent to loadings of Φ = 3.5 x 10^{-3} – Φ = 27 x 10^{-3}. In the rig developed, probes can be evaluated for the entire particle size range of the reference particles, at engine inlet conditions. Design of Experiments models can be used to appropriately position probes to validate sizing performance. The test rig is, therefore, deemed suitable for guiding the development of commercial particle ingestion monitoring sensors.

1

INTRODUCTION

1.1 Overview

Material ingestion into gas turbines is a problematic yet unavoidable phenomena for aircraft flying over arid land or regions of volcanic activity, and even stationary power generation systems. The intake of particles such as volcanic ash and sand is detrimental in several ways: it prompts premature wear of turbine blades due to surface erosion and corrosion; causes deposits to melt on blades and vanes; and creates material build up in the engine. Some situations have been so unmanageable at the time of ingestion that aircraft engines have failed in operation and have even caused fatalities. These incidents could potentially be avoided if real-time particle monitoring sensors were installed in gas turbine engines. With such sensors, pilots would be notified of the amount and type of particles being ingested into the engine in real-time, and thus be able to make informed decisions of flight paths. A secondary benefit for such a sensor would be predictive maintenance and thus reduced maintenance and repair costs. A sensor suitable for this application must be able to measure particle size distributions (PSD) of non-spherical particles, represented by a volume distribution; the concentration of ingested materials; and the constituents of materials ingested into the engine, at elevated velocities, temperatures, and pressures. To aid the development of such a sensor, a particle-laden environment simulating engine conditions is developed. This environment is characterized to assess particle size distributions in developing particle-laden turbulent flow, for various flow velocities and particle loads, across the rig profile. Based on a review of the literature, discussed in Section 2, open questions regarding this subject include experimental facility developments and studies of high-velocity polydisperse non-spherical particles in turbulent wall-bounded flows.

1.2 Goal

The goal of this research is to develop and evaluate a test rig to produce repeatable high-speed particle-laden flows with non-spherical reference particles for the purpose of guiding the development of commercial, real-time sensors for monitoring material ingestion into gas turbine engines.

1.3 Objectives

To meet this goal, the following objectives must be achieved:

1. Design and assemble experimental setup to generate flow of particles in air.
2. Characterize single-phase flow conditions.
3. Determine nominal particle size distribution data for test dust used.
4. Conduct study to screen factors that alter PSD.
5. Conduct experiments for determining effects on PSD.
6. Analyze and model the non-homogeneous dispersion of high-velocity polydisperse particles in wall-bounded turbulent flow conditions.

2

BACKGROUND

2.1 Turbomachinery Studies

Numerous studies over the past several decades have indicated the negative impacts of particle ingestion into gas turbine engines. The first negative impact is erosion. To understand the severity of erosion, an experimental and computational study by Hamed et al. shows that for erosion caused by particle impingement, surface roughness increases with impact angle and size [1]. Another study, by Tabakoff et al., involving simulations alone demonstrate that the PSD has a large influence on the blade erosion intensity and pattern [2]. Vogel et al. contributes to the understanding of particles entering the vulnerable engine core section which is critical for safety [3]. Brun et al. perform computational fluid dynamics on particles ingested into gas turbine engines, revealing the impacts of particles on rotating machinery [4]. Corrosion also occurs from particle ingestion as shown in work by Mechnich et al. [5]. Material deposition is additionally of concern. This has been addressed in computational work by Cheng et al. [6] and experimental work by Bojdo and Filippone [7], as well as Boulanger et al [8]. Hamed et al. reviews more erosion and deposition studies [9]. Finally, particle ingestion also causes clogging of cooling holes as demonstrated by Cardwell et al. [10] as well as

Walsh et al. [11]. Flow blockage on a nozzle guide vane leading edge is also studied by Whitaker et al. [12].

Figure 1. First stage turbine blade degradation from particulate ingestion [13].

Figure 2. Leading edge erosion of a NASA DC-8-72 after volcanic eruption encounter [14].

2.2 Potentials of Real-Time Sensor Implementation

Further, studies show that real-time particle size information could aid in-flight decisions. Since not all particles sizes are equally hazardous, particle size information could infer the type of damage potentially imposed on gas turbine engines in real-time.

In an experimental study by Dean et al. [15], particles of 5 – 50um were studied, as previous studies [16] and [17], indicated that particles of this size range were of most concern because they make frequent impact with solid surfaces and are also small enough to melt and deposit onto turbine components. Particle size distributions could also be used to determine the concentration of particles ingested into the engine as detailed by Vogel et al. [3] and Scala et al. [18], which if provided to pilots in real-time, could have prevented the incidents previously mentioned.

2.3 Previous Sensor Development

Given the need for such a sensor, there has been some work on the development of technology for this application. However, there exists a lack of emphasis on the ability to characterize particles travelling at gas turbine engine inlet velocities. Recent work includes that by Papadopoulos et al. [19] where plasma emission spectrometry methods were used to determine particle size and species. Work by Weickert et al. demonstrates the use of electrostatic methods to detect dust and debris [20]. In [19], the sensor was only tested at moderate velocities of 70 m/s, while velocity limitations were not mentioned in [20]. There have been some studies assessing the relationship between PSD and flow speeds, but only at low velocities. A particle sizing system using imaging and electrostatic sensors, as detailed by Carter et al., acquired PSDs from 5 m/s to 20 m/s at increments of 5 m/s, and showed insensitivity to flow velocity [21]. Despite these promising results, it is paramount to confirm sensor functionality at elevated velocities because particles entering turbine inlets travel at velocities of around 200 m/s – 250 m/s (447 – 560 mph), as predicted in a numerical model by Shinozaki [16]. This thesis involves the development of such an environment.

2.4 Previous High-Velocity Dust-Laden Facilities

Works involving the development of particle laden environments simulating engine ingestion, include those by Boulanger et al. [8] as well as Delimont et al. [22], where an aerothermal rig was used for sand deposition testing on test coupons, up to 1100°C. However, flow velocities are limited to around 70 m/s. In addition, accelerated deposition facilities, such as those in work by Jensen et al., have proven successful in conducting 4-h tests on deposition to simulate 10,000 hours of operation [23]. These studies were conducted at Mach numbers of 0.34, equivalent to around 115 m/s, and temperatures of 1150 °C with focus on material deposition due to particle ingestion. In the current work, flows velocities required to simulate engine inlet conditions travel up to 200 m/s, which corresponds to a Mach number of 0.58.

2.5 Particle-Laden Flow Studies

There have been a vast number of experimental and numerical studies focusing on characterizing turbulent particle-laden flows, given its connection to numerous applications including aerosols, coal combustions, and exhaust plumes. One of the early works is that by Modarress et al., whereby turbulence intensities and gas-phase turbulent shear stresses of two-phase turbulent jets were studied using laser Doppler anemometry

[24]. Findings show that the presence of particles reduces the turbulence intensities. Sommerfield discusses how wall roughness and inter-particle collisions dramatically influence the particle behavior in horizontal channel flow [25]. This was performed for several groups of monodispersed spherical particles. In more recent work by Fong et al., velocity and spatial distributions of particles in turbulent channel flow were investigated for spherical glass microspheres [26]. For non-spherical particles, Wachem et al, gives insight on the effects of non-sphericity on collisions between other particles and walls [27]. However, the study solely involves modelling. Borée et al. study the effects of mass loading and inter-particle collisions of polydisperse particles. The particles are, however, spherical. Thus, in the current literature, is little experimental work on studying particle-laden flows of non-spherical polydisperse particles in turbulent pipe flow.

2.6 Methods for Characterizing Particles in Particle-Laden Flows

To study turbulence and particle behaviors, a commonly used technique in this space is particle image velocimetry (PIV). A review by Westerweel et al. summarizes the achievements of PIV in the study of turbulent flows [28]. Tu et al. discuss other experimental techniques for measuring micro-to-nano-particle-laden gas flows, including phase-Doppler Interferometry (PDI) and light scattering intensity measurements [29]. Given the choice of two commonly used laser diagnostics for particle sizing, PDI was not used in this study, because of its inability to size non-spherical particles. Also, acquiring line of sight ensemble measurements was desirable because such data represent the distribution of particles within a measurement volume, rather than at certain points, such as those in Phase Doppler measurements, which would not be time effective.

2.7 Methods for Particle Sizing

If focusing on sizing of particles, where velocity information is not of interest, several dominant techniques exist. One of the oldest methods is sieve analysis. More modern techniques include dynamic image analysis and laser diffraction. Ulusoy demonstrates how dynamic image analysis is superior to sieving in accuracy and speed, as the former method accounts for particle sphericity [30]. A study by Stefano et al. compare grain-sizes of sand and clay using both a laser diffraction system and a sieve combined with hydrometer method, called a sieve-hydrometer system [31]. The aim was to create a correlation between sieve-hydrometer, an accepted and certified sizing method, and laser diffraction, a more time efficient sizing method. Results showed that for sand particles, the distributions acquired by both methods were similar, confirming that the accuracy and convenience of laser diffraction systems makes measuring sand particles with the system favorable. A laser diffraction system will be used in this work.

2.8 The Challenge of Sizing Non-Spherical Particles

However, despite the convenience of laser diffraction, the non-spherical nature of particles that get ingested into engines may pose as a challenge. Studies have doubted the validity of sizing non-spherical particles using laser diffraction [32], [33]. A study by

Blott and Pye involves sizing of natural materials such as soil, silt, and sand with sieving and laser diffraction [34]. Discrepancies in distributions acquired increased with particles of reduced sphericity. Farafonov et al. describes a spheroidal model in an attempt to solve this problem of non-sphericity [35]. If non-sphericity is solved, and if repeatable and similar PSD are obtained for both the probe sensor and laser diffraction system, an important question to then answer is: what does a PSD represent for non-spherical particles? More specifically, can a volume distribution be accurate enough to estimate the volume of particles being ingested into the engine?

2.9 Summary

It is evident that there is a lack of work on sizing particles at high velocities, and of a non-spherical nature, in wall-bounded turbulent flow. Therefore, this work will focus on the assessment of particle sizes and concentration in a high-velocity particle-laden flow rig ingested with polydisperse test dust contaminants, simulating engine inlet conditions. Laser diffraction diagnostics will be used for their rapid measurement times. Effects of particle sphericity will be investigated based on comparisons to a system that accounts for particle sphericity. This fully characterized particle flow will be used, in the future, to evaluate the particle sizing capabilities of a compact fiber-optic probe sensor for gas turbine particle ingestion monitoring.

3

APPROACH

The goal of this research is to develop and evaluate the ability of a test rig to produce repeatable high-speed particle-laden flows with non-spherical reference particles, to guide the development of real-time commercial sensors for monitoring material ingestion into gas turbine engines [36], [37]. The following tasks were accomplished to achieve this goal.

Task 1. Design and assemble experimental setup to generate flow of particles in air and characterize sand particles:

The experimental setup was designed to achieve three major goals: generate high velocity flow, ingest particles into flow, and integrate laser diagnostics for particle characterization. The high velocity flow rig was engineered to produce air flow of up to 200 m/s. An eductor was sourced for particle ingestion into the rig, providing an environment simulating harsh engine conditions – conditions under which the probe must be able to characterize particles. A particle feeder was identified for feeding particles at a rate that would generate sand in air mixtures similar to that in a gas turbine engine. A test section was developed for flush mounted insertion of a commercial probe. And a laser diffraction diagnostic capable of characterizing particles was also incorporated to the setup, to allow for simultaneous measurements with commercial probe sensors for direct comparisons between both data sets. The rig was fit onto a translational plate, allowing for laser diffraction measurements at various locations with respect to the rig exit face. Diagnostics were setup to measure PSD for sand flowing through various rig lengths, rig flow velocities, particle in air concentrations, as well as laser beam locations.

Task 2. Characterize single-phase flow conditions:

Flow conditions for a range of velocities were characterized. Air flow velocities were confirmed for a range of supply pressures, using a pitot tube for point velocities and laminar flow element (LFE) for bulk flow velocities. Flow velocities were confirmed for velocities from 65 m/s to 200 m/s.

Task 3. Determine nominal particle size distribution data for test dust used:

The PSD deemed baseline for this experiment was then determined. Since the primary goal of this thesis is to characterize particles under various rig conditions, two advanced laser diffraction technologies with built-in particle dispersers were used to generate the nominal particle size distribution. Using such dispersers was deemed necessary since they are designed very carefully to prevent any agglomeration as well as break-down of material, which are potential phenomena within the current rig designed.

Task 4. Conduct study to screen factors that alter PSD:

A Design of Experiments (DoE) was performed to assess and determine the experimental setup factors that affect the particle size data obtained from the laser diffraction system. Factors that were studied were rig length, rig flow velocity, particle feed rate, particle suction pressure, and sensing region location. Results from this DoE were used to give insights and screen the factors that were worth investigating in more depth in the following task.

Task 5. Conduct experiments for determining effects on PSD:

An in-depth experimental study was conducted to determine the degree to which screened factors altered the PSDs. Particle size distributions were measured at various locations of the rig exit profile, sand feed rates, and sand velocities, using the laser diffraction system. Additional tests with a second laser diffraction system were performed to demonstrate repeatability and reproducibility of sand flow within the rig, crucial for evaluating commercial probes under development. These measurements also covered lower particle load measurements.

Task 6. Analyze and model the non-homogeneous dispersion of high-velocity polydisperse particles in wall-bounded turbulent flow conditions.

Based on the results, several additional tests were conducted to better understand the causes for the relationships between experimental conditions and PSD. To further understand the non-homogeneity of particle dispersion, particles were injected horizontally into the rig side wall instead of vertically from the top. In addition, sizes of particles conveyed through a reduced pipe diameter were characterized. Particle size measurements were recorded for these rig configurations at various velocities and laser beam locations.

The data produced from this thesis should provide particle size distributions for particles flowing within the rig at various experimental conditions and measurement locations. Models with confidence intervals of 95%, and statistical significance, according to analysis of variance (ANOVA) parameters, will be developed for particle size parameters and concentration. These models would be used to determine particle size and concentration as a function of flow velocity, particle feed, and measurement location, for commercial probes evaluated in the rig. Probes will be evaluated for the ability to size particles at engine inlet conditions, as well as assess sizing performance over time, when testing for probe durability after exposure to harsh conditions.

4

METHODOLOGY

4.1 Test Dust Contaminant

A standard test dust was selected for ingestion into the high-velocity particle-laden rig for measurement by the laser diagnostics. The test dust used was Arizona Test Dust Medium, ISO 12103-1, A3 Medium Test Dust (AMTD).

Since engines are required to undergo sand ingestion tests, several sands have been synthesized for engine and component testing. The U.S. Air Force Research Laboratory (AFRL) synthesized sand simulating sand ingested into engines. The sand is now commercially available from Powder Technology Inc (PTI), a test dust manufacturing company. Synthesized sands include AFRL 02 for component-level testing or AFRL 03 for engine-level testing, coarser than AFRL 02. However, above 1200°C, these sands produce calcium-magnesium aluminosilicate (CMAS), a molten form of sand, which deposit and even infiltrate component coatings. Although high-temperature probe sizing evaluations are not included in this work, they shall be conducted in future work in the same high-velocity particle-laden rig. And since evaluating the sizing functionality of the probe was the main near-term sensor development goal, AFRL was not chosen, as CMAS would hinder evaluating the probe's sizing capabilities. Instead, AMTD test dust, manufactured by PTI, without CMAS yet with a similar PSD to AFRL, as shown in Figure 3, was chosen. Table 1 compares the chemical composition of AFRL and AMTD.

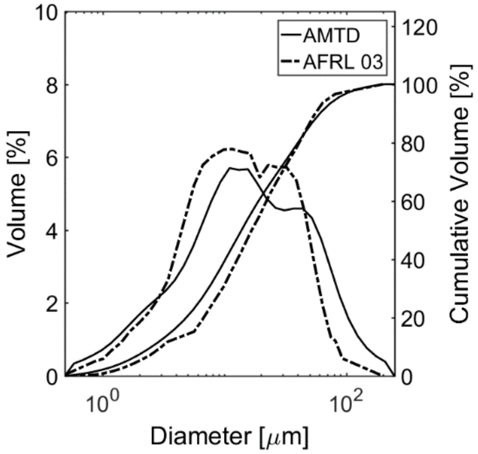

Figure 3. Cumulative particle size distribution of AMTD and AFRL 03.

	Species	Weight %
AMTD		
	Silica	69 – 77
	Aluminum Oxide	8 – 14
	Calcium Oxide	2.5 – 5.5
	Potassium Oxide	2 – 5
	Sodium Oxide	1 – 4
	Iron (III) Oxide	4 – 7
	Magnesium Oxide	1 – 2
	Titanium Oxide	0 – 1
AFRL 03		
	Quartz	34
	Gypsum	30
	Aplite	17
	Dolomite	14
	Salt	5

Table 1. Sand composition for AMTD and AFRL 03.

Figure 4 shows a microscopic image of AMTD at 60x magnification. The image illustrates the particles' non-spherical nature, where most particles are irregularly shaped, some with jagged edges, contrasting the sphericity and uniformity of monodisperse glass beads in Figure 5.

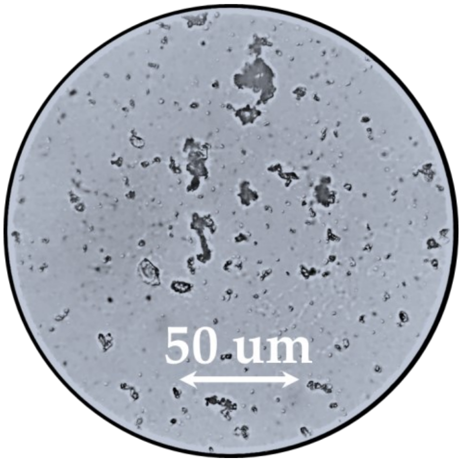

Figure 4. Microscopic image of polydisperse AMTD.

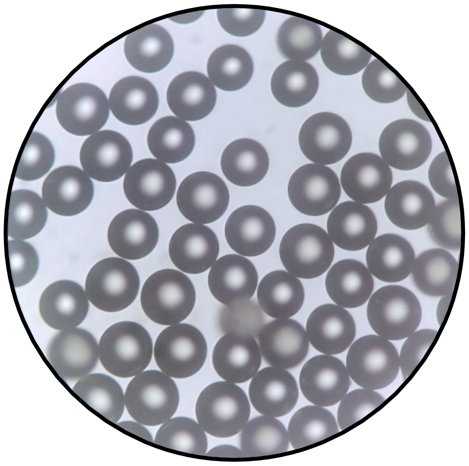

Figure 5. Microscopic image of 75 μm glass beads.

4.2 Equations Governing Particle-Laden Flows

To ensure that particles were conveyed and not settling to the bottom of the rig, some equations for dilute-phase particle-laden flows were sought to confirm that conditions enabled particles to convey successfully. Equations governing forces acting on solid particles in gaseous flow were also studied.

4.2.1 Pneumatic Dilute-Phase Solids Conveying

Producing high-velocity particle-laden flows was fundamental for this work. To perform effective evaluations for commercial probes, these flows should ideally be well dispersed, so that the probe can be exposed to particles of all sizes for measurement. From a pneumatic conveying perspective, for dilute-phase particle-laden flows, where dilute-phase corresponds to Φ, solid to gas mass flow rate ratios, of typically less than $\Phi = 15$ [38], gas flows must be greater than saltation velocity to achieve homogeneity. Saltation velocity is defined as the minimum gas velocity for solids to be suspended in a horizontal pipeline. When the gas velocity in dilute particle-laden flows fall below saltation velocity, gravitational forces and frictional forces dominate the drag and lift forces. This causes particles to salt out or settle and deposit at the bottom section of the channel.

Assuming that sand in air loads are less than $\Phi = 15$, saltation velocity can be computed for a range of particles and loads up to $\Phi = 15$ by the Rizk equation where Φ is the mass flow rate ratio of solid to gas, d [mm] is the particle diameter, g [m/s^2] is gravitational acceleration, D [m] is the pipe diameter [38].

$$\Phi = \frac{1}{10^{\delta}}\left(\frac{v_s}{\sqrt{gD}}\right)^{X} \tag{1}$$

$$\delta = 1.44d + 1.96 \tag{2}$$

$$X = 1.10d + 2.50 \tag{3}$$

The Rizk equation was used to plot saltation velocity, v_s, for various particle sizes, d. This was plotted for inner pipe wall diameter, D = 26.7 mm. Maximum loadings across all experiments in this study was $\Phi = 0.02$. In taking into account potential spikes in feeding from the particle feeding methods, using a screw feeder, the maximum particle feeding is assumed to be Φ = 0.2. However the curve for Φ = 15, was also plotted to show that for all dilute flow cases, the gas flow velocity in this high-velocity particle-laden rig is sufficient to convey particles, without allowing them to fall from gravity. This plot is shown in Figure 6. The plot reveals that all particles sizes in the particle size distribution of AMTD, up to 178 µm, do not settle, so long as gas flow velocities are greater than 90 m/s, which is less than the minimum flow condition used in surface response models.

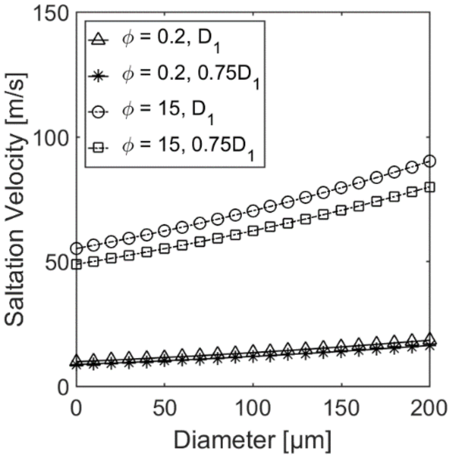

Figure 6. Saltation velocities for various particle diameters, mass loadings of Φ = 2 and Φ = 15, and pipe diameters of D = 1 inch, and D 0.75 inch.

4.3 Experimental Setup

The high-velocity particle-laden flow was developed in two phases. The first involved ensuring that gaseous flows produced met the velocities of interest. In the second phase, particles were introduced to the high-velocity flow rig. The entire rig setup is shown in Figure 7.

4.3.1 Generating High-Velocity Flow

In assuming particles do not salt out of the main particle-laden plume at 100 m/s, and the flow velocity of interest is 200 m/s, from communications with gas turbine engine companies, a flow rig supplying 100 m/s to 200 m/s was developed. A volumetric flow rate of around 215 cfm was required to achieve 100 m/s to 200 m/s gaseous flow through a round pipe of inner diameter $D = D_1 = 26.7$ mm. This flow rate was achieved through supplying dry compressed air through a 9.525 mm sonic orifice plate upstream of the D_1 pipe section. Horizontal, as opposed to vertical, pipe flow was chosen, since this represents particle-laden flow in a mostly horizontal engine. A pipe size smaller than D_1 may allow all conveyed particles to be measured in a single measurement zone; however, being exposed to a narrow plume of particles is not characteristic of a real engine environment. It would also fail to provide insight to dispersion or segregation within the flow, which would be valuable to highlight since in a real engine environment, the commercial probe would be flush mounted with sensing region approximately 10 mm away from the probe face; also, further segregation would be likely to occur with larger engine cross sections and complex geometries. In addition, given that the particle feeder is limited to feeding particles at a minimum of 0.03 g/s, at 100 m/s to 200 m/s, particle loads may be too high to successfully deagglomerate particles, making environments unsuitable for probe sizing capability evaluations.

High-velocity bulk flow and point flow were verified using laminar flow element (LFE) and pitot tube point measurements, respectively. Pitot tube measurements were acquired for several locations along the horizontal and vertical lines intersecting the centerline. This was done to assess symmetry in the flow profiles. Profiles are shown and discussed in Section 5.1.

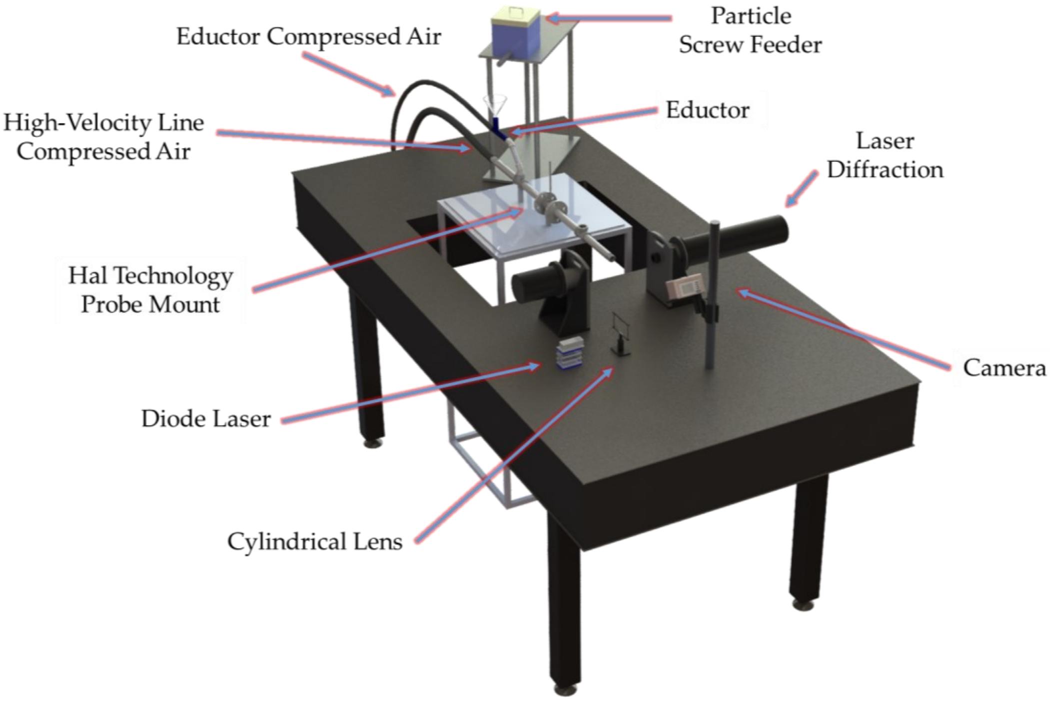

Figure 7. High-velocity particle-ingestion experimental rig.

4.3.2 Particle Ingestion

With the desired gas flow rates achieved, from successful validations, components necessary for particle ingestion were then incorporated. As shown in Figure 7, following around 10 inches of 1-inch diameter pipe, sand particles were ingested via a 12.7 mm Fox Valve eductor, as shown in Figure 8. The eductor internal geometry comprises of a constriction, creating a region of low pressure when compressed air is fed into the motive inlet, drawing material into the eductor through the suction port. Upon ingestion, particles mix with the compressed air entering the eductor, and particle-laden flow gets discharged through the eductor outlet. The jet of particles from the eductor discharge outlet are further accelerated upon mixing with the cross flowing air from the high-velocity line shown in Figure 7. Around 11.8 scfm is expelled through the outlet, when the eductor is supplied with 80 psig compressed motive air. Given pipe losses, a gauge was installed close to the eductor to ensure 80 psig was being supplied. This is the supply pressure used in this study. Otherwise, the lower end supply pressure recommended by Fox Valve is 60 psig where 9.3 scfm is discharged.

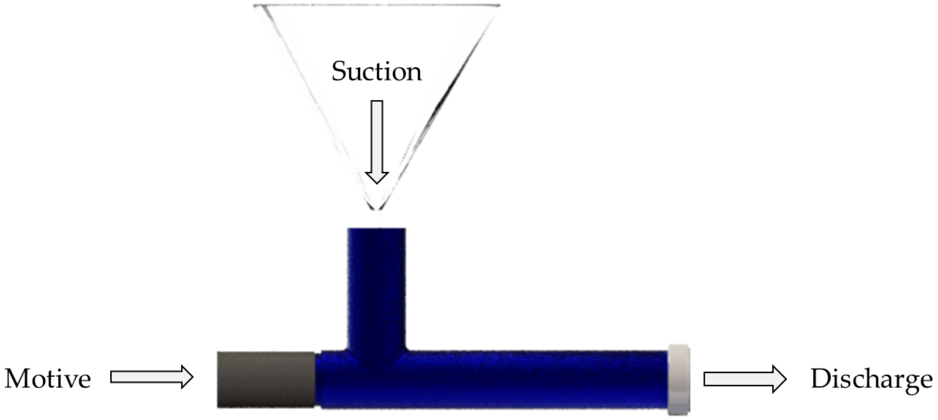

Figure 8. Eductor flow.

It should be noted that these eductors typically operate with the suction inlet attached to an enclosed chamber of material to be ingested, e.g. a hopper full of sand with a heap of particles sitting at the suction port, and being fed continuously into the stream.

However, this would have produced much higher particle feed rates – rates around 100 times those expected to exist in gas turbine engines [12], [39]. Discussion with the vendor indicated that using a particle feeder with required feed rates, instead of a hopper, would be the best solution. The setup adopted meant that air was introduced into the rig through the suction port, as well as the motive port. Flow rates through the suction port were measured to be around 15.7 scfm, when using the eductor alone at 80 psig, the operating pressure condition used for this study.

4.3.3 Sensitivity of Particle Size Distribution to Particle Feeding

For the current setup, an AccuRate particle feeder was used. It is a mechanical feeder with a leadscrew. This design causes particle feed rates to vary with time. To assess the dynamics of the feeding, the laser diffraction system was used to gauge how transmittance varied with time. Transmittance is a measure of the amount of laser beam light that is neither blocked nor scattered by the particles. With higher particle in air concentration comes lower transmittance, and vice versa. It should be noted that even with fluctuations in transmittance, particle size distribution data standard deviations generally remained within 5% of the average size of particle size parameters, which was deemed suitable for the study.

Feed rates used are detailed in Section 4.5. These were averaged rates determined over measurements over a duration of 60 seconds, with errors of ± 0.1 g/s. The particle in air concentrations corresponding to combinations of feed rates and velocities are also discussed in Section 4.5. It should be noted that the hopper was filled with at least 2-liters of sand at a time, to ensure that a lack of particles in the hopper did not contribute to lowered feed rates.

4.4 Laser Diagnostics Setup

Two laser diffraction systems were used in this experiment. Laser diffraction has been used in numerous industries for particle characterization, including combustion, pharmaceutical, and agriculture, because of its ease of use and ability to calculate and output distributions at fast rates [40]. This was the primary reason for its use in this work. The models used were selected due to availability. The following sections describe the systems in further detail.

It should be noted that at these high velocities, PIV measurements would have been beneficial to validate certain hypotheses. However, a high-speed camera suitable for PIV for such high-velocities and small particles was not available for the current study.

The size distributions of particle-laden plumes generated at the exit of the flow rig were separately analyzed with these laser diffraction systems. The centers of the laser diffraction beams were positioned 12.7 mm away from the high-velocity pipe exit. It is assumed that the particle jet should behave as is, at this axial distance from exit. Figure 10 illustrates the general process of laser diffraction systems, where the lens and detector are components of the laser diffraction receiver. A laser beam from a transmitter is illuminated in the direction of a particle plume. Laser beam light incident on an individual particle either gets refracted, absorbed, or diffracted as shown in Figure 9. Laser diffraction systems measure the degree of diffraction of this incident light, of which the diffraction angle is dependent on the particle size. The greater the particle size, the stronger the scattering intensity; also, the smaller the scatter angle, as illustrated in Figure 11. Thus, for an ensemble of spherical particles, a diffraction pattern is generated. This is captured on a circular detector of many rings on the laser diffraction receiver, and the pattern is used to determine the distribution of particles within a sample. Larger particles will scatter the light onto more central rings, while smaller particles scatter light onto outer rings. At higher particle loads, multiple scattering algorithms are applied by the software. The sum of diffraction patterns generated by an ensemble of particles is converted into a PSD. Since particles are non-spherical, the sizes are based on the relative volume of equivalent spherical particles of the same size. The deconvolution from a scattering pattern to a distribution is performed using a model, unique to the laser diffraction system, based on light scattering theories that will be discussed in the next section. PSDs are measurements averaging around 20 seconds of data acquired at 1000 Hz.

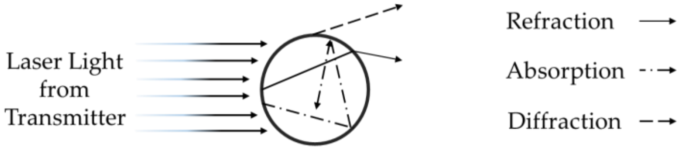

Figure 9. Path of light upon encountering a particle. Line type selected does not signify any light phenomena.

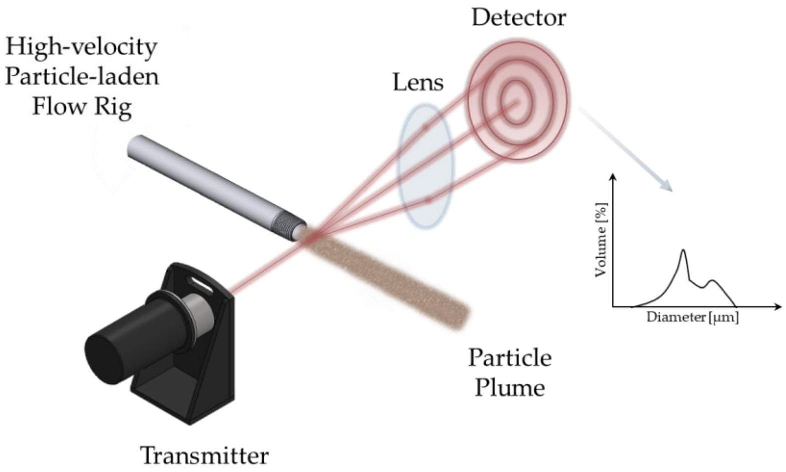

Figure 10. Laser diffraction illustration.

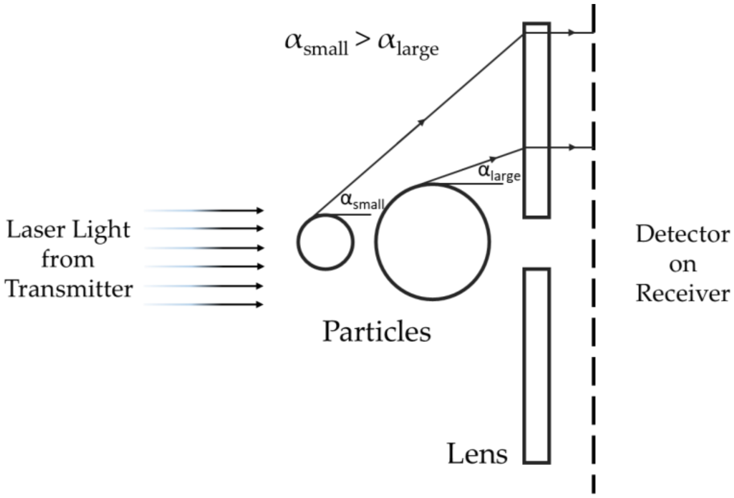

Figure 11. Scattering angle for large and small particles. Adapted from Malvern Insitec RTSizer manual.

4.4.1 Malvern Insitec ST97 Laser Diffraction System

The first laser diffraction system used for sizing the particles in the high-velocity particle-laden plumes was the Malvern Insitec ST97 Ensemble Particle Concentration and Size (EPCS). RTSizer software was used to acquire PSD data using scattering patterns obtained with the system hardware. Hardware includes a laser transmitter, a receiver, and a laser power supply. The transmitter emits a 670 nm wavelength laser beam of 10 mm in diameter. The receiver has a 200 mm lens installed, allowing the system to size particles between 0.25 μm and 1000 μm.

The PSD produced is dependent on system models. For the Malvern Insitec ST97, models are based on Mie theory. The theory assumes that spherical particles are being measured. Also, it uses the difference in refractive index between the particle and dispersing medium to model the intensity of light that gets diffracted, as opposed to refracted or absorbed, when light is incident on an individual spherical particle.

The system was calibrated before each use using a reticle of known Rosin-Rammler parameters. So long as the Rosin-Rammler distributions produced by the reticle were within 10% of the given parameters, the system was deemed well aligned.

4.4.1.1 Refractive Index Sensitivity

Given that studies including that by Rawle [41] indicate the importance of opting for correct refractive index (RI) when using laser diffraction systems using Mie Theory, a brief sensitivity study was performed to seek any variations in PSDs of the test dust for different real and imaginary parts, which are a measure of particle refraction and absorption, respectively. For this, three different calibration files were generated with varying real part RI = 1.54 + 0.00i, RI = 1.33 + 0.00i, and RI = 2.50 + 0.00i, giving distributions in Figure 12. Figure 13 shows comparisons of distributions for the test dust with RI = 1.54 + 0.00i, RI = 1.54 + 0.01i, RI = 1.54 + 0.10i, and RI = 1.54 + 1.00i. These plots revealed that changing the absolute part of the refractive index did not change the distributions produced by the software's models or algorithms. However, for the same absolute part of RI = 1.54, the greater the imaginary coefficients of 0.10i and 1.00i gave monomodal distributions with a peak that does not algin with that in the PTI data, considered nominal and will be discussed later.

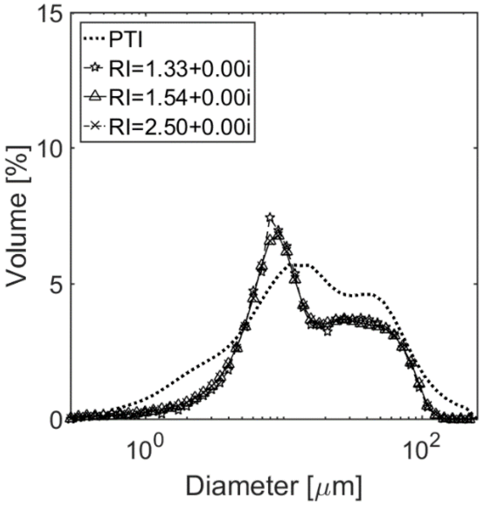

Figure 12. PSD of test dust for varying real refractive index coefficients.

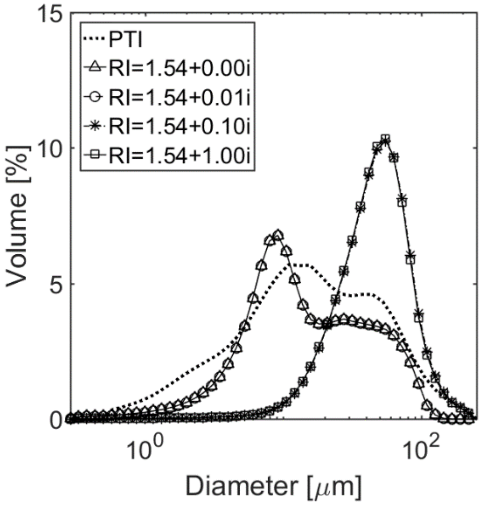

Figure 13. PSD of test dust for varying imaginary refractive index coefficients.

For all laser diffraction measurements for the Malvern Insitec ST97, RI = 1.54 + 0.01i was chosen in the software settings, based on recommendations from work by Rawle [41], and from comparisons to the PTI distribution, which also had two peaks in size distribution.

4.4.2 Sympatec HELOS

A Sympatec HELOS laser diffraction system was also used to measure particles ejected from the high-velocity particle-laden flow rig. This system was used to compare with measurements acquired by the Malvern Insitec ST97 system, as well as contribute to the dataset acquired for particle-laden flow within the rig.

The system can be used with Mie theory when optical properties of the dispersion material are known, and Fraunhofer theory if unknown. The advantage to sizing particles using Fraunhofer theory is that the models are not based on knowledge of refractive indices of the gas and particle medium, as particle refraction and absorption is ignored. This makes Fraunhofer theory very attractive as a sizing system because it is inherently difficult to accurately determine the refractive index of a nonhomogeneous mixture, like that of AMTD, which is made up of eight constituents, as shown in Table 1. Fraunhofer models, however, are known to be less complex than Mie theory models.

Typically, Fraunhofer models fail to predict particle sizes below 50 μm and are particularly inaccurate for particles less than 2 μm. It is the reason why most laser diffraction systems today operate with Mie theory instead. However, the Fraunhofer algorithms in the Sympatec system are more advanced than older models of Fraunhofer systems, and can determine sizes below 1 μm, making it very favorable to size with.

A disadvantage of sizing particles with a system based on Mie theory models is the need for refractive index parameters. This involves rigorous investigations as demonstrated in [41]; also, the refractive index inputted into models is meant to be characteristic of the entire particle plume. In reality, such a value would not be able to accurately define a mixture made up of many constituents, like the eight components of AMTD.

The system has a wide range of lenses that allow for measurements ranging from 0.1 μm – 3,500 μm. An R4 200 mm standard lens was used in this experiment, measuring particles between 1.8 μm – 350 μm. The laser light wavelength used was 632.8 nm, and the beam size is adjustable, but was set to 12.8 mm for this work. The unit can self-align using built-in software, so calibration with a reticle was not performed.

4.4.3 Nominal Particle Size Distribution Data

Table 2 summarizes the general published PSD by the supplier, PTI. The PSD in Figure 14 is more specific to the standard test dust procured, and was acquired by PTI with a Microtrac S3500 laser diffraction system. It represents an average of three measurements. The system measures particle sizes from 0.02 μm – 2800 μm, using Mie theory to determine the PSD of an ensemble of particles on a volume-basis. Typically, laser diffraction systems operate with one laser beam where the laser transmitter and receiver are collinear, and so light diffracted off a particle will be captured at low angles (around 30°), for the lens in use, where the range of measurable particles is limited by this lens. However, the Microtrac S3500 has a tri-laser system and two lenses, capturing backscattering up to 160°, thus enabling a wider spectrum of particle sizes to be measured at a time.

To add, the Microtrac S3500 is claimed to account for non-sphericity of particles. This is achieved by "advanced proprietary algorithms," modified Mie theory models, and ensuring particles undergo turbulent flow and "tumble" during the measurement period. This allows for averaging of the particle size to determine a more representative PSD on a volume-basis.

Size [μm]	AMTD [% Less Than]
0.97	2.0 – 2.4
1.38	3.8 – 4.4
2.75	10.3 – 11.1
5.50	22.1 – 23.2
11.00	42.3 – 43.6
22.00	62.5 – 64.5
44.00	82.0 – 83.5
88.00	94.7 – 96.0
124.50	97.2 – 98.5
178.00	99.0 – 100

Table 2. Published Particle Size Distribution of AMTD.

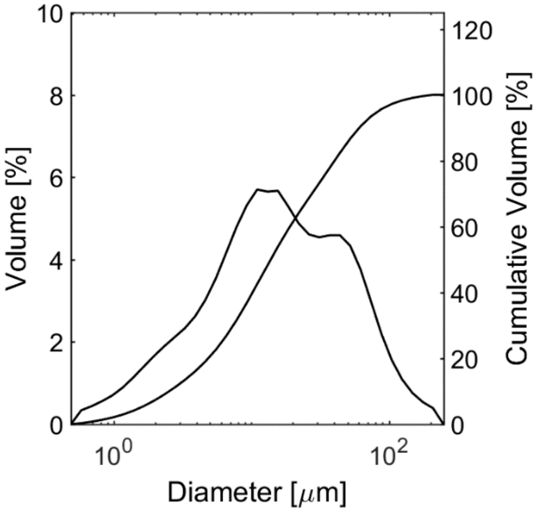

Figure 14. PSD of procured AMTD using Microtrac S3500.

In terms of sample preparation for the Microtrac S3500, the system uses a Microtrac Sample Delivery Controller (SDC). For this, the test medium is suspended in a cell (approximate dimensions: 51 mm x 9.5 mm x 2 mm) filled with a fluid. For AMTD, water was used as the solvent. This suspension is accelerated to the greatest velocity that can be attained before bubble formation within the cell. Based on communication with PTI, it was determined that the suspension and particles within travel at around 1.84 m/s. This speed is negligible compared to that of the particles travelling through the rig.

However, given that the Microtrac sizes particles using Mie theory, its accuracy is dependent on inputted particle refractive index. Therefore, another PSD was acquired from the Sympatec HELOS, using Fraunhofer models. Instead of measuring the plume ejected from the high-velocity particle-laden flow rig, the system was used with a Sympatec RODOS particle dispersing unit. Figure 15 shows a comparison between distribution of sand using the Sympatec system, at the Microtrac described above.

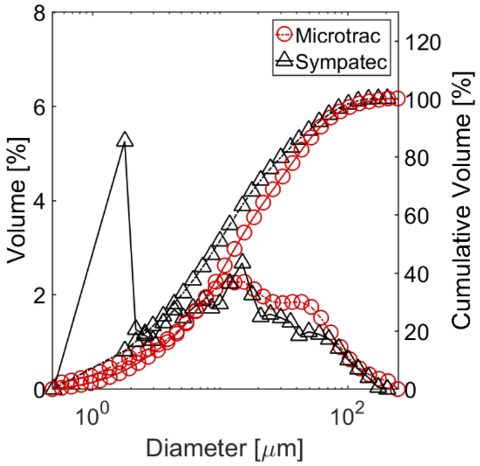

Figure 15. Particle size distribution from two dispersion units: Microtrac and Sympatec.

With compressed air, particles were accelerated to velocities up to 100 m/s, generating a well dispersed particle in air suspension the width of the laser beam. The disperser and vacuum system are carefully designed to prevent any particle recirculation zones. Particles are extracted at the same flow rate in which they are ejected from the disperser.

When comparing the two PSDs from the different systems in Figure 15, a spike in the volumetric concentration for the Sympatec distribution is present a at particle diameter of 1.8 μm. The smallest size the system lens installed can capture is 1.8 μm, which is likely contributing the very large initial peak. The second peak lies at around 15 μm, which is close to the position of first peak for the Microtrac S3500. In Figure 15, an additional two soft peaks of data centered at around 30 μm and 60 μm are present, while the Microtrac system shows one peak centered between the intersection of the two soft peaks shown on the Sympatec PSD curve. Despite these differences, datapoints are very useful since smoothing algorithms are not applied to the data, like most laser diffraction systems, including the Microtrac S3500. It also sheds light on the difference between Fraunhofer and Mie theory measurements.

For this work, data from PTI, using the Microtrac S3500 and SDC, and that from Sympatec HELOS and Sympatec RODOS disperser are considered nominal. The former being a nominal distribution based on Mie theory, and the latter for Fraunhofer. These have been considered nominal because the sampling techniques used ensure distribution data includes measurement of all particles in the disperser. All particle size distributions measured by the Malvern Insitec ST97 and Sympatec HELOS from plumes ejected from the high-velocity particle-laden rig will be compared to these nominal distributions. Table 3 summarizes the systems and methods used for PSDs acquired in this work.

For this work, it is assumed that any particle that enters the rig must leave the rig exit. Therefore, any changes in particles size distribution measured are due to either one or a combination of the following: (1) rig limitations, where particles agglomerate from lack of dispersion, (2) non-homogeneous particle dispersion, and (3) limitations of the laser diagnostics used.

Sample Description	Laser Diffraction Model	Range [μm]	Particle Dispersing Method
Nominal Mie	Microtrac S3500	0.02 – 2800	Liquid suspension with cell
Nominal Fraunhofer	Sympatec HELOS	1.8 – 350	Air suspension without cell
Rig Mie	Malvern Insitec S97	0.25 – 1000	High-velocity particle-laden rig
Rig Fraunhofer	Sympatec HELOS	1.8 – 350	High-velocity particle-laden rig

Table 3. Summary of laser diffraction systems used.

4.4.4 Laser Diffraction Limitations

Researchers such as Kelly et al. [32], Vlachos and Chang [33] have discussed caveats for sizing non-spherical particles using laser diffraction systems. The results in this study shall investigate the difficulties in sizing particle of a non-spherical nature, by comparisons to the nominal data from PTI, which involved the use of a laser diffraction system that considers non-sphericity.

Another limitation of using laser diffraction for sizing particles is the concentration of particles. Loads must be high enough for valid and representative measurements. In general, systems are typically restricted to transmission levels of 50% – 95%. Transmission is a measure of light that is not diffracted by particles, and thus a measure of particle in air concentration. This is to ensure a high signal to noise ratio. Thus, when acquiring sizing data from high-velocity particle-laden flows, a greater volume of sand must be used during measurement, to meet this particle in air concentration requirement. This can increase the probability of light scattered from one particle to reflect onto another particle before reaching the receiver, which is undesirable for measurement accuracy, but unfortunately cannot be avoided. Also, since particle concentrations must be sufficient for ample signal to noise ratios, the concentrations are at least 10^2 times as high as that typically observed in an engine environment [39].

4.5 Design of Experiments

To perform a systematic analysis on the change in particle-laden flows with different experimental conditions, classical Design of Experiments (DoE) was used. DoE studies are primarily used in manufacturing and process industries. According to Allen, DoE methods are formal approaches for varying input settings in a systematic way and fitting models with data collected [42]. Astakhov reminds us that it is only under given uncertainties, that a DoE allows an experimentalist to establish a statistical correlation between a set of input variables with a chosen outcome of the system or process under study [43]. In DoE terminology, the uncertainties are called uncontrollable factors.

DoEs are a cost-effective and time-effective approach for determining factors or interactions of factors that affect an outcome. In DoEs, instead of keeping all terms constant, and changing one variable at a time, an experimental run has more than one factor altered. This is done to identify interactive factors, which is a combination of factors, instead of a single factor, that alters the outcome of a study. This is desirable in experimentation, since in most practical cases, outcomes are caused by a change in a combination of inputs, rather than a change in one input alone. The cost-effective and time-effective nature of DoEs will be explained below.

Experimental studies have adopted the experimental method for these reasons. For instance, Chen et al. performs a DoE to determine a model that represents fuel spray characteristics as a function of fuel injection pressure, viscosity, and air blast pressure [44]. Work by Nekouei et al. determine the most optimal experimental parameters for synthesizing ultra-fine copper particles by electrolysis. The mathematical model presented was used to predict the particle size synthesized at certain conditions. The predicted value matched closely to the experimental value [45].

Here, the main use of DoEs were to statistically fit response surface models that describe the particle size and concentrations of the high-velocity particle-laden environment, as well as reduce the amount of sand required to give conclusive results.

To acquire these models, Design Expert 11, a Stat-Ease, Inc. Software was used to perform regression analysis and analysis of variance (ANOVA) on experimental datasets to determine any linear, quadratic, or interactive relationships between input and output variables. Before describing the DoEs performed, the following terms are important and should be defined.

(1) Factor – the name given to input parameters to an experiment. Controllable and uncontrollable factors are the two types of factors in DoE. Controllable factors are those that would be altered in an experiment, while uncontrollable factors are those that occur inevitably but cannot be controlled and lead to uncertainty. It is important to note the possible effects these uncontrollable factors could impose on the results of the experiment.
(2) Interaction – an interaction occurs when a factor (input) influences the response (output) to a degree that is dependent on the setting or value of another factor (input).
(3) Response – the name typically used in DoE work to describe the output parameter being measured in the experiment. Ideally, these should be quantifiable.

4.5.1 DoE1- Screening DoE

The first DoE, DoE1, was used to screen factors significantly affecting the responses, the measured characteristics of the particle-laden flows. Screening experiments are usually two-level factorial, 2^k, designs. These experiments involve measuring the response of a system from changing factors between only two values, called levels. These levels are labelled high and low. Factor effects determined are essentially the difference between the average of all runs at the two levels for a factor.

A factorial design could be either full-factorial or fractional-factorial. A full-factorial design has 2^k runs, where k is the number of factors. So, in the case of five factors being investigated, the number of runs for a full-factorial design would be $2^5 = 32$. Fractional-factorial designs enable conclusions to be drawn with less runs performed. Here, a half fractional-factorial design was chosen, so that only 16 runs had to be performed. The reliability of these designs is based on the sparsity of effects principle, which states that, in general, responses depend on a few main factors and low order interaction factors. Here, a low order interaction factor means interactions between two or three terms, and high order interaction factor would be interactions between a larger number of factors.

The factors to screen were: flow velocity, laser beam location, particle feed rate, eductor supply pressure, and rig length. The responses were measured by the Malvern Insitec ST97 laser diffraction system, and included Dv50, the particle distribution median, Dv10, the 10th percentile size of the distribution, Dv90, the 90th percentile size of the distribution, D32, Sauter Mean Diameter, a measure of volume over surface area for a given measurement, and transmission, the fraction of light that is not scattered by particles in the measurement plume – the greater the transmission, the lower the particle in air concentration.

The above factors were postulated to be parameters affecting particle-laden conditions and thus measurements. With statistical reasoning, the DoE results would provide a means of determining which of these initially selected factors most significantly affected the flow environments. Flow velocities, particle feed rate, and eductor supply pressure were hypothesized to provide environments that may affect particle trajectory or motion. Checking for any changes in particle-laden environments from shortening the rig length was important to determine whether developing flows present in the shorter rig, as opposed to more developed flows in the longer rig, would alter particle size values measured. The effects of the laser beam height with respect to the rig face was also investigated because it was hypothesized that particles do not distribute homogeneously within the rig profile, due to gravitational forces on particles.

Experimental conditions comprised of combinations of upper and lower factor settings. These were established and randomized by the DoE software. A summary of DoE1 conditions is shown in Table 4. For flow velocity, higher flow velocities were achieved by increasing compressed air pressure supplied to the rig. The laser beam location was varied by altering the rig height on a 3-axis traverse, so that the laser beam cylinder covered a different section of the rig profile, as shown in Figure 16. The center of the 10 mm diameter laser beam was positioned at a vertical height of 6.35 mm above and below the centerline for the upper and lower level, respectively. Unfortunately, at distances greater than 6.35 mm away from the centerline, signal to noise levels were not high enough to acquire laser diffraction measurements. Otherwise, measurements up until the edge would have been beneficial. The particle feed rate was altered via controls on the AccuRate screw feeder. Changes in compressed air pressure gave the two levels for eductor pressure. Finally, the rig length was altered by switching the smooth pipe section linked to a pipe connector, furthest downstream. The particle injection point is 0.406 m upstream of the connector. The pipes were 0.152 m and 0.305 m long, with an inner diameter of 26.7 mm, giving L = 6D and L = 10D respectively. Pipe lengths are measured from the pipe connector, since the connector gives slight deviation in the section inner diameter.

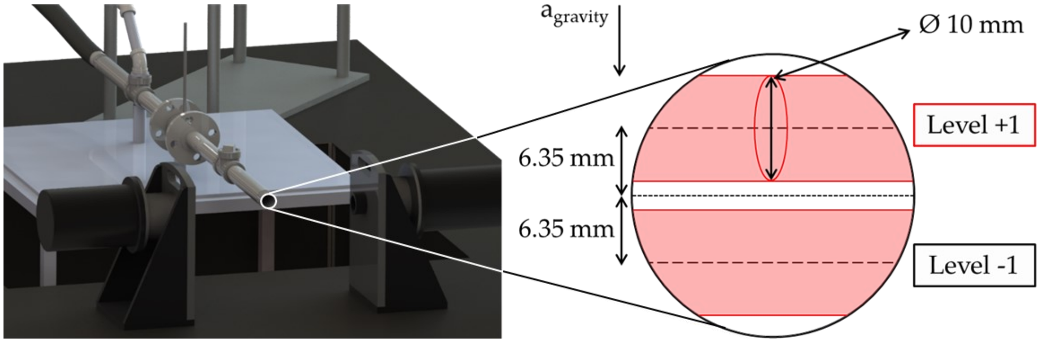

Figure 16. Higher and lower level laser beam location for DoE1.

Level	Flow Velocity [m/s]	Distance from Centerline [mm]	Particle Feed Rate [g/s]	Ejector Pressure [psig]	Rig Length [m]
-1	65	– 6.25	0.25	20	0.152
+1	125	+ 6.25	0.50	60	0.305

Table 4. Summary of testing conditions for two levels for DoE1.

As for responses, the median particle size, Dv50, was chosen for its intuitive nature, being the size of the particle corresponding to the center of the distribution. Dv10 and Dv90, the 10th and 90th percentile of the distribution were also measured because they give insight on the distribution spread, and whether changes exist for the smaller or larger particle population. These three size parameters can also be used to describe the PSD, since distributions are typically complex, and cannot be described by one parameter alone. D32 was also chosen for its physical meaning. The value of D32 can be used to indicate the presence of smaller particle being present. The D32 is defined as:

$$\mathrm{D32} = \frac{\sum \mathrm{D}^3 \cdot \mathrm{n}}{\sum \mathrm{D}^2 \cdot \mathrm{n}} \tag{4}$$

Where D is the square root of the upper bin multiplied by the lower bin. And n is the volumetric percentage within that bin. Therefore, for a given volume (D32 numerator), if a smaller D32 is measured, this infers that the surface area of that volume of material (D32 denominator) is greater. And since smaller particles give greater surface area, smaller particles must be present. In addition, D32 is sensitive for smaller particles, which is of interest in this study. Transmission was also studied to detect any discernable concentration segregation of particles within the plume cross-section.

4.5.2 DoE2 – Response Surface with Malvern Insitec ST97

The screened factors from DoE1 were then studied further in a Box-Behnken response surface design (DoE2), using the same laser diffraction unit, the Malvern Insitec

ST97. This experimental design was conducted to provide an in-depth analysis of the relationships between factors and responses. It requires runs with at least three different experimental factors, each with three levels, where the middle level is a center point between the upper and lower levels. Here, five center points were used to test for curvature in models, which was not evaluated in DoE1. The test conditions of these levels are summarized in Table 5. Based on DoE findings, eductor pressure was maintained at 80 psig and the length of the end pipe section fixed at 0.254 m. The flow velocities were increased to include that of interest: 200 m/s. Consequently, particle feed rates were increased to produce sufficient signal to noise ratios for the laser diffraction system measurements. The locations of measurement included a center point. These points overlap one another as shown in Figure 17.

Level	Flow Velocity [m/s]	Distance from Centerline [mm]	Particle Feed Rate [g/s]
-1	100	– 6.25	1.33
0	150	0	1.50
+1	200	+ 6.25	1.67

Table 5. Summary of testing conditions for three levels for DoE2.

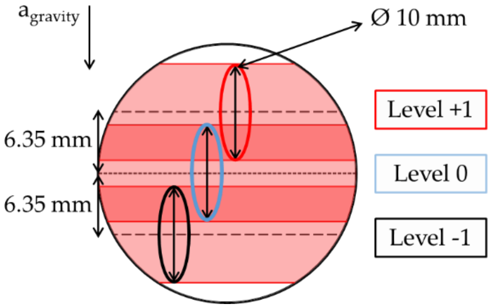

Figure 17. Three levels of laser beam location for DoE2, with 10 mm diameter beam.

An additional response was evaluated in DoE2 and in DoE3: D43, the DeBroukere mean. It is a measure of the mean diameter weighted by the volume. Unlike D32, is more sensitive to changes in larger particle sizes, and is defined by:

$$\mathrm{D43} = \frac{\sum \mathrm{D}^4 \cdot \mathrm{n}}{\sum \mathrm{D}^3 \cdot \mathrm{n}} \tag{5}$$

4.5.3 DoE3 – Response Surface with Sympatec

A third DoE, DoE3, adopting the same Box-Behnken response surface design as DoE2 was then carried out. For this, the Sympatec HELOS was used. This was performed to assess variation in laser diffraction systems and their accompanying theories (Fraunhofer, as opposed to Mie) used to convert diffraction patterns from the receiver into particle size distributions. Like DoE2, eductor pressures were kept at 80 psig, and end pipe length at 0.254 m.

Fortuitously, transmission levels were sufficient for the Sympatec when particle feed rates were lowered. Reduced particle feed rates were used to be cost-effective, and to investigate changes in measurements at lower particle loading. Also, the increased laser beam diameter was valuable, providing ensemble particle size measurements for least 99.4% of the pipe cross section. Table 6 and Figure 18 describe the test conditions for DoE3.

Level	Flow Velocity [m/s]	Distance from Centerline [mm]	Particle Feed Rate [g/s]
-1	100	– 6.25	0.50
0	150	0	1.00
+1	200	+ 6.25	1.50

Table 6. Summary of testing conditions for three levels for DoE3.

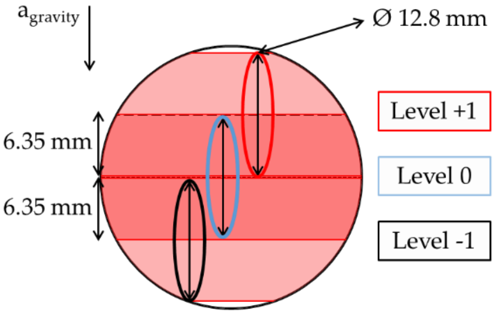

Figure 18. Three levels of laser beam location for DoE3, with 12.8 mm diameter beam.

4.5.4 Particle Ingestion through Side Wall

To further assess the non-homogeneity of the particles within the profile exit, particles were red into the rig through the side wall. Injected from the left, when viewing the face of the exit profile. All conditions, including particle feed rates, flow velocities, laser diffraction system, and laser beam location measurements were the same as that in DoE2.

4.5.5 Reduced Rig Diameter

The final set of data acquired was for a reduced with diameter of $D_2 = 21.1mm = 0.75D_1$. This was performed to assess whether the same trends were observed, even for a smaller diameter. The flow velocities and laser diffraction system used in DoE2 were used for this investigation. However, the laser beam was positioned at half the distances from the centerline as that in DoE2 and DoE3. And the particle feed rate was kept at 1g/s. These conditions are highlighted in Table 7. It is noted that at this reduced diameter, the velocity conditions could not be reduced lower, unless the sonic orifice plate which would be undesirable in this work.

Level	Flow Velocity [m/s]	Distance from Centerline [mm]
-1	200	– 3.125
0	220	0
+1	240	+ 3.125

Table 7. Summary of testing conditions for particle sizing through reduced rig diameter, at 1 g/s.

4.5.6 Data Acquisition and Model Selection

Care was made to ensure that the dataset contributed to adequate power, a measure of signal to noise ratio, by performing sufficient runs. Also, the population means of lower and upper level samples, plotted as end points in the factor plots, are calculated with a confidence interval of 95%. This means that if an experienced experimenter conducts this experiment again, they are 95% likely to obtain the same results obtained in the models, within the ranges of the experimental conditions chosen. Allen describes the equations used to perform the ANOVA on the data [42].

Models are fitted to data using least squares. To confirm that all models are representative of the data, certain ANOVA values were scrutinized. These values were

F-values, p-values, and Adeq Precision, all summarized in the Appendix. These values come from F-tests, which involve the F-distribution. F-values are values on the theoretical F-distribution, and are used to support or reject the null hypothesis. The null hypothesis states that there is no difference between the means of groups of data. The groups of data are those under the same factor level. Since the F-value is a ratio of variation between sample means and variation within the samples, the value is expected to equal 1, under the null hypothesis. However, a large F-value means that the two means are in fact not equal, and the null hypothesis that the group means are equal is rejected.

To know whether a large F-value was actually large enough, the model p-value is used. P-value is the probability of obtaining an F-value that is at least as large as the value obtained in the study. To do this, the F-value obtained is placed in the F-distribution. The p-value allows us to determine the probability of getting the F-value that was calculated, assuming the null hypothesis is true. If the probability, and thus p-value is low enough, then the null-hypothesis can be rejected. If the probability is high, it signifies that the large F-value obtained is likely due to noise. Models and model terms with p-values less than 5% are typically deemed significant. Thus p-values were checked to ensure values were less than 0.05. Adeq Precision is a measure of signal to noise from the data. A value greater than 4 is significant for the model to be valid.

Several model diagnostic tools were also assessed. Plots of externally studentized residuals versus predicted points were checked for a random scatter of points to ensure there were no systematic errors in results. A non-random scatter may have a diverging or converging shape to the overall scatter plot. The Box-Cox plot was used to confirm that no model transformation should be applied to the data. A transformation would be necessary if the ratio between the maximum and minimum response value was greater than 10. Cook's Distance is used to determine outliers in the data based on the threshold. Cook's Distance measures the change in least squares regression analysis when an individual run or point is excluded in fitting the model. Therefore, if the Cook's distance is large for a particular run, it has strong influence on the data, and is an outlier, and the model should be reconsidered. Factors were thoroughly considered. Final models were selected based on sound ANOVA diagnostic results.

4.5.7 Uncontrollable Factors

Uncontrollable factors should be identified and taken into consideration in each experiment, to minimize their effects on the study. In this work, all runs for each DoE were acquired on the same day. This was done to minimize systematic errors from variance in laser diffraction alignment or compressed air conditions that may vary day to day. Also, the laser diffraction system was warmed up for at least 30 minutes before the run, for a steadier laser power supply. Whenever possible, runs were performed in a randomized order.

4.6 Rig Plume Imaging

The exit of the rig plume was imaged to detect particle dispersion and segregation. A diode laser beam was projected into a laser sheet via a cylindrical lens. The sheet was positioned around 50.8 mm away from the plume exit to reduce any laser light reflection from rig surfaces. A Nikon D90 camera was used capture light scattered from plume particles. Images were converted to 8-bit grayscale, where each pixel has a value between 0 and 255, measures of intensity. The intensities for each condition were plotted in colormaps to illustrate regions of brightness, associated with more light scattering, and thus an indication of either greater particle surface area, greater number of particles, or both.

4.7 Evaluation of Forces Acting on a Particle in an Air Stream

To gain a better understanding of possible causes for non-homogeneous particle dispersion, forces acting on particles when travelling in an air stream were evaluated. The ratio of horizontal drag forces to vertical gravitational forces, $F_{h/v}$ were assessed to determine the distance a particle can travel before colliding with the rig floor.

For this, the following assumptions were made: radial air flow velocity component is negligible compared to axial air flow velocity component; particles are injected vertically downward, as in DoE2 and DoE3, and are only subject to gravitational acceleration, with negligible forces acting on particles from the eductor compressed air. The system is also assumed to be under isothermal conditions, so thermophoretic forces are neglected. From the Newtonian equations of motion in a Lagrangian framework, the forces on one particle can be taken to be:

$$m_p \frac{d\vec{c}}{dt} = \overrightarrow{F_d} - \overrightarrow{F_g} + \overrightarrow{F_x} \tag{6}$$

Where m_p is the mass of one particle of a given size, c is the particle velocity, F_d is the drag force and F_g is gravitational force. F_d acts in the same direction as the fluid flow. This is because the force opposes the motion of the particle relative to the surrounding fluid. The fluid surrounding the particle moves towards the right. The particle moves to the left, relative to this fluid. Thus, the drag force acts towards the right, to oppose the motion. To simplify the force balance further, other factors that would affect drag, such as particle collisions, pipe roughness, particle rotation, wall effects and electrostatic effects, represented by F_x are neglected here, reducing the equation further to:

$$m_p \frac{dc}{dt} = F_d - F_g \tag{7}$$

The ratio of horizontal forces to vertical forces, a measure of height lost due to gravity for a particle conveyed by air can be found by:

$$F_{h/v} = \frac{F_d}{F_g} \tag{8}$$

The equation for Fg is:

$$F_g = (m_p - m_f)\, g \qquad ((9)$$

Where m_p is the mass of the particle, m_f is the mass of the fluid displaced by the particle, and g is gravitational acceleration.

While the equation for the drag force acting on a particle for horizontal transport is given by Klinzng as [38]:

$$F_d = m_p \frac{C_d}{d_p}\left(\frac{\rho_f}{\rho_p - \rho_f}\right)(\, v - c\,)^2 \tag{10}$$

Where C_D is the drag coefficient, d_p is the particle diameter, ρ_f is the density of the fluid, ρ_p is the density of the particles, w = v – c is the relative velocity between the gas and solid. Shamlou derives a similar form of the equation from a vertical differential balance [46]. The equations found from this balance for drag forces is also applicable to horizontal transport.

To obtain the drag coefficient, the drag coefficient curve, which plots C_D versus particle Reynolds number can be used. Curves for non-spherical particles, instead of the standard drag curve, have been used here, to account for the non-spherical nature of AMTD, increasing the drag on particles. In assuming the largest particle size in the particle size distribution to be 200 μm, the particle Reynolds number can be determined by:

$$Re_p = \frac{v\, d_p\, \rho_f}{\mu_f} \tag{11}$$

Where v is the fluid stream velocity and μ_f is the fluid stream velocity.

The non-sphericity of particles is determined by the shape factor. Numerous definitions for shape factor exist. But for the drag of a particle in fluid flow, shape factor, sphericity, ψ, is used. This is defined as the ratio of the surface area of a sphere with the same volume as a particle, d_v, over the surface area of that particle:

$$\psi = \frac{\pi \, d_v^{\,2}}{s} \tag{12}$$

The value ranges from 0 to 1, where sphericity of a spherical particle is 1. The less spherical the particle, the closer the value to 0. Given the non-rounded and non-spherical nature of AMTD, a sphericity of 0.1 was assumed.

The velocity of a single particle was empirically found by Hinkle, to be:

$$c = v\,(1 - 0.68\, d_p^{\,0.92} \rho_p^{\,0.5} \rho_f^{\,-0.2}\, D^{\,-0.54}) \tag{13}$$

5

RESULTS AND DISCUSSION

5.1 Single-Phase Flow Validations

The velocity profiles obtained from pitot tube point measurements, as described in the methodology are shown in Figure 19 – Figure 22. Measurements closer to the wall edge were not possible, due to pitot tube thickness. Curves are fitted from the seven data points measured. The locations of measurements have been normalized to the inner radius of the pipe, 26.7 mm. For Figure 19, negative radial location signifies the left of the pipe face, positive signifies the right, when viewing normal to the high-velocity rig exit profile. Flow travels from top to bottom. Figure 20 is the vertical velocity profile viewed as if flow travels from left to right. Positive radial locations correspond to the top of the rig, negative radial locations correspond to the bottom. A dotted line has been included to facilitate observing profile symmetry.

Interestingly, both the horizontal velocity profile and vertical profiles are not symmetric. This may have been due to the pipe connector, connected to the end pipe, and positioned 0.254 m upstream of the rig exit. It may have caused the cross-sectional area of the pipe to vary, disrupting the flow. For the horizontal profile in Figure 19, another cause of asymmetry may be from the orientation of flex hose connected to the high-velocity rig. A section of flex hose connects the compressed air line, with a sonic orifice plate installed, to the rig. Since this hose is not clamped in place, it is possible that when compressed air flows through, the hose centerline and high-velocity rig centerline do not lie on the same axis, causing the flow velocity maximum to be shifted slightly towards the right of the rig face, at r/R = 0.25. The same applies to the peak in Figure 20, which is slightly higher than the centerline at around r/R = 0.2. The flex hose connects to the rig from the ground up and may be shifting the peak towards the top of the profile face. Alternatively, the eductor could be contributing to the slight asymmetry.

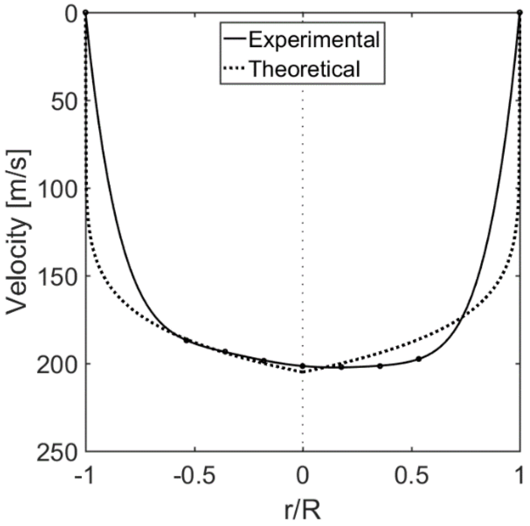

Figure 19. Horizontal velocity profile.

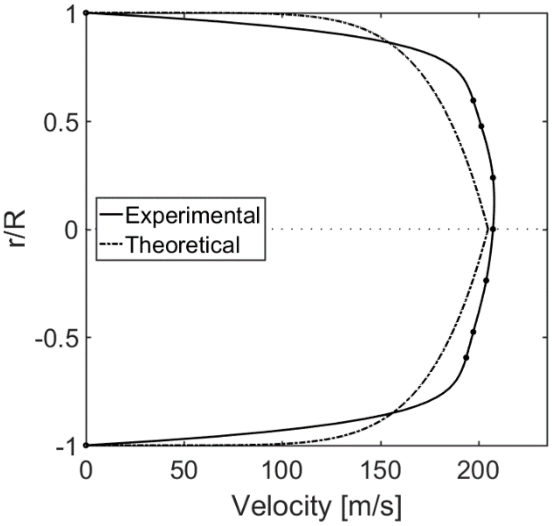

Figure 20. Vertical velocity profile.

Overall, both the horizontal and velocity profiles are flat, indicating that the turbulent pipe flow may be fully developed at L = 12D, matching less conservative correlations for fully developed flow of L = 10D [47]. The theoretical power-law velocity profiles for fully developed turbulent flows has been plotted to compare to experimental profiles:

$$V = \left(1 - \frac{r}{R}\right)^{\frac{1}{n}}$$

Where R is the pipe inner diameter and n is a constant dependent on Reynolds number. A value of n = 8 was chosen, based on Reynolds of around 3.5×10^5 at 200 m/s [47].

Laser diffraction measurements were to be measured at multiple vertical positions, so the vertical profiles were investigated further. Point velocity flow measurements were acquired for various mean velocities. Mean velocities were approximated from extrapolating laminar flow element calibration curves, assuming linearity was held for higher flow rates. These calibration curves give the relationship between volumetric flow rates and pressure supplied to the high-velocity rig. Figure 21 plots velocity profiles created by fitting seven point velocity measurements. As expected, the profile velocities increase with increasing mean velocity, around the velocity of interest, 200 m/s. The slight dip in the absolute velocity for the 200 m/s case at around r/R = 0.5 is likely a random error in measurement. To illustrate asymmetry across all the velocity profiles, the velocities were normalized by the mean velocity of each profile. Figure 22 shows the result of normalizing the profiles. Profiles collapse along the same curve, indicating that this slight asymmetry exists across a range of velocities. Given that these flows are already fully developed even at 200 m/s, lower velocity flows are expected to follow a similar trend, since the entrance length would be even shorter.

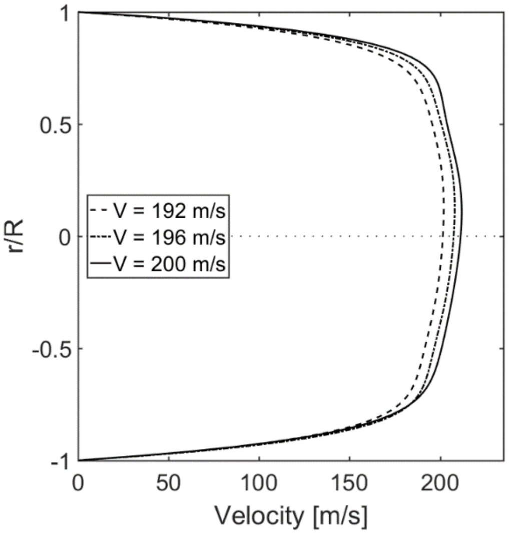

Figure 21. Vertical velocity profile for various mean velocities.

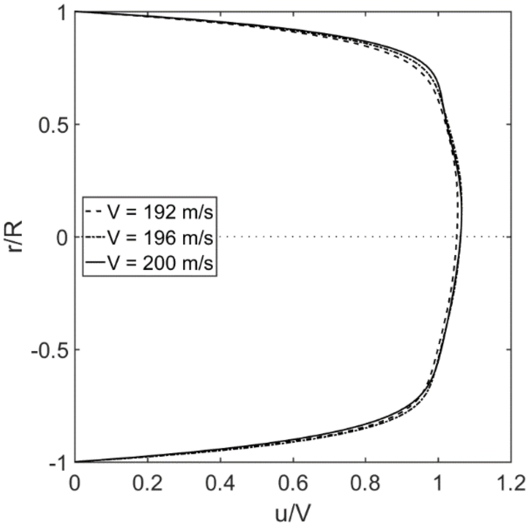

Figure 22. Normalized vertical velocity profiles for various mean velocities.

For the following discussions, since laser diffraction measurements were recorded for various vertical locations across the profile face, r(+) will be used to represent measurements where the laser beam covers the higher level settings, and r(-) denotes measurements for lower level settings. For surface responses with center points, regions are labelled as r(0). Radial locations of the laser beam edges are summarized in Table 8.

DoE	Level -1 – r(-)	Level 0 – r(0)	Level +1 – r+
1	-0.85R – -0.025R	N/A	+0.025R – +0.85R
2	-0.85R – -0.025R	-0.38R – +0.38R	+0.025R – +0.85R
3	-0.96R – -0.002R	-0.48R – +0.48R	+0.002R – +0.96R

Table 8. Laser beam edge location during measurement.

5.2 DoE1 – Screening Factors

The first DoE was performed to identify factors that govern the transmission levels [%], particle size distribution 10th percentile of distribution Dv10 [µm], median Dv50 [µm], 90th percentile of distribution Dv90 [µm], and Sauter mean diameter D32 [µm]. It should be noted that model curvature, that involves center point measurements, was not investigated in this screening study. Curvature was studied in DoE2 and DoE3. Despite curvature not being assessed, these model coefficients can still be used for values at the low and high level settings used. The model equations coefficients where A: flow velocity, B: laser beam location, C: feed rate, D: ejector pressure, E: rig length, and interaction factors, the product of coefficients. Model equations are summarized in Table 9. They are in coded factor form. This means that to obtain the value of the response (output) using the model equations coefficients, "-1" must be inputted for a low-level factor setting and "+1" for a high-level setting. In the equations, the magnitude of factor coefficients is an indication of how significantly the factor affects the response. The signs of the factors determine whether the factor positively or negatively affects the response.

Response	Mean	A	B	C	D	E	AB	DE
Transmission	94.09	2.629	-0.484	-1.311	-2.102	0	52.96	0
Dv10	4.694	0.365	0.453	0.197	0	0	0	0
Dv50	26.62	7.417	2.686	0	0	0	5.197	0
Dv90	n/a							
D32	9.622	1.315	1.333	0	0.401	0.443	0.913	-0.852

Table 9. Response model equation coefficients for DoE1.

5.2.1 Factors Governing Dv10, Dv50, and Dv90

The predicted model response, as a function of model coefficients in Table 9, versus actual experimental values for Dv10 is plotted in Figure 23. As indicated in Table 9, values of Dv10 depend on flow velocity, particle feed rate, and laser beam location. The ANOVA statistics F-value and p-value reveal that both the model and all three factors are significant. All three terms are positive, as shown in Figure 25 – Figure 27, so at the higher level of each factor, a greater Dv10 value was obtained. Laser beam location has the greatest impact on the response, followed by flow velocity, and finally particle feed rate.

The first 10% by volume of particles in r(+) should be comprised of larger particles than those at the bottom of the rig, in r(-). With increased velocity is increased Dv10. Particle feed rate also increases causes Dv10 values to increase. Dv10 measurements are highly sensitive to changes in the smaller particles. So, an increase in Dv10 from increased particle concentration could be an indication that clumps of agglomerated sand of around 5 μm in diameter may have been captured during measurements.

According to the ANOVA results for Dv50, the only significant factor in the model is flow velocity. The other terms were included in the model because while these terms were deemed statistically insignificant from a p-value perspective, they contribute to a statistically significant model. Excluding these terms was attempted but led to undesirable diagnostic results. The predicted versus actual points is shown in Figure 24.

Despite this, the p-value for the flow velocity and laser beam interaction was 0.0599, which is close to 0.05, and thus plays a relatively high role in the value of Dv50. Figure 28 shows the interaction plot of distribution median for a combination of flow velocity and laser beam location. An interaction is indicated by the different slopes of these lines. Flow velocity has a different effect on transmission, depending on whether the laser beam is positioned at r(+) above the centerline, coded by "+1" and the red line, or positioned at r(-), below the centerline, coded by "-1" in black.

This interaction factor is an indication of heterogeneous dispersion within the rig. If homogeneous dispersion were to exist in the flow, particle mean sizes should be consistent throughout. For both rig locations, at higher velocities, the Dv50 is higher. The degree of significance of increased flow velocities for Dv50 in r(+) is demonstrated by the greater model line slope.

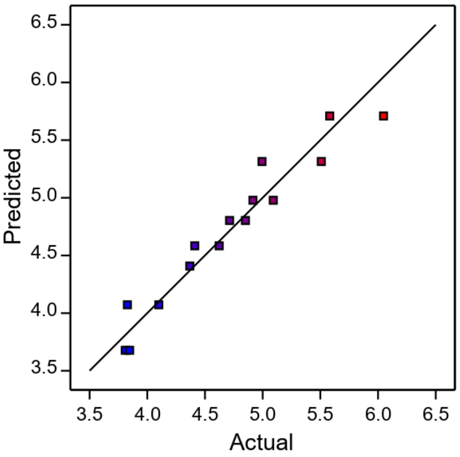

Figure 23. Predicted versus actual Dv10 model points.

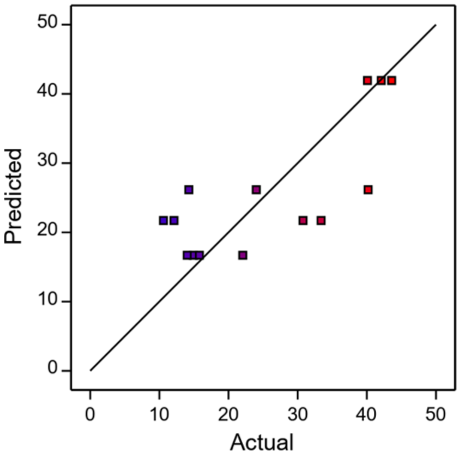

Figure 24. Predicted versus actual Dv50 model points.

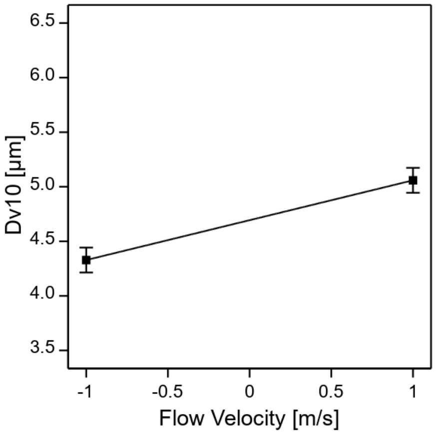

Figure 25. Main effect plot of Dv10 versus flow velocity.

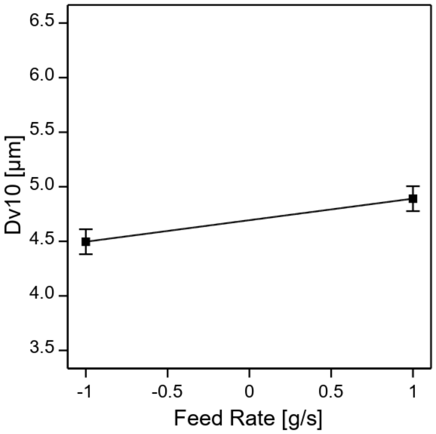

Figure 26. Main effect plot of Dv10 versus particle feed rate.

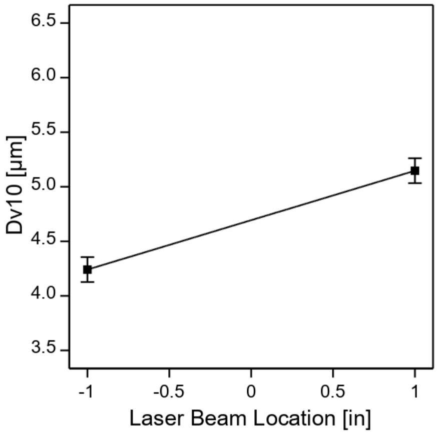

Figure 27. Main effect plot of Dv10 versus laser beam location.

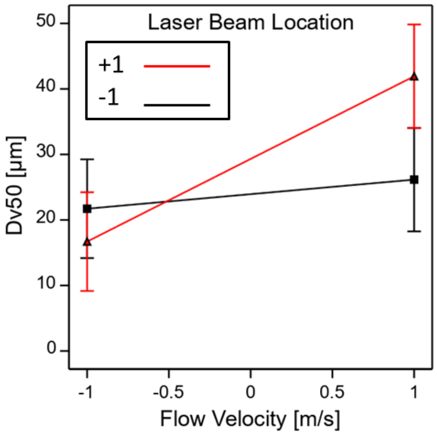

Figure 28. Interaction plot of particle distribution median for combinations of flow velocity and laser beam location.

Interestingly, it was not possible to determine a significant model that characterized Dv90. This was deemed promising, because even though there may have been agglomeration of smaller particles, as seen from the Dv10 dependence on particle feed rate, there was no significant dependence of particle feed rate on Dv90. A lack of correlation between particle feed rate and Dv90 is an indication of a well dispersed particle-laden flow.

5.2.2 Factors Governing D32

Figure 29 shows the predicted model points against those experimentally measured for D32. Figure 30 and Figure 31 show the interactions between factors governing D32. A lower D32 is an indication of a greater number of smaller particles in a measurement. In view of this, for the range of flow rates measured, Figure 30 shows that a greater number of smaller particles are present at r(-), compared to r(+), since the magnitude of D32 is lower for the black line than it is for the red line. The plot also indicates that for both locations of the rig, smaller particles are measured at low velocity, versus high velocity flow conditions.

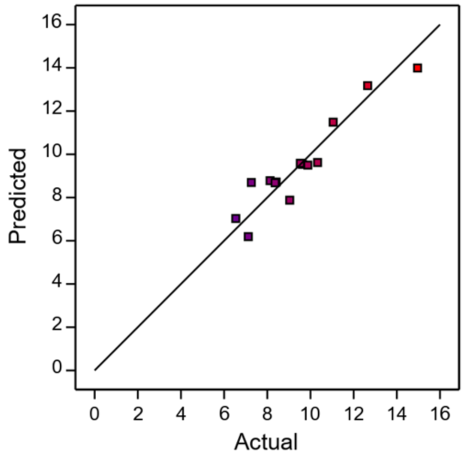

Figure 29. Predicted versus actual D32 model points.

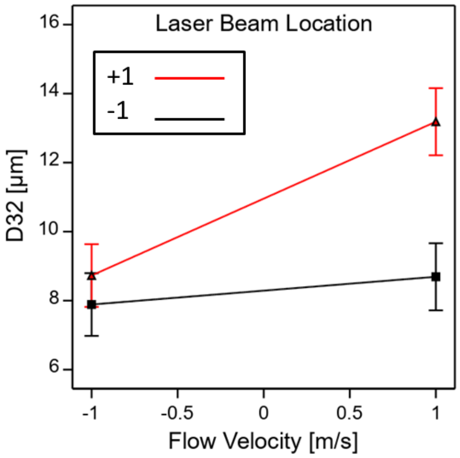

Figure 30. Interaction plot of D32 for combinations of flow velocity and laser beam location.

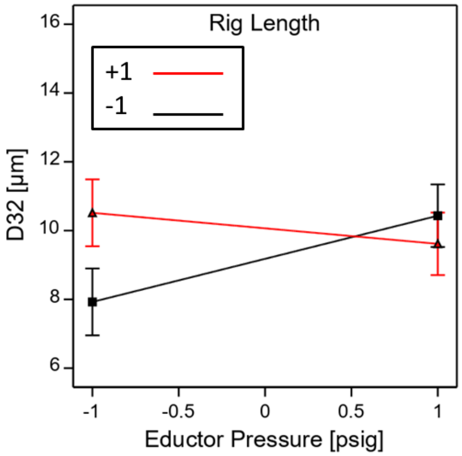

Figure 31. Interaction plot of D32 for combinations of eductor pressure and rig length.

Figure 31 shows the interaction plot where rig length and eductor pressure have interacting effects on D32. This plot shows that for a shorter rig length, increasing the eductor pressure increases the D32. Increased eductor pressure may mean more particles are ingested for a given time, so the particle in air concentration is higher. And increased rig length may mean more time for particles to disperse and deagglomerate from collisions or to fall from gravity. Therefore, for a shorter rig length, denoted by the black line, two possible scenarios could be contributing to this positive slope. At higher particle concentration from increased eductor pressures, particles may not have enough time to disperse within the rig, causing particles to be clumped together, giving rise to a larger D32. Another cause of the larger D32 could be the combination of higher particle concentration and less time for the large particles to fall from gravity. While for the longer rig length, the opposite effects may be in play.

5.2.3 Factors Governing Transmission

The factors governing the transmission model equation were flow velocity, laser beam location, particle feed rate, eductor supply pressure and an interaction factor, of laser beam location and flow velocity. The predicted versus experimental model values are shown in Figure 32. Since flow velocity and laser beam location were part of interaction factors, they are not discussed independently, and rather, as an interaction. Figure 33 shows the effects of transmission and particle feed rate. Given that transmission is a measure of light that is not scattered by particles, a greater transmission is an indication of lower particle in air concentration. Thus, the relationship obtained is as hypothesized. For lower feed rates, coded as “-1”, greater transmission is measured, meaning less light is scattered, and reduced particle concentration in the measurement zone. These results also indicated that the particle feed rate should be increased for more accurate laser diffraction measurements. They were therefore increased in succeeding experiments in DoE2 and DoE3.

As for Figure 34, where transmission is plotted for two levels of eductor pressure, lower factor conditions also gave rise to high transmission levels. This relationship was interesting, since it indicated that with a given particle feed rate, greater eductor pressure increased the particle in air concentration. This could be attributed to a greater volume of particles being ingested at a time, from a greater pressure differential existing within the eductor, when more compressed air is supplied. It also suggests that even though a larger volume of air should flow through the eductor with increased pressure supplied, this does not cause a dilution in particle in air concentration. Given that greater transmission levels were desirable, a higher eductor pressure was adopted for DoE2 and DoE3, to ensure reliable readings for the development of response surface models.

Figure 35 shows the interaction plot of transmission. Again, it is the dissimilar slopes that reflect the presence of an interaction. Flow velocity has a different effect on transmission, depending on whether the laser beam is positioned in r(+) above the centerline, coded by “+1” and the black line, or positioned in r(-) below the centerline, coded by “-1” in red.

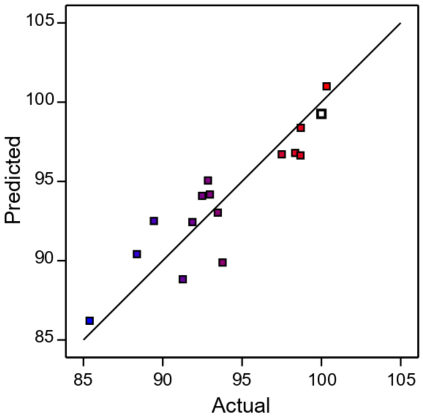

Figure 32. Predicted versus actual transmission model points.

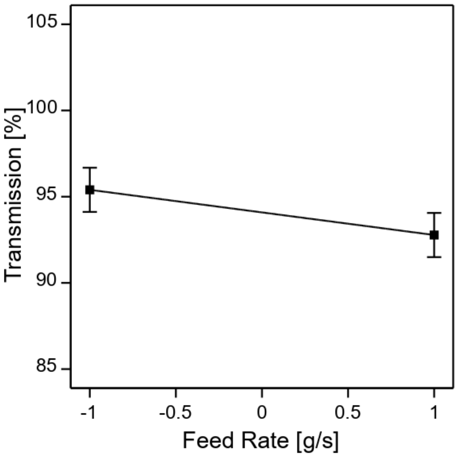

Figure 33. Main effect plot of transmission versus feed rate.

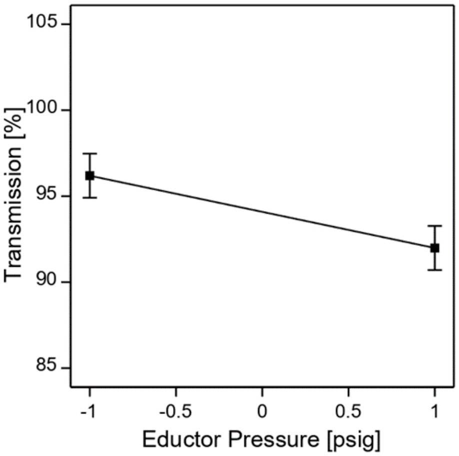

Figure 34. Main effect plot of transmission versus eductor pressure.

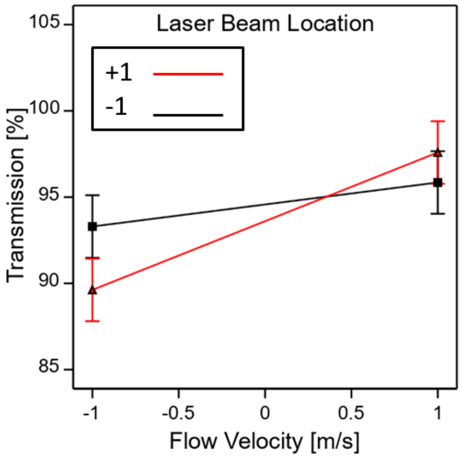

Figure 35. Interaction plot of transmission for combinations of flow velocity and laser beam location.

Similar to the Dv50 model, the transmission model reveals heterogeneous dispersion within the rig. For both scenarios, at lower velocities, the transmission is higher, indicating greater particle in air concentration. The lower velocities are produced by introducing reduced volumetric flow, providing less air flow for a given amount of sand fed into the rig. Therefore, the positive slopes in the plot are expected. However, since the slope of the red line is steeper than that of the black line, a change in flow velocity affects the transmission, a measure of particle in air concentration, to a greater extent for measurements acquired at the higher portion of the rig profile. This suggests that at higher velocities, the volume of particles residing in r(-) is less than that at r(+).

5.2.4 Outcomes of DoE1

Even though the range of conditions in DoE1 were lower than those of interest for investigation, it served as a time-effective and cost-effective method of providing insight to the setup of the response surface designs. Since the intended flow velocities of interest simulating gas turbine engine conditions were to be adopted in DoE2 and DoE3, possible effects of high flow velocities on particle size distribution were of interest. At the velocity conditions in DoE1, it was evident that particle size distributions were changing with velocity. This phenomenon was explored further at velocities ranging between 100 m/s and 200 m/s.

In addition, laser beam location was also of interest since discrepancies across the profile face are an indication of heterogenous particle dispersion. This is important to identify and model since heterogeneity may impact the particle size distribution of particles within rig, in which the commercial probes would be mounted for evaluation.

Next, since particle feed rate was a significant factor of Dv10 and is claimed to play a role in particle dispersion from a study by Sommerfield [25], it was also investigated in DoE2, as well as DoE3. Another reason for studying this further is, a lack of deviation in particle size distribution data from varying particle feed rate is a good indication of successful particle dispersion in air. This is especially important to assess since particle feed rates were increased to ensure sufficient laser diffraction signal to noise levels, especially with increased flow velocity conditions.

In terms of eductor supply pressure and rig length, these factors were kept constant during the remaining studies. A higher supply pressure was used to rule out contributions of agglomerated particles, so that the dispersion of polydisperse particles could be of a greater focus. A longer rig length was adopted. DoE1 showed that there might be some deviation in particle size distribution from measurements of different pipe lengths used for the upper and lower factor levels. The equation for entrance length for turbulent pipe flow is:

$$L = 4.4\mathrm{Re}^{1/6}D \tag{14}$$

Where L is entrance length, for which the flow is still developing, Re is Reynolds number, and D is the pipe inner diameter. Reynolds number ranges from Re = 1.74×10^5 to Re = 3.48×10^5 for flows of 100 m/s to 200 m/s. Based on this equation, for both levels, the flow is still developing at an axial distance of 26.7 mm. The boundary layer changes based on the flow velocity. The boundary layer of this developing flow is given by:

$$\delta = 0.37\ \frac{x}{\mathrm{Re}^{1/5}} \tag{15}$$

Given this, in DoE2 and DoE3, a 0.254 m long smooth pipe with an inner diameter of 26.7 mm was configured as the end pipe section. Since entrance length is governed by the above equation, this length would allow for boundary layer thicknesses that would potentially lie slightly above and slightly below the probe sensing region, if situated around 10 mm away from the probe face, and assuming the commercial probe would be flush mounted. This would allow for the particle size distributions to be characterized for near-wall flow conditions in which the probe would likely be subject to when in an engine. It would also give insight to the variance of particle size distribution measurements of sand around the boundary layer, suggesting particle sizes the probe may be missing, with a sensing region above the boundary layer.

5.3 DoE2 – Response Surface with Malvern Insitec ST97

This response surface served as a more rigorous investigation compared to the screening design. When including some center point measurements in DoE1, curvature was identified and predicted in the models. A response surface enables this curvature to be characterized. The main differences in DoE2, compared to DoE1, are (1) increased flow velocities to simulate an engine environment more closely, (2) increased particle loading to allow for reliable laser diffraction measurements, and (3) no changes in rig length. The model equations describing each response of interest is shown in Table 10.

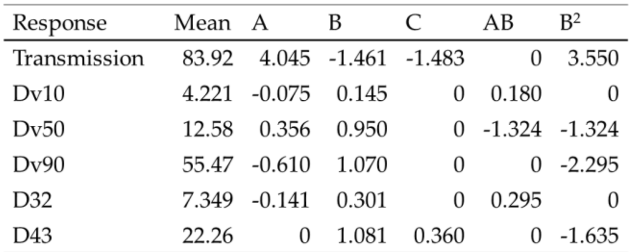

Response	Mean	A	B	C	AB	B^2
Transmission	83.92	4.045	-1.461	-1.483	0	3.550
Dv10	4.221	-0.075	0.145	0	0.180	0
Dv50	12.58	0.356	0.950	0	-1.324	-1.324
Dv90	55.47	-0.610	1.070	0	0	-2.295
D32	7.349	-0.141	0.301	0	0.295	0
D43	22.26	0	1.081	0.360	0	-1.635

Table 10. Response model equation coefficients for DoE2.

5.3.1 Factors Governing Transmission Higher Loads

Transmission levels, a measure of light not scattered nor reflected by particles, are plotted in Figure 37, Figure 38 and Figure 39. Results of Figure 37 are of no surprise. As previously indicated in DoE1, when flow velocities increase, particle dilution is greater, giving rise to less particles per unit volume, and higher transmission levels.

What is interesting, however, is that flow velocity and laser beam location is no longer dependent on an interaction, as shown in Figure 38. Instead, r(+) is subject to a higher concentration of particles, and the extent of particle dilution is the same in r(+) and r(-). The final significant factor affecting transmission is particle feed rate. The relationship is a combination of linear and quadratic, giving the curve in Figure 39. This indicates that the particle load affects the transmission levels up to a certain point, after which the transmission levels increase again slightly. It is intuitive to assume that particle in air concentration measured increases with particle feed rate. However, at a certain particle load, particle collision rates are enhanced, which in turn disperses particles, and may keep them from being trapped beneath viscous layers, increasing particle concentrations in the measurement region [25], [48]. This could be the cause of the increased transmission levels.

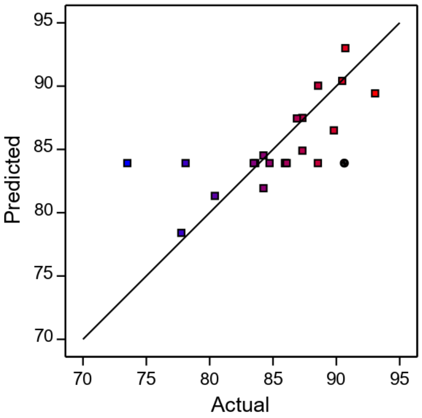

Figure 36. Predicted versus actual transmission model points.

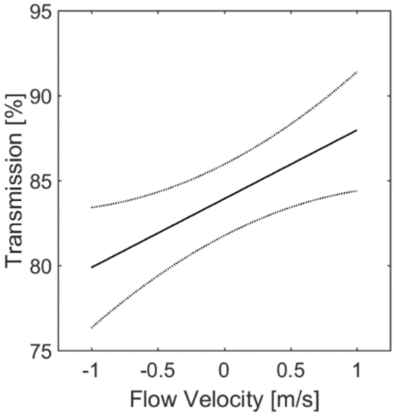

Figure 37. Main effect plot of transmission versus flow velocity.

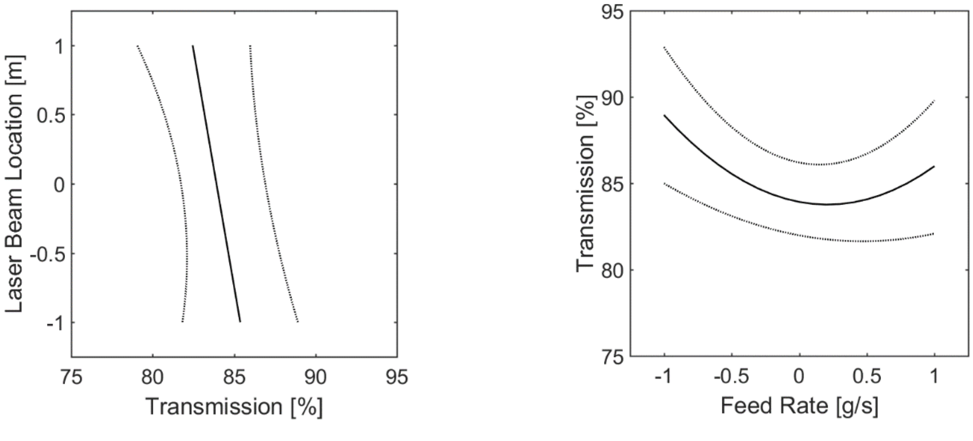

Figure 38. Main effect plot of transmission versus laser beam location.

Figure 39. Main effect plot of transmission and particle feed rate.

5.3.2 Factors Governing Dv10, Dv50, and Dv90 Higher Loads

To understand how polydisperse particles distribute within the rig profile, it is paramount to discuss the distribution parameters collectively. Figure 40 shows the model predicted terms versus the experimental measurements, while Figure 41 shows the interaction plot for Dv10. The significant effects for Dv10 are laser beam location and an interaction of laser beam location and flow velocity. For r(+), Dv10 increases with flow velocity, matching findings in DoE1, which involves lower flow velocities and particle loading. Interestingly, an interaction was not observed for Dv10 in DoE1. These differences may be in part due to the increased load, which ranged from $\Phi = 0.5 \times 10^{-3}$ – $\Phi = 4 \times 10^{-3}$ in DoE1 and was increased to $\Phi = 10.3 \times 10^{-3}$ – $\Phi = 27 \times 10^{-3}$ in DoE2. Increased load is seen to enhance particle-particle collisions, as shown in work by Sommerfield [25]. Another cause of discrepancies could be the elevated flow velocities.

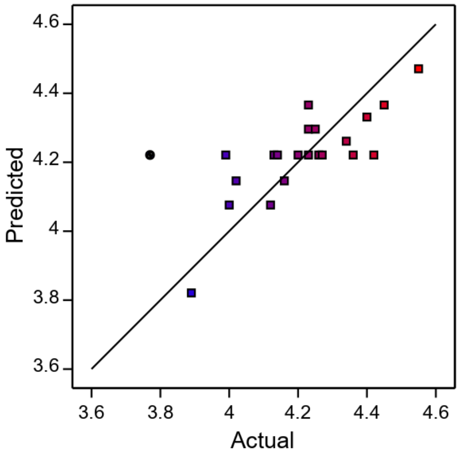

Figure 40. Predicted versus actual Dv10 model points.

The physical location of greater particle concentration, represented by lower transmission in Figure 38, is at r(+). This flow is signified by the "+1", and red line in Figure 41, and has a greater Dv10 at increased velocities. On the other hand, the more dispersed or diluted regions, in r(-) read a lower Dv10 at higher velocities. The cause of this interaction could be the dominance of different wall-bounded flow effects.

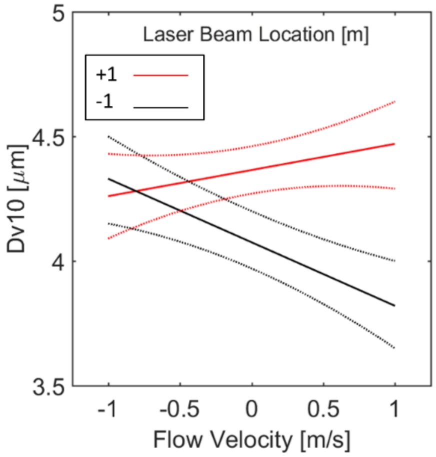

Figure 41. Interaction plot of Dv10 for combinations of flow velocity and laser beam location.

It is possible that in the r(-) region, particles are more influenced by turbophoresis, which is a feature of wall-bounded particle-laden flow, for which particles are accelerated towards the wall, causing an accumulation to exist near the wall beneath the viscous layer [49]. At the top portion of the rig, in r(+), particles may be less influenced by turbophoresis from the combination of increased particle concentration in this region, and velocities. This combination of effects gives rise to higher particle-particle collisions, which are said to reduce turbophoresis, whereby allowing trapped particles to be re-introduced into the bulk of the flow, by moving perpendicular to the streamwise flow. This effect has been shown for particles in fully developed flow turbulent flow by Zhang et al. [48].

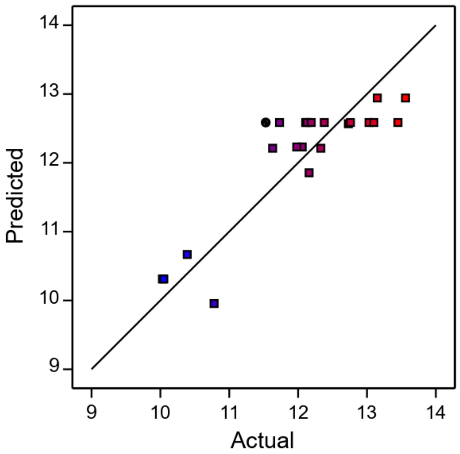

Figure 42. Predicted versus actual median model points.

Figure 43 and Figure 44 show the main effects of Dv50, while Figure 46 and Figure 47 illustrate those for Dv90. Laser beam location is a significant factor for both Dv50 and Dv90 and is quadratic. This behavior illustrates that a reduced volume of larger sized particles is present at r(+) and r(-). This reduction may be caused by turbophoresis, causing particles of a certain size to be trapped near the wall edges, and even shifting the entire PSD, making the effect present in the Dv90 model too. The asymmetry in the plots is also interesting, as it seems to match that of the velocity profiles. This similarity is discussed further in Section 5.9.

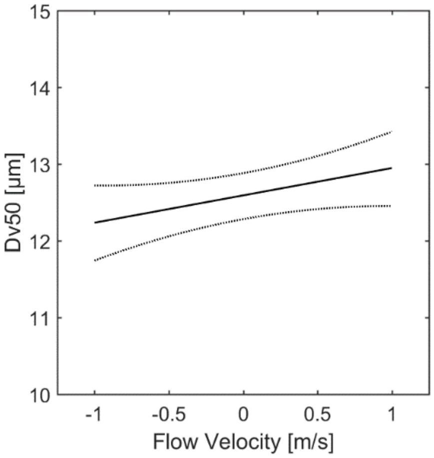

Figure 43. Main effect plot of particle distribution median versus flow velocity.

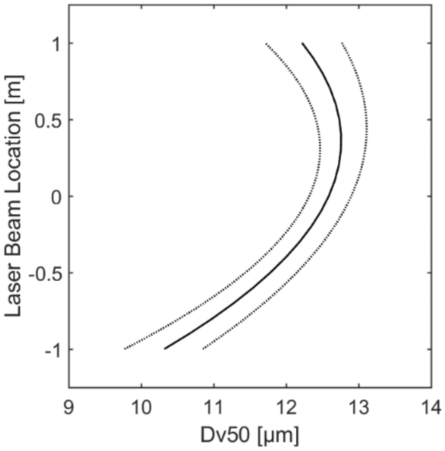

Figure 44. Main effect plot of particle distribution median versus laser beam location.

The less significant factor, flow velocity, causes Dv50 to increase, and Dv90 to decrease. For Dv50, increasing distribution median with increased flow velocity could be from reduced turbophoresis. At elevated velocities, this layer becomes thinner, housing less particles. The decrease in Dv90 at higher velocities could be attributed to the larger clumps deagglomerating.

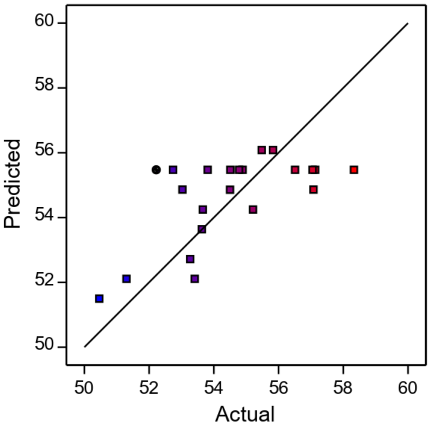

Figure 45. Predicted versus actual Dv90 model points.

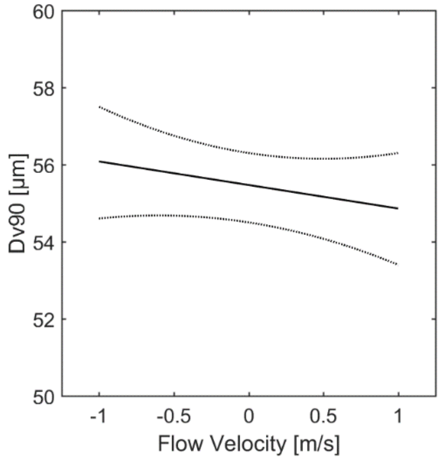

Figure 46. Main effect plot of Dv90 versus flow velocity.

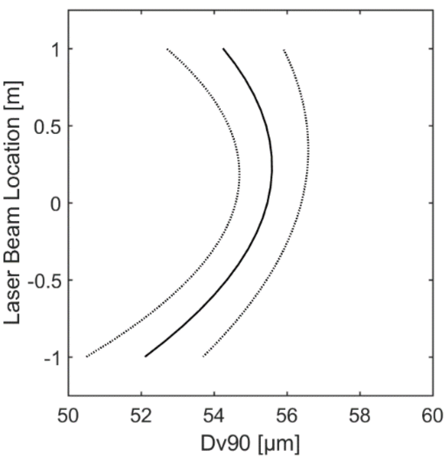

Figure 47. Main effect plot of Dv90 versus laser beam location.

5.3.3 Factors Governing D32 and D43 at Higher Loads

Figure 49 shows the interaction plot for D32, the PSD Sauter Mean Diameter. The interaction is significant in this model, and laser beam location is of second significance. According to the ANOVA, since the p-value of flow velocity alone is p-value = 0.064 > 0.05, it is deemed insignificant. However, it was included in the model, since doing so produced better diagnostics. The similarity in D32 with the Dv10 plot in Figure 41 is expected, since D32 is sensitive to changes of particles at the lower end of the distribution. Explanations of this relationship are similar to that of Dv10, whereby lower D32 measurements is obtained from the presence of a greater volume of small particles. The interaction may be caused by different levels of influence of turbophoresis. Increased particle-particle collision occurs at r(+), and so larger particles are mixed into the main plume, giving rise to a larger D32.

Finally, Figure 51 and Figure 52 show the effects of D43. This parameter is typically sensitive to larger particles. The curvature present in Figure 44 and Figure 47 is also shown in Figure 51. A peak particle size is captured at r(0), while a lack of these larger particles exists towards the wall edges, for r(+) and r(-). As for Figure 52, an increase in particle feed rate gives rise to a larger D43. This term did not have great significance in the model. However, this slight increase could be attributed to the increased levels of agglomeration from higher particle federate, that the D43 term is able to capture, since it is sensitive to the presence of larger particles.

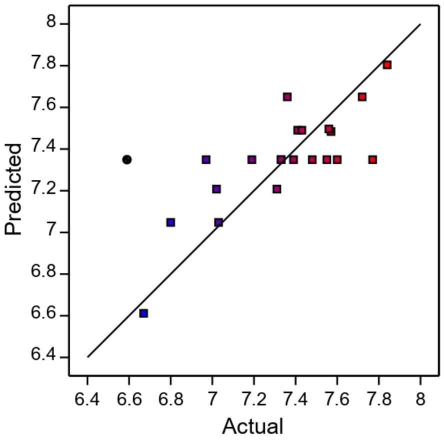

Figure 48. Predicted versus actual D32 model points.

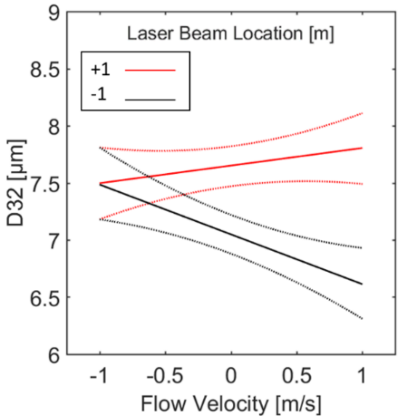

Figure 49. Interaction plot of D32 for combinations of flow velocity and laser beam location.

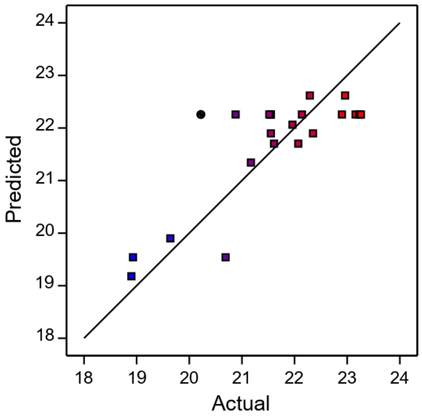

Figure 50. Predicted versus actual D43 model points.

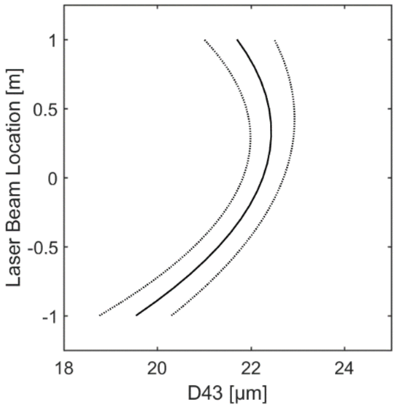

Figure 51. Main effect plot of D43 versus laser beam location.

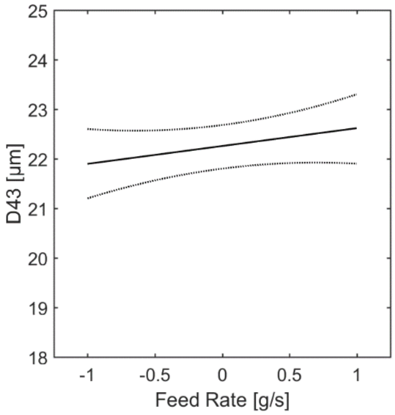

Figure 52. Main effect plot of D43 versus laser beam location.

5.3.4 DoE2 Particle Size Distributions

Plots of the particle size distributions with varying flow velocities, laser beam locations and particle feed rates are shown in Figure 53 – Figure 55. The AMTD curve is that from PTI, using the Microtrac S3500 in the dispersion cell, while the rest of the curves are acquired from the Malvern Insitec ST97 from the rig exit plume. The cumulative plot shows that the distributions are similar for particle sizes greater than 10 μm. The discrepancies from the lower particle end is likely due to the differences in lenses. The Microtrac used by PTI can measure particles as small as 0.02 μm, while the Malvern Insitec ST97 can only measure particles from 0.25 μm. In comparing the nominal AMTD from PTI, both show bimodality. Similarities beyond 10 μm are promising, and reveal that the particles within the plume tumble sufficiently to acquire PSDs akin to that measured by the Microtrac S3500 and the dispersion cell, the Microtrac SDC. The slight discrepancies in the magnitude of the data could be attributed to the different deconvolution model designs that convert light scattering patterns to PSDs.

Figure 53 shows how the PSD varies with flow velocity at the centerline for particle feed rates of 1.50 g/s. As the response surface has indicated, particle size parameters increase with velocity. The case of 200 m/s reveals a smaller peak at around 9 μm, compared to other velocities. For the 100 m/s curve, fewer large particles are measured compared to the remaining curves. This trend has been shown across a range of particle feed rates and rig profile locations. As shown, it is not very easy to identify the trends by eye; however, when assessing the particle size parameters from the DoE, the discrepancies are more evident. It should be noted that the maximum size measured does not increase with flow velocity. This indicates that a given particle size is not being overestimated system or viewed as a "stretched" particle by the laser diffraction at higher velocities. It also indicates that there may not be an optical limit, and particles can be successfully measured by laser diffraction up to 200 m/s.

Changes in PSD for laser beam locations at flow velocities of 200 m/s and particle feed are shown in Figure 54. At r(-) for level "-1", particle size distributions show a much greater first peak, and the second peak is shifted towards the larger particle size. Overall, however, as shown in the DoE2 results, these distributions have contributed to larger particle sizes appearing at level 0, r(0), and smaller particle sizes towards the wall, across all distribution size parameters. Again, these trends were apparent across most flow velocities and particle feed rates.

As most of the DoE2 model equations have shown, Figure 55 illustrates how the particle size distribution does not change with varying particle feed rates. Some slight discrepancies exist between the curves, but in comparison to those for varying flow velocities and laser beam locations, these discrepancies can be considered negligible.

A dataset of all particle size distributions for these test conditions investigated are available. Given the complexity of the particle size distributions, and the difficulty in describing a distribution accurately with one parameter, DoE2 models provide a means to rapidly determine the particle size distribution parameters, Dv10, Dv50, Dv90, D32, and D43, as well as concentrations, measured by transmission, as a function of the flow velocity, particle feed rate, and measurement location. This shall be valuable for commercial probe evaluations, where particle size distribution parameters can be predicted at the probe sensing zone, for given flow velocity conditions and particle feed rates.

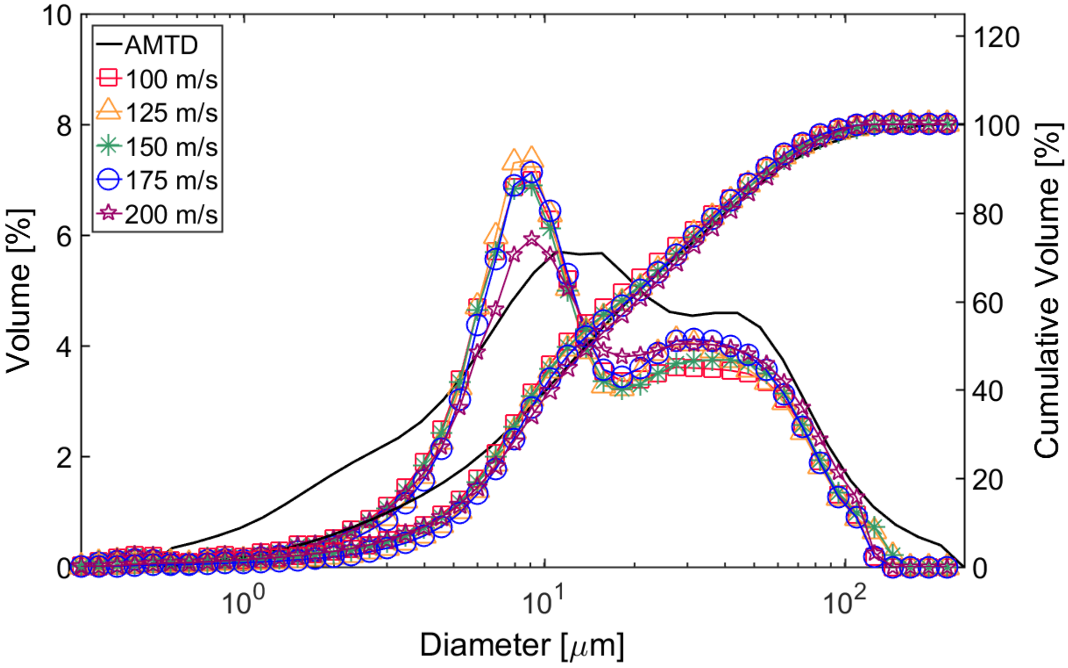

Figure 53. Particle size distribution for DoE3 conditions at centerline and 1.50 g/s for various flow velocities. Cumulative distribution curves that converge to 100% follow the right axis, while non-cumulative plots follow the left axis.

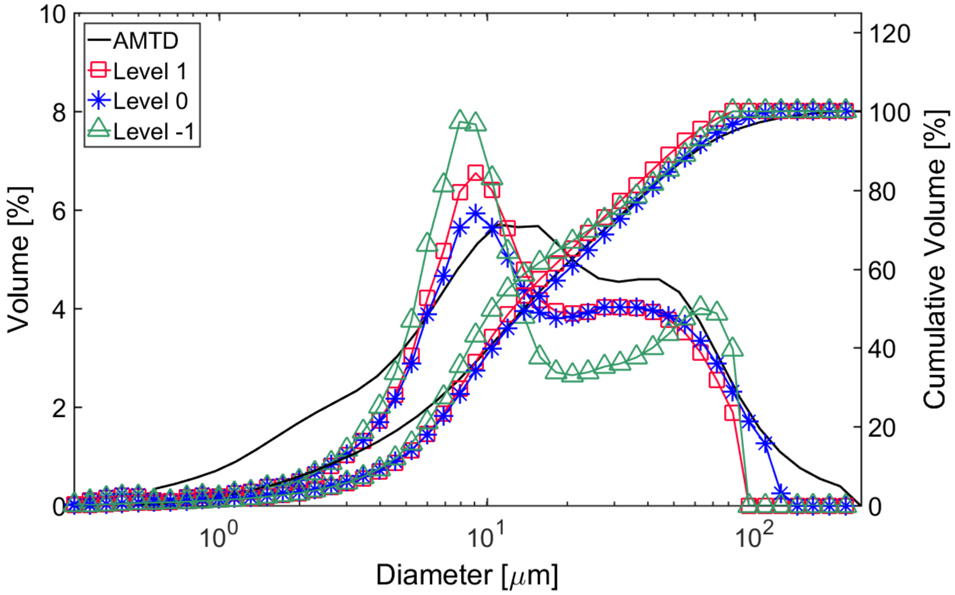

Figure 54. Particle size distribution for DoE2 conditions at 200 m/s and 1.50g/s particle feed rate for various laser beam locations.

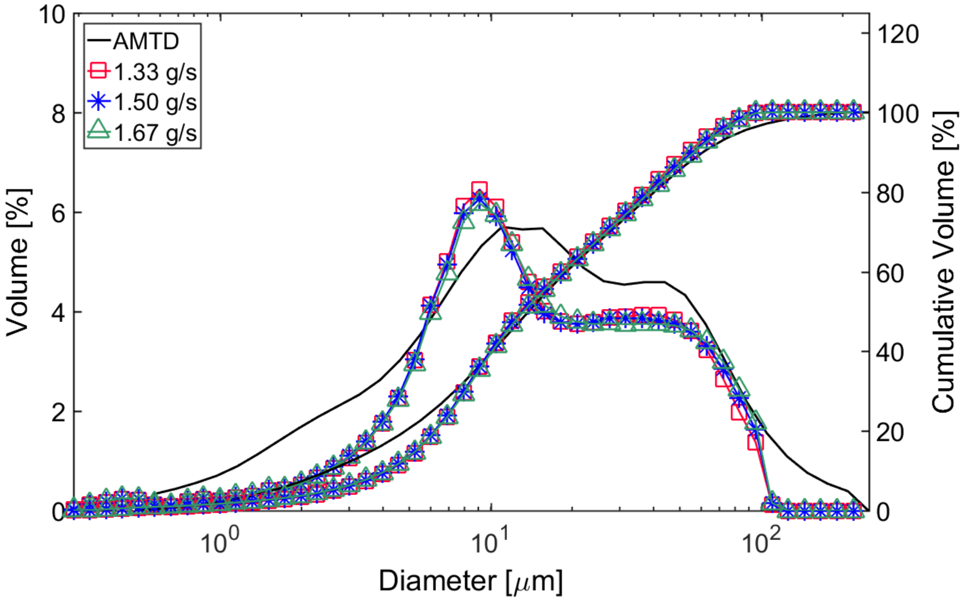

Figure 55. Particle size distribution for DoE2 conditions at 200 m/s and centerline with varying feed rates.

5.4 DoE3 – Response Surface with Sympatec HELOS

The test conditions of DoE3 were modified from those in DoE2, as highlighted in Table 6. To summarize, particle feed rate was reduced, while flow velocities remained constant, meaning experiments were conducted at lower loads. Load ranges were reduced from $\Phi = 10.3 \times 10^{-3}$ – $\Phi = 27 \times 10^{-3}$ to $\Phi = 3.5 \times 10^{-3}$ – $\Phi = 21.9 \times 10^{-3}$. This was done since the transmission levels from reduced loads were deemed sufficient for the Sympatec HELOS to capture reliable laser diffraction data, allowing an investigation of particle behavior at lower loads. It also meant reduced sand usage and experimental costs, as well as producing particle in air concentrations that more closely simulated those in an engine inlet. The higher level of the particle feed rate for DoE3 corresponds to the center point particle feed rate condition in DoE2.

The coefficients for particle size and concentration models are shown in Table 11. It should be noted that the magnitude of particle size parameters discussed are lower than those of DoE2. Since this is seen across all data, including data acquired at exactly the same conditions as in DoE2, it is evident that the laser diffraction algorithms design or theory used to convert laser diffraction patterns on the receiver into the laser diffraction data have an impact on the actual values obtained.

Response	Mean	A	B	C	B^2
Transmission	87.69	4.521	0	-2.935	0
Dv10	1.643	0.041	0.035	0	0.113
Dv50	10.96	0.629	0.344	0	1.009
Dv90			n/a		
D32	4.833	0.156	0.105	0	-0.319
D43			n/a		

Table 11. Response model equation coefficients for DoE3.

5.4.1 Factors Governing Transmission at Lower Loads

The predicted values, based on models generated from experimental data, versus actual values are shown in Figure 56. The main factors for transmission are flow velocity, shown in Figure 57, and feed rate, Figure 58. Both results are as predicted. More laser light transmits from transmitter to receiver with less particles in the sample. Thus, high transmittance is measured with higher velocity and lower particle feed rate. The more unexpected result was the independence of transmission on laser beam location, since this was observed in both DoE1 and DoE2.

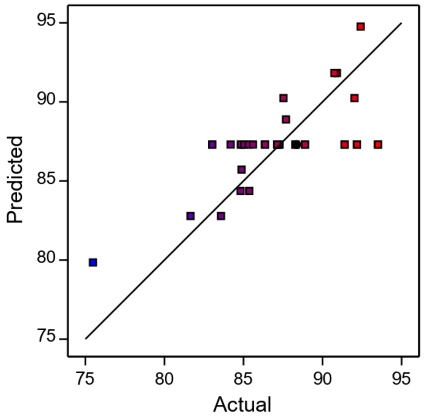

Figure 56. Predicted versus actual transmission model points.

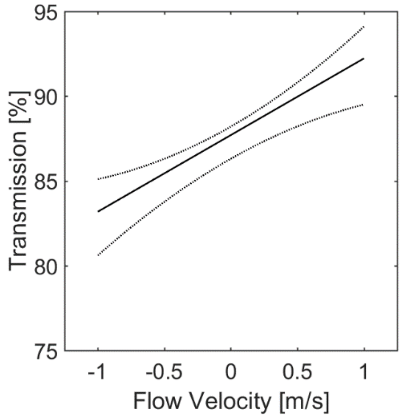

Figure 57. Main effect plot of transmission versus flow velocity.

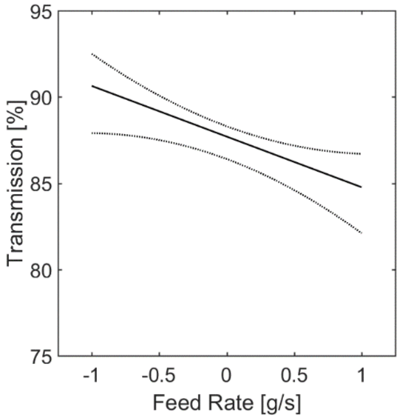

Figure 58 Main effect plot of transmission versus particle feed rate.

5.4.2 Factors Governing Particle Sizes at Lower Loads

In terms of particle distribution data, Dv10 model predicted versus actual is shown in Figure 59, and main effect plots for Dv10 is shown in Figure 60 and Figure 61. Plots for Dv50 and Dv32 show analogous trends and are thus have been placed in the Appendix. Increased flow velocities give rise to a larger particle size measurement, for Dv10, Dv50, and D32. If agglomeration were present in the high-velocity rig, increased flow velocities would break up these clumps, giving rise to smaller particles, but instead, larger particles are seen.

This indicates that the particle dispersion patterns change at higher flow velocities. A greater volume of larger particles is present in the core flow, around r(0), and at higher velocities. As mentioned for DoE1 and DoE2, it is possible that effects of turbophoresis are decreased, thereby inviting a greater volume larger particles, originally trapped in the viscous layer, into the flow. The quadratic spatial dependence in Figure

61 indicates that effects of gravitational forces are not likely. Also, for Dv10, Dv50, and D32, no interaction with laser beam location exists in the models, unlike what was observed in DoE2 and Dv10, respectively. This, together with the transmission plots, reveals that at these conditions, relatively symmetric particle behavior is present at r(+) and r(-). The quadratic nature (as opposed to linear) of the Dv10 versus laser beam location plots in Figure 61 and Figure 94, in the Appendix, also confirm that the particle composition at r(+) and r(-) are similar.

There was no model that could describe the data inputted to develop the Dv90 nor D43 model. Being independent of particle feed rate also indicates that there may be insignificant agglomeration in the high-velocity rig.

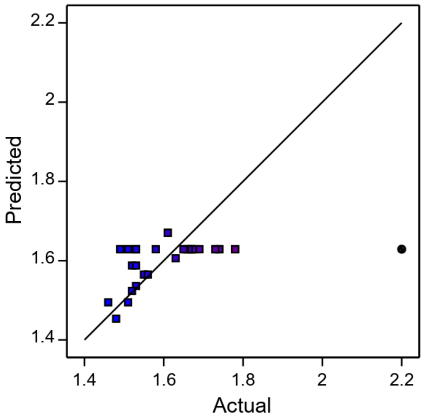

Figure 59. Predicted versus actual Dv10 model points.

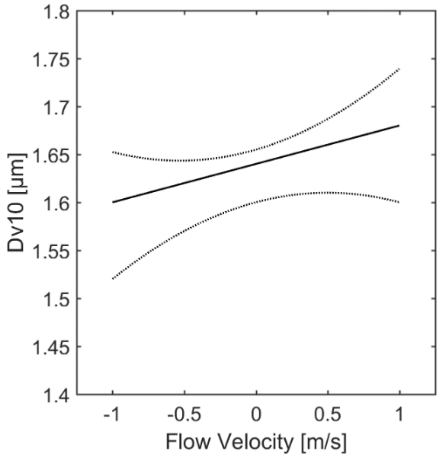

Figure 60. Main effect plot of Dv10 versus flow velocity.

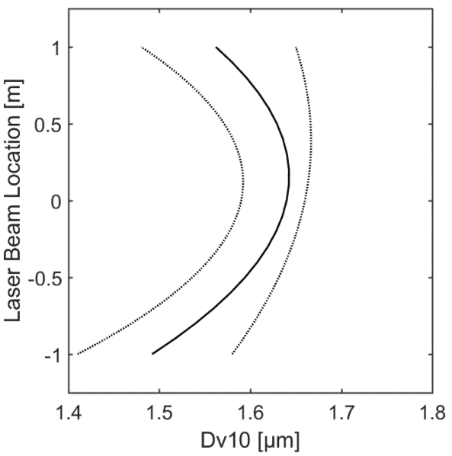

Figure 61. Main effect plot of Dv10 versus laser beam location.

5.4.3 DoE3 Particle Size Distributions

Particle size distributions for DoE3 are shown in Figure 62 – Figure 65. The AMTD distribution in these plots are acquired by the Sympatec HELOS using the particle in air dispersing unit, the Sympatec RODOS. The remaining data are also produced from the Symptec HELOS, but from the rig plume. As revealed in Figure 15, a spike in the volumetric concentration for the Sympatec distribution is present at particle diameter 1.8 µm. The smallest particle size the system lens installed can capture is 1.8 µm, which is likely contributing to the very large initial peak. Otherwise, the remaining distribution peaks are in similar locations to the Microtrac S3500 data.

These plots do not show a peak for large particle sizes, indicating that the particles are not agglomerating. In fact, it is possible that very large particles may be broken down slightly into smaller particles, given that the volume percentage corresponding to the larger particle bin sizes, between 100 µm and 146 µm, for the dispersing unit, is greater than those in produced from the rig plume. An alternative reason for the discrepancies is that the particles used for the dispersing unit were not from the exact same bottle as that for the AccuRate screw feeder. However, it should be noted that the distribution should, in theory, be characteristic of all the sand used in the experiment. Despite these differences, data comparisons from the Sympatec system are very valuable for two reasons. (1) the nominal data, labelled as AMTD, are the distributions of particles, as received from PTI. Curves represented by AMTD should include every particle within the AMTD, because the plume generated by the dispersion unit is of the same width as the laser diffraction laser beam. (2) Measurements are acquired from an identical laser diffraction system with the same lens, optical setup, and model.

The first plot, Figure 62, illustrates the impact of flow velocity on the distribution for particles at the centerline and at 1.5 g/s. These trends were present over all other locations and particle feed rate combinations. The distribution for 100 m/s flow velocity appears, on a volumetric basis, to be closest to the nominal data, followed by 150 m/s, and finally 200 m/s data, where less volume of smaller particles are observed and instead, a greater volume of large particles is captured. This pattern matches observations from the DoE3 model results. This is interesting, given that the particles in the Sympatec RODOS dispersing unit are accelerated to around 100 m/s. As with the Malvern Insitec ST97 cases, the maximum particle size measured does not increase with velocity. This confirms that particles are not observed as “elongated” particles at higher velocities.

Figure 63 shows particle feeding dependence of particle plumes with flow velocities of 200 m/s at the centerline. The plot reveals that the distribution, overall, does not change with particle feed rates. It is promising to see that overall, the inconsistencies of feeding via the mechanical screw design does not influence the distribution of the particles. Next, Figure 64 reveals the distribution at 200 m/s for 1.5 g/s particle feed rate at the centerline for various laser beam locations. The distributions indicate that at the lower region of the rig, the particle size distribution matches that of the disperser more closely, while those at the centerline, r(0) for level 0 and at r(+) for level 1 deviate more. At the lower particle size range, at level -1, r(-), a greater volume of smaller particles is captured. While less of these smaller particles and a great volume of larger particles are present at level 0 and level 1.

Figure 65 has also been plotted to reveal the differences in distributions at the different laser beam locations for particles in flows of 100 m/s. These particle sizes do not deviate as much from one another as those in Figure 64. This may suggest two things: laser diffraction systems and its light scattering theories may have an optical limit, whereby particles cannot travel beyond a certain speed during measurement; also, it suggests that increased air flow velocities segregates particles to a greater extent, where a larger volume of larger particles are captured at the centerline.

Again, all particle size distributions are available. However the complexity of the particle size distribution plots confirm how the models will be useful in determining the particle size distribution parameters for flow velocities, particle feed rates, and measurement locations for commercial probes inserted into the high-velocity particle-laden rig.

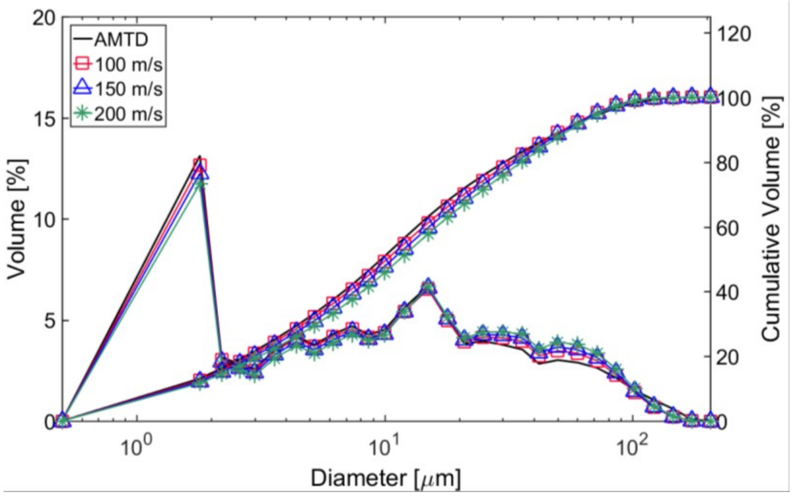

Figure 62. Particle size distribution for DoE3 conditions at centerline and 1.5 g/s for various flow velocities. AMTD corresponds to the distribution for sand particles, as received from PTI, when fed through the Sympatec RODOS dispersion unit.

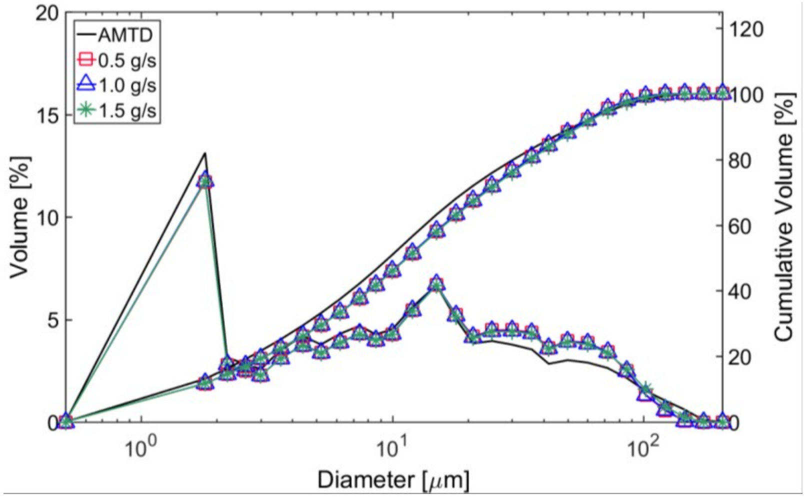

Figure 63. Particle size distribution for DoE3 conditions at 200 m/s and at the centerline for various feed rates.

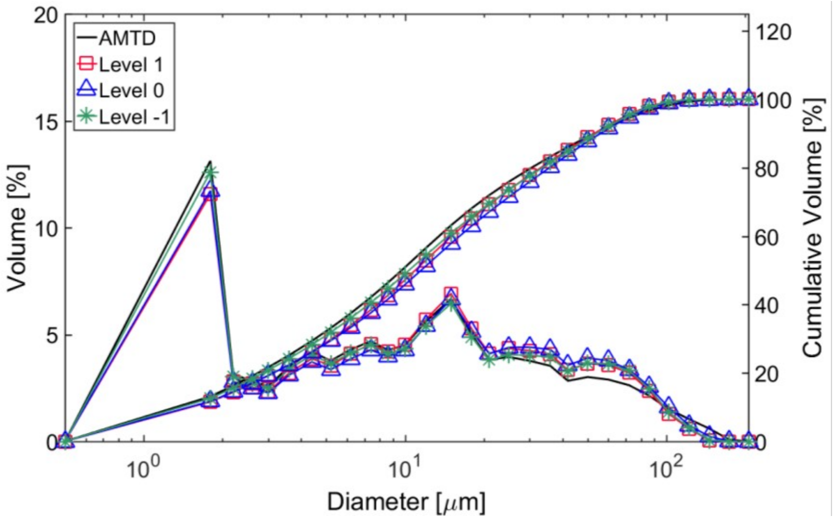

Figure 64. Particle size distribution for DoE3 conditions at 200 m/s and 1.5 g/s for various laser beam locations.

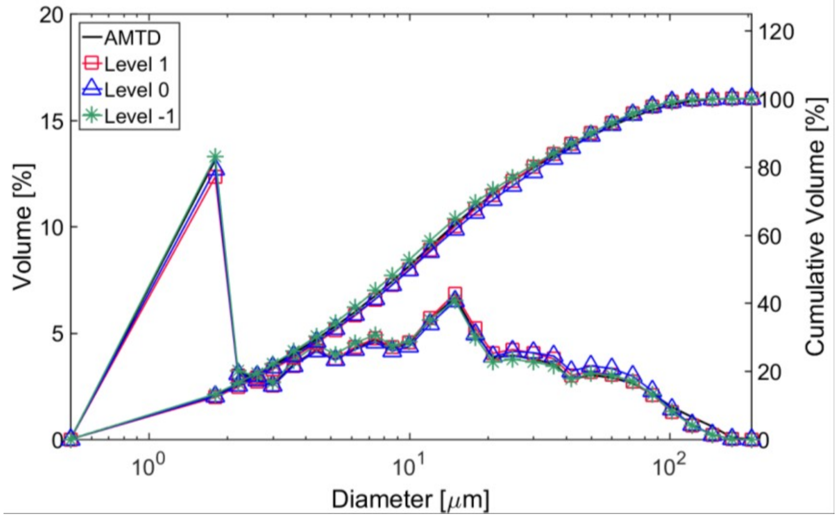

Figure 65. Particle size distribution for DoE3 conditions at 100 m/s and 1.5 g/s for various laser beam locations.

5.4.4 Mie Theory and Fraunhofer Theory Particle Size Distribution Comparisons

In comparing the distributions acquired from the Malvern Insitec ST97 and the Sympatec HELOS, distributions are dissimilar. These differences are likely due to the different theories used for deconvoluting light scattering patterns into particle size distributions. The former system uses Mie theory, which relies on refractive index which is difficult to accurately characterize. While the latter uses Fraunhofer, which does not rely on refractive index information. However, Fraunhofer models are known to be simplified versions of Mie theory models. It is difficult to determine which particle size distribution is more accurate. But it is important to know the limitations of both theories.

Another reason for associating the differences to the model theories adopted, is that the cumulative data from the Malvern and Microtrac system, that both use Mie theory, are very similar for most of the distribution. It should be noted that discrepancies at particle sizes less than 10 μm are likely due to different optical lenses, and ranges of measurable particle sizes.

Despite the differences between the Mie theory and Fraunhofer models, it is promising to see that distributions from the Sympatec RODOS dispersion system and that from the rig are, in general, comparable. Given this, it is evident that conditions within the flow are suitable for evaluation of commercial probes since they would expose probes to all particle sizes present in AMTD.

In regard to particle sphericity, it is likely that turbulence prevents the non-spherical nature of AMTD from affecting laser diffraction measurements. Assuming that the differences between the Malvern and Microtrac data are deemed negligible beyond 10 μm, particles may tumble sufficiently within the rig, so that multiple dimensions of particles are measured. Particles do not align themselves in the direction of the surrounding fluid flow. And laser diffraction systems do not solely measure the longest dimension. Therefore, the non-sphericity of AMTD does not bias the measurements from the Malvern system. Instead, measurements are comprised of multiple dimensions of an ensemble of particles.

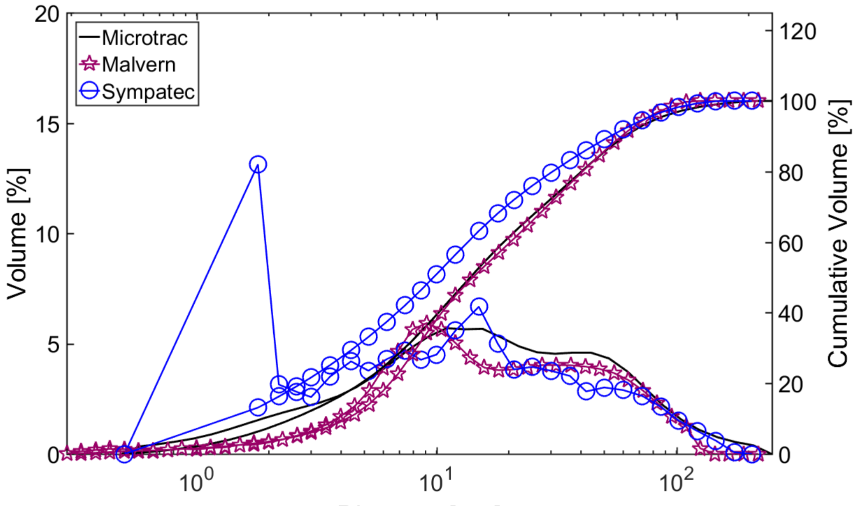

Figure 66. Particle size distribution comparison between three laser diffraction systems: Microtrac with Mie theory, Malvern with Mie theory, and Sympatec using Fraunhofer theory.

5.5 Horizontal Particle Injection

The feed conditions, flow velocities, and laser diffraction system were the same as those in DoE2, to determine whether altering the radial location of particle injection into the high-velocity rig would give rise to similar trends. In general, particle sizes were larger than those in DoE2, indicating that there may have been significantly more agglomeration. The models for sizes are transmission are shown in Table 12.

Response	Mean	A	B	C	AB	A^2	B^2	C^2
Transmission	80.54	6.125	1.54	-1.915	1.415	-1.190	0	2.16
Dv10	7.908	0	0.070	0.262	0	0	0.110	0
Dv50	12.10	0.951	0.386	0	0.27	0	-0.512	0
Dv90	n/a							
D32	13.84	0.425	0.213	0	0	-0.134	-0.381	0
D43	26.12	1.002	0.170	0	0	-0.623	-0.898	0

Table 12. Response model equation coefficients for horizontal particle injection cases.

5.5.1 Factors Governing Transmission

The predicted points based on the model versus actual experimental values for transmission are plotted in Figure 67. Transmission values are dependent on two factors: an interaction factor of flow velocity and laser beam location, and a main factor, particle feed rate. As shown in Table 12, this model has six significant terms. The main factors are flow velocity, laser beam location and particle feed rate. Flow velocity and particle feed rate showed curvature. And flow velocity and laser beam location form an interaction factor. For the main factor uninvolved in an interaction, particle feed rate, the transmission levels decrease with increased particle feed rate, until a certain rate, where transmission levels start to increase again. This is illustrated in Figure 69. This behavior is also seen in DoE2, where the high-velocity rig was subject to the same particle loading. This suggests that the by L = 10D, even though particles were injected horizontally into the rig, they had sufficient time to spatially reorient into a similar manner as that found in DoE2, giving similar transmission curves. It should be noted, however, that even though similar trends were observed, the magnitude of transmission is higher in DoE2 than it is here.

As for the interaction factor shown in Figure 68, an increase in flow velocity affects particle transmission in r(+) more than in r(-). At higher velocities, the magnitude of transmission values is increased by almost 10% for particles in r(-) and by around 15% for those in r(+). Which means that concentrations have been greatly reduced at higher velocities, attributed to the dilution with air, and more dilution occurs at r(-). This is noteworthy, because in DoE1, where in general, lower loads and lower velocities existed, transmission levels also varied to a greater extent at r(+) than in r(-) when flow velocities were increased. In DoE2, transmission was higher in r(+) than in r(-). And for DoE3, transmission values were independent of the location within the rig profile. The interaction plot here indicates that gravity may not be an influencing factor on the particles, given that at lower flow velocities, for which gravity would play a larger role, the transmission levels are similar. Discrepancy in particle concentration at r(+) and r(-) at high velocities is interesting and will be discussed further with Dv50 figures.

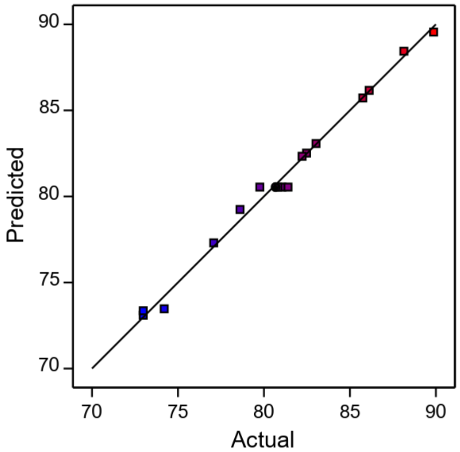

Figure 67. Predicted versus actual transmission model points.

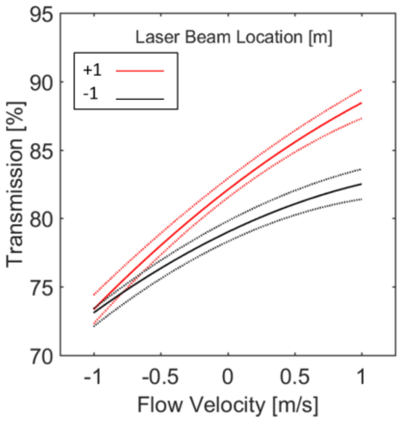

Figure 68. Interaction plot of transmission for combinations of flow velocity and laser beam location.

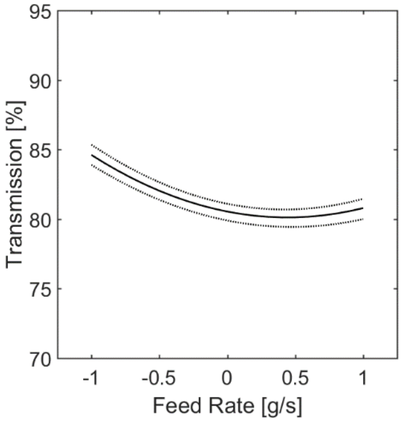

Figure 69. Main effect plot of transmission versus particle feed rate.

5.5.2 Factors Governing Dv10, Dv50, and Dv90

The model predictions versus experimental values for Dv10 and Dv50 are shown in Figure 70 and Figure 71, respectively. The recurring curvature seen in previous plots for particle size distribution parameters versus laser beam location also persisted for the following cases, where particles were injected horizontally towards the high-velocity rig centerline. Figure 72 and Figure 75 show the curvature. Despite the small change ranging from around 7.7 μm to 7.95 μm. in Dv10 values, curvature was still detected, and is the most significant factor in the model. The values for Dv50 ranged between 11 μm to 12.2 μm. Asymmetry also exists, in a similar fashion to the asymmetry seen in previous plots versus laser beam location, as well as the velocity profile in Figure 20.

Dv10 is also a function of particle feed rate, where the value increases slightly with increased particle feed rate. This may be an indication of agglomeration, where increased loading causes particles to stick and clump with one another, giving rise to greater Dv10 values.

The remaining plot for Dv50 involves its most significant factor: flow velocity, which is part of an interaction factor with laser beam location. The interaction plot of Dv50 is shown in Figure 74. This plot shows that at lower velocities, Dv50 values at r(+) are about 0.5 μm greater than those at r(-). And this divide gets more prominent with increasing flow velocities. At r(+), Dv50 values are predicted to be just over 13 μm, while at r(-), just under 12 μm. In comparing this plot to the transmission plot in Figure 68, at high velocity conditions, a small volume of large particles may exist at r(+), while many smaller particles reside in r(-). This is interesting because it would be expected that larger particles are subject to gravitational effects, drawing them to r(-).

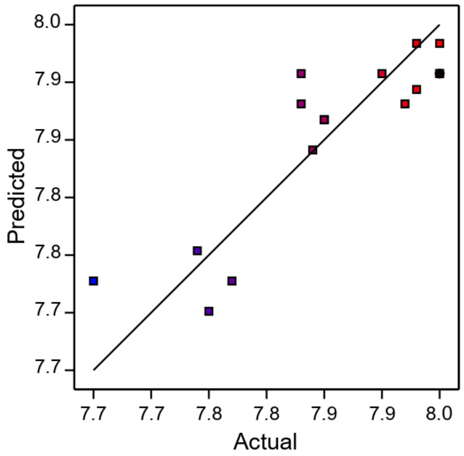

Figure 70. Predicted versus actual Dv10 model points.

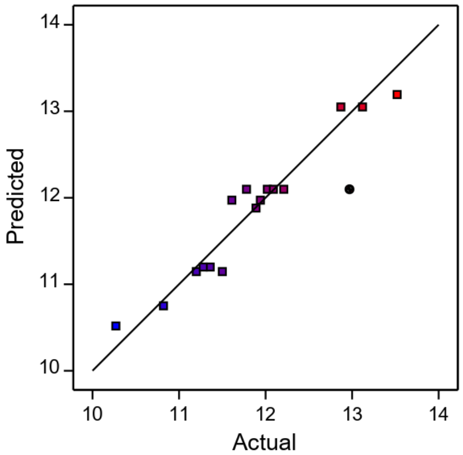

Figure 71. Predicted versus actual Dv50 model points.

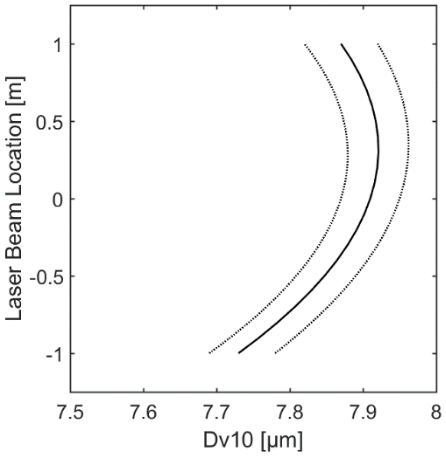

Figure 72. Main effect plot of Dv10 versus laser beam location.

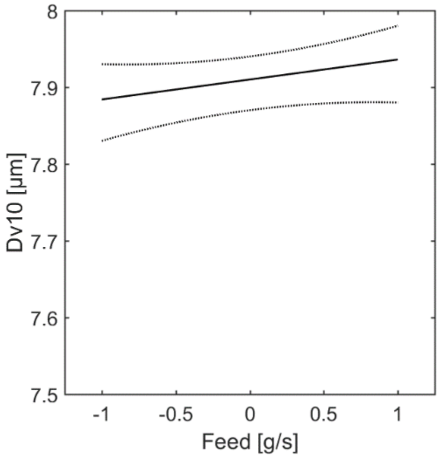

Figure 73. Main effect plot of Dv10 versus laser beam location.

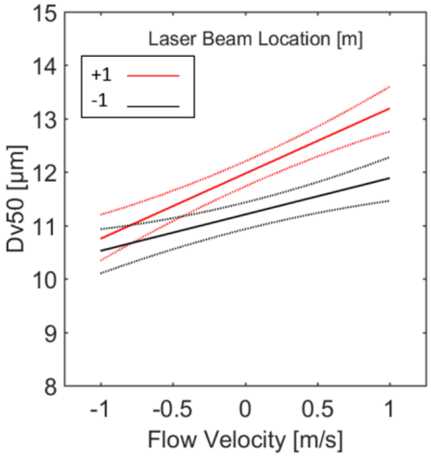

Figure 74. Interaction plot of Dv50 for combinations of flow velocity and laser beam location.

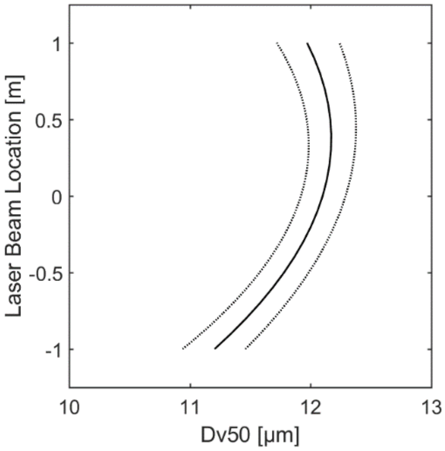

Figure 75. Main effect plot of Dv50 versus laser beam location.

For Dv90, its significant factor is flow velocity. The model predicted versus actual is plotted in Figure 76, and the relationship between Dv90 and flow velocity is plotted in Figure 77. Again, particle size distribution parameters are proportional to flow velocities. The plot includes some curvature, which is not significant, but was kept in the model, to ensure better ANOVA diagnostic results. According to the plot, 90% of the volume particles are 59.5 µm or less at low velocities, and 63 µm or less at higher velocities. This relationship indicates that despite injection occurring into the side of the high-velocity rig, particles still continue to interact in such a way that causes a greater volume of larger particles to be present in the measurement volume at elevated velocities.

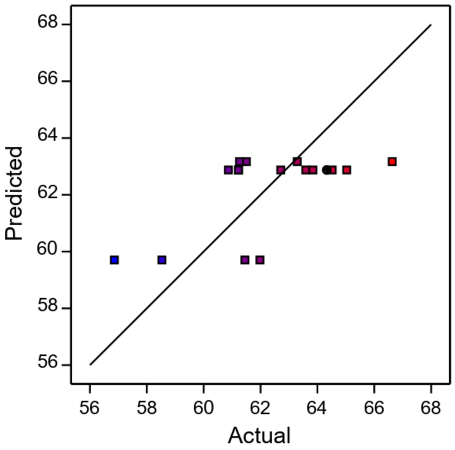

Figure 76. Predicted versus actual Dv90 model points.

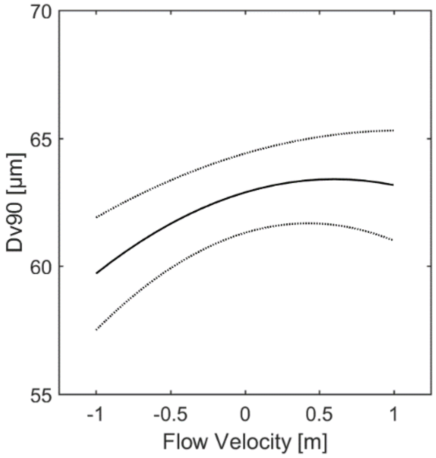

Figure 77. Main effect plot of Dv90 versus flow velocity.

5.5.3 Factors Governing D32 and D43

The model versus predicted plots for D32 and D43 are shown in Figure 78 and Figure 79, respectively. Main effects of D32 are shown in Figure 80 and Figure 81, while those of D43 are shown in Figure 82 and Figure 83. Despite using horizontal particle injection, these plots show the same trends for diameter versus flow velocity, as seen in Dv50 in DoE2, where the same particle loads were present.

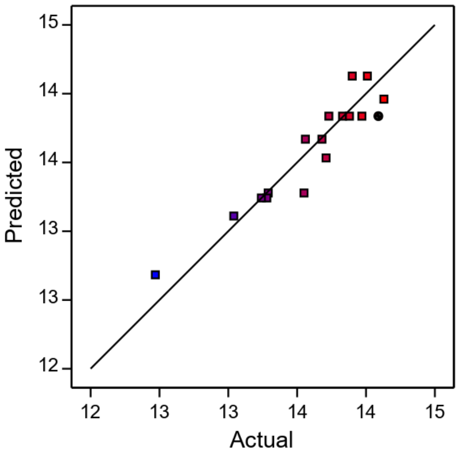

Figure 78. Predicted versus actual D32 model points.

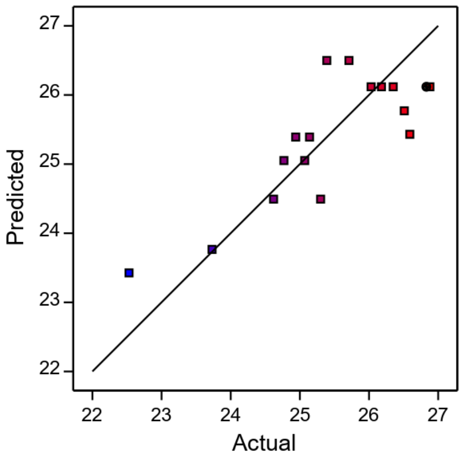

Figure 79. Predicted versus actual D43 model points.

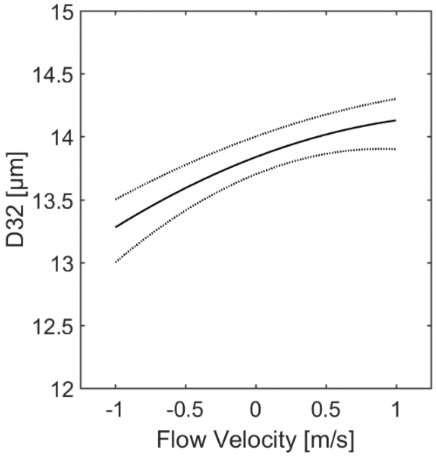

Figure 80. Main effect plot of D32 versus flow velocity.

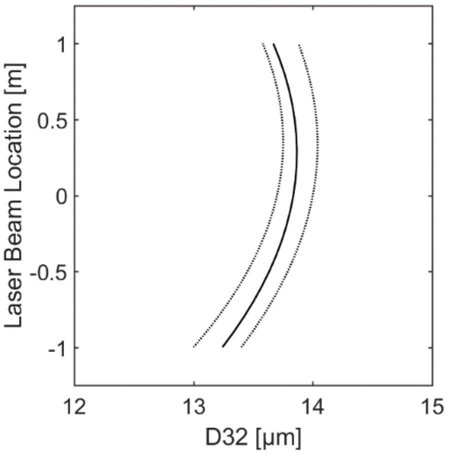

Figure 81. Main effect plot of D32 versus laser beam location.

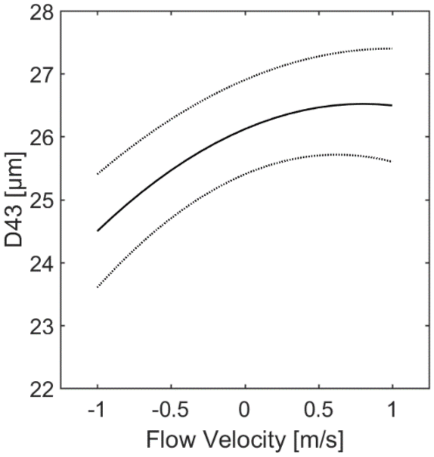

Figure 82. Main effect plot of D43 versus flow velocity.

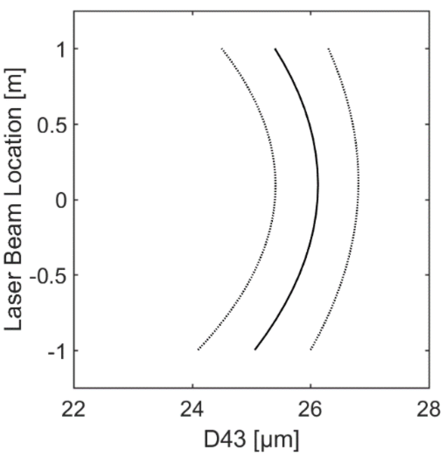

Figure 83. Main effect plot of D43 versus laser beam location.

5.6 Particle Size Distributions for Horizontal Particle Injection

Figure 84 – Figure 86 show the particle size distributions acquired when particles are injected horizontally, as opposed to vertically, in DoE1, DoE2, and DoE3. Across all plots, it is evident that particle agglomeration appears to be present, where the smallest particle size is even larger, at around 5 µm. Also, in comparing to vertical particle injection, the distributions are different, showing three peaks, and with a very large first peak, almost four times the volume % as that of vertical injection.

For Figure 84 , it is interesting to see that the 200 m/s case is different from the lower velocity cases at particle sizes around 10 µm. In terms of particle size data, an increase in velocities gives an increase in particle size. While Figure 85 shows that particle size distribution for the centerline case appears to differ from those closer to the edge, at around 10 µm. This is evident in the particle median size data. At level 1, 0 and

-1, the Dv50 values are 12.23 μm, 12.87 μm, and 11.80 μm respectively. Showing that the particle sizes are larger in the centerline, as with the particle size data. It is noted that distributions are not truncated for the larger particle sizes for levels 1 and -1, as was seen in the DoE2 results. Figure 86 shows that particle sizes do not alter with varied particle feed rates, consistent with DoE2 and DoE3 surface responses. The same is true for the particle size data parameters.

These observations match the trends shown in DoE2 and DoE3. This is interesting and confirms that particle segregation occurs no matter the initial point of injection of particles. The air surrounding the flows appears to organize particles in the manners shown in the models, where a greater volume of larger particles is situated in the middle, and smaller particles towards the edge. Despite the similarity in trends, it is evident that the particles are subject to more agglomeration, which is undesirable for assessing particle sizing capabilities for commercial probes, especially for the lower particle size range. This investigation, therefore, shows that vertical particle injection is favorable for this work.

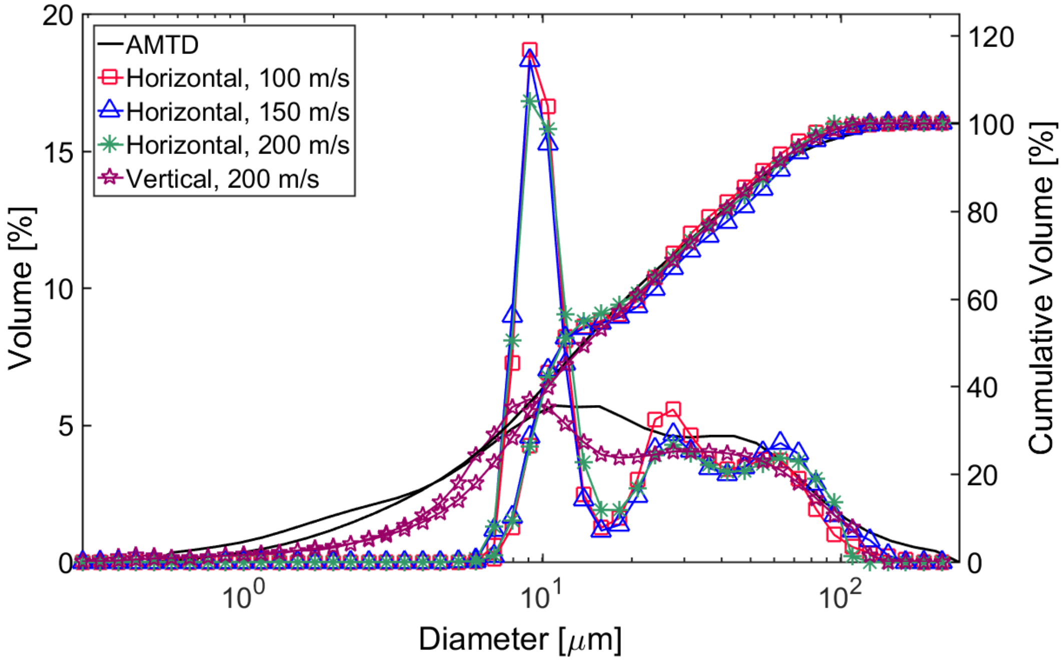

Figure 84. Particle size distribution for horizontal particle injection at the centerline for 1.50 g/s for various flow velocities.

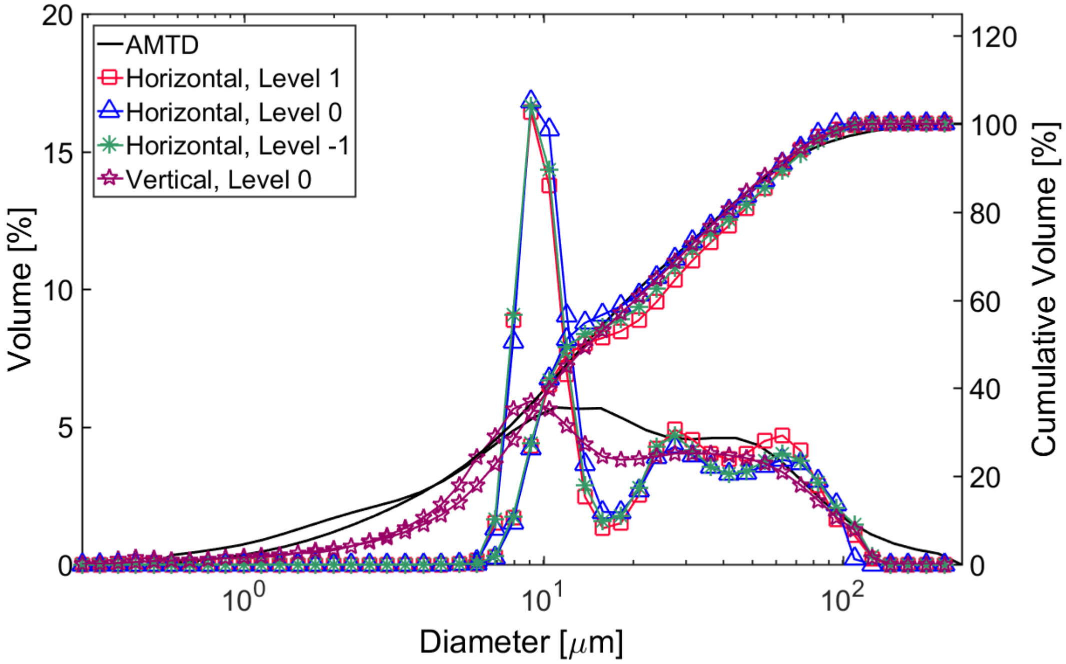

Figure 85. Particle size distribution for horizontal particle injection at 200 m/s for 1.50 g/s for various laser beam location.

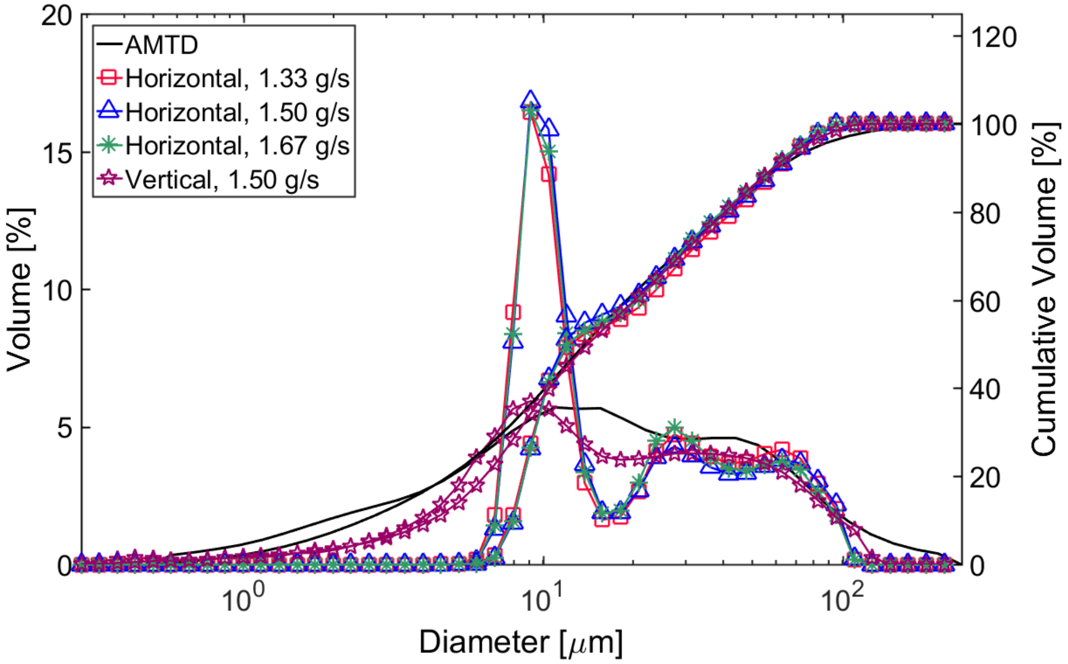

Figure 86. Particle size distribution for horizontal particle injection at 200 m/s and the centerline at various particle feed rates.

5.7 Reduced Rig Diameter

The particle size distributions for the reduced rig diameter cases are shown in Figure 87 and Figure 88. Transmission trends are similar to those in DoE2. Interestingly, even with a smaller pipe diameter, $D_2 = 0.75D_1$, the particle sizes for Dv10, Dv50, Dv90 exhibited the same patterns as that seen in the models for the DoE2 and DoE3 rig diameters. Even though it appears that at level -1, the peak is smallest at around 10 μm, level 1, 0, and -1 particle medians are 13.66 μm, 14.05 μm, and 13.24 μm, respectively. When comparing the distributions to the cases for $D = D_1$, the smallest particles captured differ. The smallest particle size observed is around 1.8 μm in D_2 cases but is around 0.28 μm for that in D_1. This also is an indication of particle agglomeration with reduced rig diameters. In addition, an additional peak for D_2 cases is present, giving a trimodal distribution.

While for Figure 88, it is evident that the same discrepancies exist between D_1 and D_2 cases. Again, increased velocities cause particle sizes to increase. For Dv50 values corresponding to these conditions, at 200 m/s, 220 m/s, and 240 m/s, the sizes are 13.23 μm, 14.05 μm and 14.59 μm. However, the distribution does not exhibit the same drastic change in PSD, as was seen in the DoE2 cases. It is likely that given that these flow velocities are beyond 200 m/s, high velocity effects have been applied to all cases.

These findings reveal that although using a reduced diameter may appear to be a solution to less particle segregation, exposing commercial probes to particles that are representative of AMTD particle sizes, this is not the case. Small clumps of agglomeration seem to be present in the reduced diameter, so the smallest particles that the probe could be evaluated for would be around 1.8 μm, instead of 0.28 μm. It should be noted, also, that since particle segregation continues to be present for the reduced diameter case, segregation may occur, regardless of the pipe diameter. Therefore, a commercial probe with a very small probe volume, on the order of 1 mm^2, may never be able to obtain a distribution that is exactly the same as that measured by PTI, in a rig setting, unless the diameter of the rig pipe is the same or less than the commercial sensor probe volume. This would not be feasible. The models represented in this work can therefore be used to determine the particle size parameters, at various conditions, due to particle segregation.

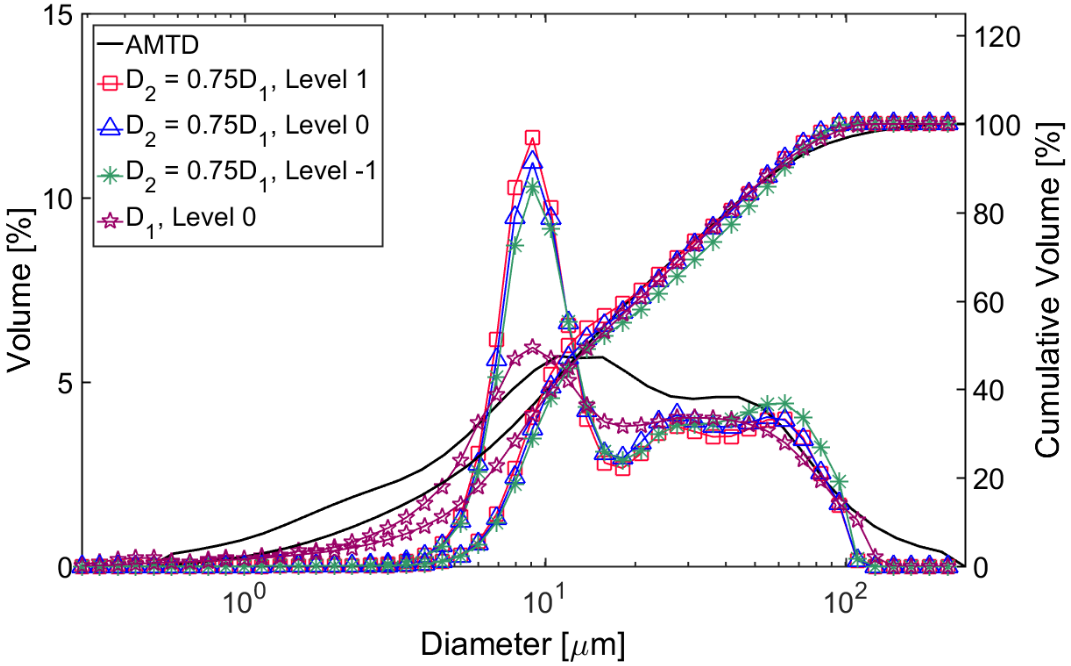

Figure 87. Particle size distribution for reduced rig conditions at 220 m/s for 1.33 g/s for various laser beam locations.

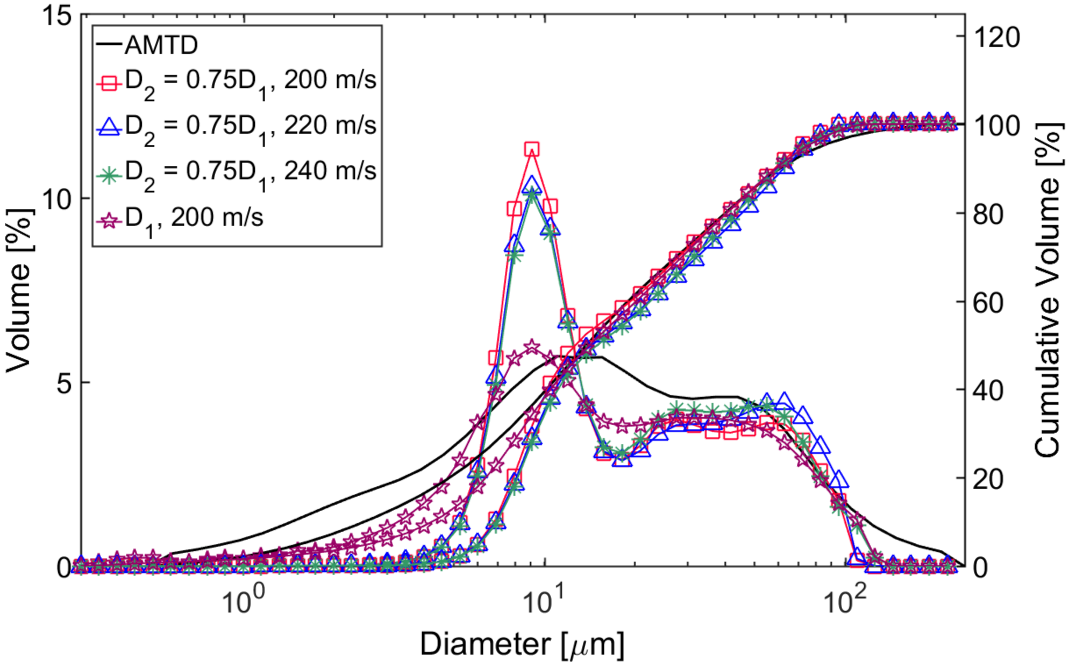

Figure 88. Particle size distribution for reduced rig conditions at the centerline for 1 g/s for various flow velocities.

5.8 Imaging Rig Exit Profile

Images of the rig profile exit illuminated with a laser sheet have been shown in Figure 89. The images were taken at various conditions. Given that the particle screw feeder design causes inconsistent particle feed rates, the quantitative pixel density for these different conditions cannot provide any physical meaning. However, when viewed qualitatively, the images reveal the non-homogeneity of the particle dispersion, identified in the preceding sections.

The regions of highest pixel intensity are a measure of light captured by the camera sensor. Thus, they indicate a greater concentration of particles, either by particle surface area or number. However, it is not possible to distinguish the sizes of the particles in concentrated regions in these images. A greater concentration is exhibited at the core of the plume, and this decreases towards the plume edge. Some of the images reveal non-homogenous particle segregation, since greater particle concentrations are visible at the top region of the images, also evident in the transmission model results.

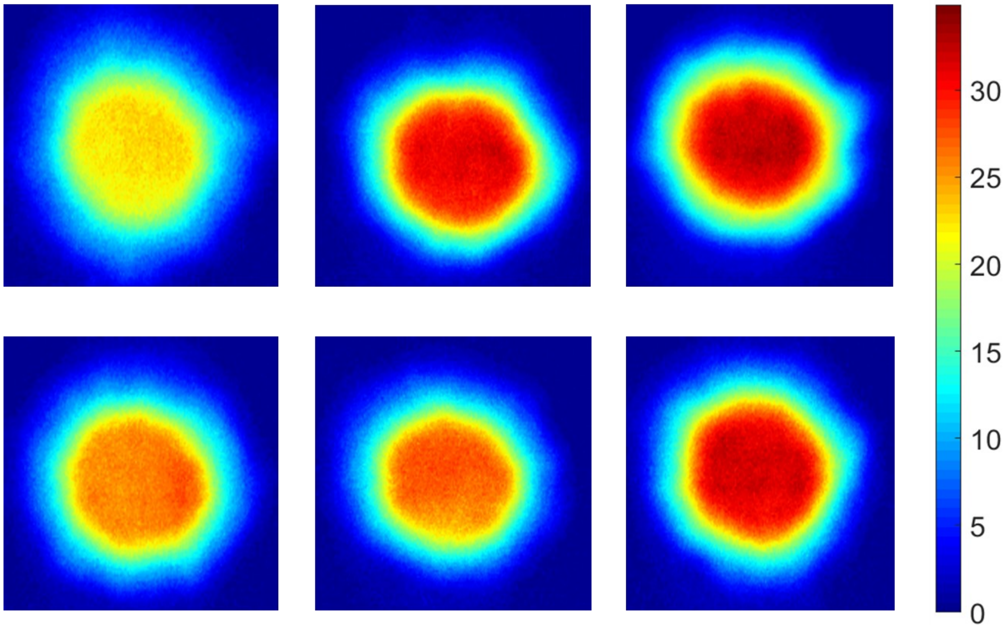

Figure 89. Contour plots of rig exit plume at various testing conditions.

5.9 Evaluation of Forces Acting on Particle in Air Stream

Using equation (10) and equation (13), the $F_{h/v}$ value was determined for particles of various sizes, sphericity, and in various fluid flow velocities. Drag coefficient curves for non-spherical particles were used to obtain drag coefficients, C_d, for corresponding particle Reynolds numbers. Coefficients for various particles sizes, sphericities, and flow velocities are plotted in Figure 90. The drag force is proportional to C_d but is inversely proportional to particle diameter, d_p. Thus, with all other parameters equal, the overall value of the drag force is dependent on the ratio of C_d/d_p. Particles with reduced size and sphericity and flow velocities generally have greater C_d. This is true except for particles of 200 μm for sphericities of $\psi = 0.125$, for which drag coefficients increase with velocities. The cause of this outlier is the particles Reynolds number, which is greater for these sizes

(>880). Beyond this regime, C_d values continue to increase for greater Reynolds numbers. It is likely that most particles for AMTD have a sphericity of at most ψ = 0.6. However, particles with perfect sphericity are plotted here to provide intuition on how greater sphericity alters the $F_{h/v}$.

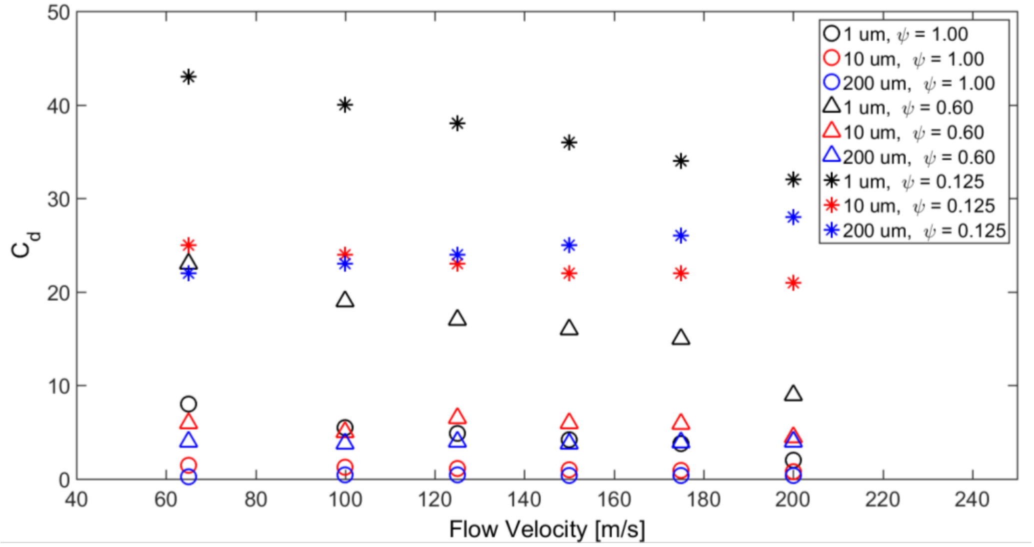

Figure 90. Drag coefficients for various particle sizes, sphericities, and flow velocities.

For DoE1, with flow velocities of 65 m/s and 125 m/s, 1 μm sized particles ψ = 0.125 are subject to the greatest drag coefficient. Assuming no other forces are present, Figure 91 shows that $F_{h/v}$ are around 3.3 and 10.8 for the two velocities. Particles are likely to travel a vertical distance of 1D from the injection point to the rig floor and a corresponding axial distance of 3.3D and 10.8D. While for 1 μm sized particles of less sphericity, ψ = 0.6, at 65 m/s and 125 m/s, particles are subject to less drag and the $F_{h/v}$ axial distances travelled for 1D vertical drop is around 1.7D – 4.8D. These values shows that for 1 μm sized particles to be measured by the laser diffraction system at an axial distance of around 36D from the particle injection point, these particles must be subject to other forces present in the particle-laden flow that lift them up by the time the particles reach the laser diffraction measurement zone.

For 10 μm sized particles, the $F_{h/v}$ values are even greater. 10 μm is of interest, as it is close to the particle median size. For $\psi = 0.6$ and at 65 m/s to 125 m/s, for vertical displacement of 1D, 10 μm particles travel an axial distance of 3.2D to 12.8D, while for sphericities of $\psi = 0.125$, from 13.3D to 45.4D. Despite these particles having lower C_d than the 1 μm particles, the inverse of the d_p term dominates, causing drag forces to be greater. Therefore, they travel further axial distances. For the case of particles at 125 m/s and with $\psi = 0.125$, particles are subject to very large drag forces, and it is even possible that the particles do not touch the bottom of the 36D long rig.

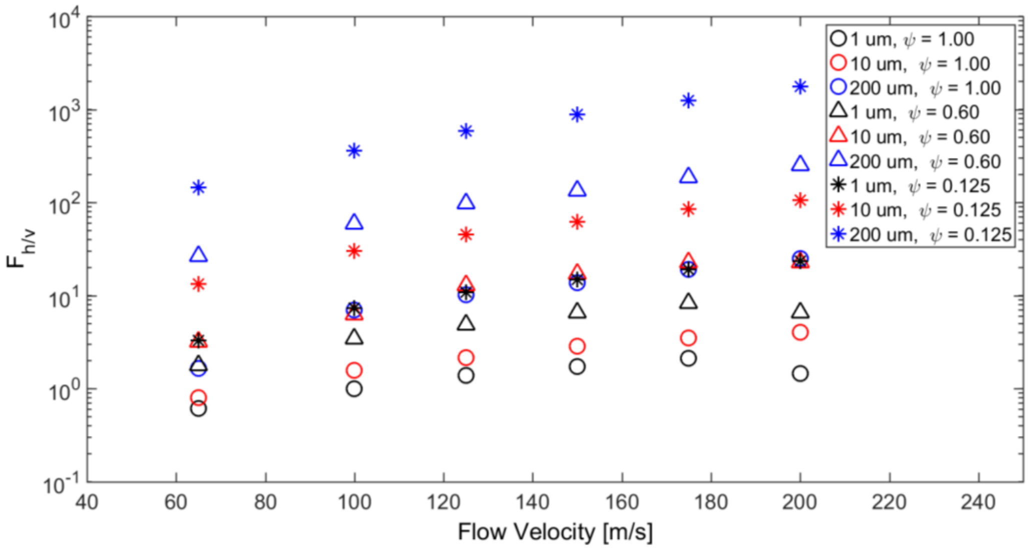

Figure 91. Ratio of horizontal versus vertical force components for various particle sizes, sphercities, and flow velocities.

As for particles of greatest size within the distribution, 200 μm, for a vertical drop of 1D, particles with flow velocities of 65 m/s and 125 m/s, and sphericities of $\psi = 0.6$ travel an axial distance of 26.4D to 97.7D and particles with $\psi = 0.125$, travel an axial distance of 145D to 733D. From this, it is evident that despite the drag coefficients being low, the particle size causes drag forces and thus $F_{h/v}$ values to be large. This means that the particles are unlikely to touch the rig floor at all. The drag forces dominate the gravitational forces in these cases. It is important to note that the reduced sphericity and flow velocity significantly increase the $F_{h/v}$.

As for DoE2 and DoE3, with flow velocities ranging from 100 m/s to 200 m/s, 1 μm sized particles are again subject to greatest C_d. For 1 μm sized particles with sphericity of $\psi = 0.6$, at 100 m/s and 200 m/s, the $F_{h/v}$ is around 3.5 and 6.6, respectively. Meaning, for a 1D drop from the injection point, particles reach the rig floor after travelling an axial distance of around 3.5D – 6.6D. For reduced sphericity, these axial distances are increased to 7.3D and 23.4D.

For the median particle size, 10 μm, particles travel 6.3D to 22.7D and 30.3D to 106.1D for $\psi = 0.6$ and $\psi = 0.125$, respectively. Thus, other than particles with $\psi = 0.125$ travelling at 200 m/s, the particles are likely to reach the bottom of the rig at least once before re-orienting in the measurement zone.

Finally, for the largest particle group, $F_{h/v}$ values are very high, ranging from 59.4 to 250.2 and 360 to 1752 for for $\psi = 0.6$ and $\psi = 0.125$ respectively. Again, assuming all other forces are negligible, and particles strictly travel in the axial direction, particles will not touch the bottom of the rig before reaching the measurement zone.

It is interesting to observe such large $F_{h/v}$ values, even though drag forces are comparatively low, and particle size is large. The this is attributed to the increase in relative velocity term. Compared to other particle sizes, 200 μm particles travel with speeds that deviate most from the surrounding fluid, only reaching about 90% of the fluid speed.

It is evident that some particles touch the rig floor before reaching the laser diffraction measurement zone, especially for particles with low $F_{h/v}$. It is likely that particles get lifted before reaching the measurement zone, otherwise they would not have been measured by the laser diffraction systems. Therefore, there must be other forces present, causing heterogeneous particle dispersion. Small particles may be subject to Saffman lift, which is a force that acts on small particles in shear flow. Particles with lower sphericity get lifted more since edges aid the rotation, and the lift force is dependent on such rotation. The force acts perpendicularly to the direction of the fluid flow. These lift forces likely act in the radial direction towards the rig wall, thereby causing small particles to be able to disperse within the flow. Assuming this small particle is at the centerline, a force would act from the centerline towards the wall when the horizontal velocity vector of the fluid between the particle and the wall is greater than the horizontal force of the particle itself. Larger particles, on the other hand are less common towards the rig walls. It is likely that with larger St, and thus greater momentum, that they are less likely to follow the turbulence of the flow and will continue existing within the core region.

In regard to the non-uniform distributions of particles at different sizes, trends observed are similar to those acquired by Soo and Regalbuto [50]. In their work, they show how monodisperse 230 μm and 115 μm particles undergo non-uniform particle dispersion across the cross-section of a pipe. They conclude that these monodisperse particles, are subject to small gravity effects, and will segregate, creating a concentration profile of solid particles in steady fully developed turbulence that approximates the turbulent velocity profile, when injected into fully turbulent pipe flow. These profiles reveal that particle concentrations are greater in the core region, and this concentration decreases towards the pipe wall edge. This is similar to the trends observed in DoE2 and DoE3, where larger particles are more concentrated in the core.

Soo and Regalbuto give an explanation for such non-uniformity, declaring that the presence of a net momentum of turbulent transport from the wall region towards the core region exists in single-phase flow. Thus, when particles are introduced, solid particles travelling from the center towards the wall are decelerated to velocities that match that of the stream velocity. Therefore, the average velocity of particles in the wall region is greater than that of the average stream velocity. Given that the average concentration of particles per unit volume should be constant, the number of particles in a local region can be found by:

$$C_l = C_{ave}\frac{u_f}{u_p} \tag{16}$$

Thus, for a constant C_l, particles of greater u_p will give rise to a decrease in C_{ave}. This gives rise to faster relative particles towards the wall, and thus lower concentration at the wall.

Soo and Regalbuto [50] also discuss how the particles travelling towards the wall center encounter opposing effects. Particles which have been decelerated already (from interactions with the wall) are then accelerated to match velocities in the core region. Therefore, the average particle velocity near the centerline is lower than that of the fluid. This increases the local concentration, C_l.

Another finding of the study by Soo and Regalbuto was that this trend of increased particle concentration near the centerline was apparent, regardless of the particle size studied. This does not match behaviors observed in the current work. If particles of different sizes produced the same pattern of concentration profiles, the ensemble measurements would be the same or at least similar across the profile. A cause for the opposing results may be the particle sizes investigated. While their study was conducted at high flow Reynolds numbers akin to those in this work, particle Reynolds numbers were much higher, since particles of 115 μm and 230 μm were used. In this study, particle Reynolds number is much smaller given that the particles studied are less than 200 μm in diameter and AMTD has particle distribution median of around 10 μm.

To provide insight on why large particles act differently from smaller particles in this work, another parameter, Stokes number, (St), which is the ratio between the particle time scale and the characteristic flow time scale, is useful to evaluate. Particles with St < 1 have small inertial and are therefore more likely to follow any variation in the carrier flow. Conventional St is only valid for particles in the Stokes regime, where particle Reynolds number is Re < 1. Therefore, for this work, where Re_p ranges from 4.4 to 2700, theoretically, equations used determine conventional St are not valid. A non-Stokesian drag correction factor, ψ_e , can be added in these cases, developed by Israel and Rosner [51]. It should be noted that despite the equation being valid for spherical particles, the non-dimensional number is still of interest. The correction factor is found by:

$$\psi_e\left(\mathrm{Re_p}\right) = \frac{3\left(\sqrt{c}\,\mathrm{Re_p}^{\frac{1}{3}} - \arctan\left(\sqrt{c}\,\mathrm{Re_p}^{\frac{1}{3}}\right)\right)}{c^{3/2}\mathrm{Re_p}} \tag{17}$$

Where c = 0.158

$$\mathrm{St_e} = \mathrm{St} \cdot \psi\left(\mathrm{Re_p}\right) \tag{18}$$

Conventional St would have given increasing St for increased particle size, without taking into account the increased drag force from the increased particle size, thus overestimating how these particles depart from the fluid flow. St_e shows that for particles in this flow, taking the same particle sizes studied for the drag forces: 1 μm, 10 μm, and 200 μm, travelling between 65 m/s and 200 m/s, 1 μm particles have St_e between 0.35 < 0.1 and 1.08, 10 μm St_e are between 35 and 108, and for 200 μm particles, St_e is between 14,000 and 43,300. These values show that only the particles that are 1 μm at 65 m/s will follow the flow closely, while those at 200 m/s will to some extent. The other particle sizes will depart from the flow.

From these Stokes values, it is evident that the low St_e of the smaller particles (with smaller inertia) follow the turbulent flow and any complex structures such as turbulent eddies. This may be why smaller particles segregate towards the wall and are more affected by turbophoresis, which is a force induced by nonhomogeneous turbulence in the flow, and acts towards the directions where turbulence levels are lower, i.e. towards the wall [49]. It is also possible that these small particles are more evenly dispersed within the rig than the larger particles, because of strong inertial effects, as discussed by Salehi et al. [52].

Based on this, the curvature of particle sizes observed in the DoEs can be explained by superimposing two phenomena: (1) larger particle concentrations are generally higher in the centerline, and (2), smaller particles are more evenly dispersed within the rig exit profile.

6

SUMMARY, CONCLUSIONS, RECOMMENDATIONS

6.1 Summary

- A particle-laden rig with high-velocity, non-spherical reference particles, Arizona Medium Test Dust (AMTD), was developed to aid the development of commercial particle ingestion monitoring probes.
- Single phase flows were characterized to confirm that rig conditions match that of flows velocities in that of an engine inlet, 200 m/s or Mach number 0.58.
- Several experimental studies were performed on the two-phase flow at the exit of the rig to (1) determine whether laser diffraction measurements could capture all sizes that exist in the particle size distribution for AMTD and, (2) characterize particle distributions as a function of flow velocity, particle feed rate, and measurement location.
- To conduct studies systematically and develop models for particle size and concentration at various rig conditions, classical Design of Experiments (DoE) was performed. Response surfaces were developed to model particle size and concentration as functions of flow velocity, particle feed rates, and measurement location. Data were acquired by two laser diffraction systems. One system using Mie theory, a Malvern Insitec ST97 and another using Fraunhofer theory, a Sympatec

HELOS. For Malvern Insitec ST97 measurements, distributions were compared to measurements acquired by PTI from a Microtrac S3500, also using Mie theory, but accounting for particle sphericity. Sympatec HELOS measurements were compared to those acquired using the Sympatec RODOS dispersion unit.

- The surface response models for Dv10, Dv50, Dv90, D32, D43, and transmission are valid for particle loading between 0.5 g/s to 1.67 g/s and velocities from 100 m/s to 200 m/s, in a round pipe flow of 26.7 mm inner diameter. Given that one parameter alone cannot be used to describe a distribution, the DoE models serve as an ample method for quantifying size parameters that describe the distribution. Otherwise, exact particle size distributions for the conditions measured are also available.
- Models indicated the presence of non-homogeneity in the particle in air plume. This was investigated further for flow from a reduced pipe diameter of 21.1 mm, with velocities between 200 m/s – 240 m/s and particle loadings of 1 g/s. Additionally, particle sizes were acquired for plumes created via horizontal particle injection, as opposed to vertical injection, between 100 m/s – 200 m/s and particle loadings between 1.33 g/s and 1.67 g/s.
- Further investigations of forces acting on individual particles allowed for a better understanding of non-homogenous particle dispersion within the flow profile.

6.2 Conclusions

- **The rig developed in this study produces repeatable two-phase flows simulating particle-laden engine inlet conditions.**

The experimental test rig successfully produces repeatable flows simulating particle-laden engine inlets with fluid velocities between 100 m/s – 200 m/s and Reynolds numbers of 1.74×10^5 – 3.48×10^5, for polydisperse reference particles of 0.25 μm – 178 μm and particle Reynolds numbers of 4.4 – 2700. Particles are injected into flows at 0.5 g/s – 1.67 g/s, equivalent to loadings of $\Phi = 3.5 \times 10^{-3}$ – $\Phi = 27 \times 10^{-3}$.

- **Statistically significant Design of Experiments (DoE) models are developed and can be used to estimate local particle size and concentration levels of reference particles, Arizona Medium Test Dust (AMTD), in the rig.**

DoE models developed are valid for 95% confidence intervals. These models confirm that local particle size distributions within the rig are dependent on flow velocity and laser beam location. Findings of the high-velocity particle-laden pipe flow include: (1) particle size distribution parameters, Dv10, Dv50, Dv90, D32, and D43 increase with increased flow conditions, (2) a greater concentration of larger particles exists in the core region of the flow, while smaller particles tend to disperse well within the profile, and (3) greater particle concentration exists at the top portion of the rig, and reduced concentration at the bottom portion. DoE models can be used to determine the local particle size distribution within the rig, so that sensors with small probe volumes can be appropriately positioned within the rig for validating sizing performance. The models can also predict the maximum variation of particle sizes across the rig profile, as well as estimate the expected deviation of particle sizes from the sand, as received, from the sand manufacturer.

- **The rig provides an environment that allows commercial probes to be evaluated over the entire particle size range of AMTD.**

Laser diffraction particle size distributions generated in this work show the entire range of particles sizes in the reference particles size distribution is present in the flow rig. This is demonstrated in DoE3 data where particle size distributions of particles from the rig plume are very similar to that of AMTD, as received.

- **The rig is suitable for guiding the development of commercial, real-time sensors for monitoring material ingestion into gas turbine engines.**

The combination of a rig with environments simulating gas turbine engine conditions; models of particle size and concentration, as functions of flow velocity, particle feed rate, and measurement location; and the presence of particles spanning the entire distribution of AMTD, make the rig suitable for guiding the development of commercial particle ingestion monitoring probes. Models based on Mie theory (DoE1 and DoE2) and Fraunhofer (DoE3) are available.

6.3 Recommendations

- The current rig configuration with horizontal flow, vertical particle injection, and 26.7 mm diameter pipe is deemed appropriate for commercial probe evaluations. Horizontal particle injection and reduced rig diameters should be avoided because particle agglomeration increases in these rig configurations.

- To further visualize the particle segregation and dispersion, develop a 2-dimensional map of the entire particle size distribution across the rig profile, whereby line of sight data are converted to spatially resolved data.

- To confirm findings in this study, use highspeed imaging to identify whether size dependent particle segregation across the rig profile exists. Determine whether large particles are primarily located at the centerline, and small particles are well dispersed within the rig profile. Also, determine whether these patterns change at increased flow velocities between 100 m/s and 200 m/s.

- Using highspeed images, measure particle dimensions across the entire rig profile. Convert data into particle size distributions to compare to laser diffraction data acquired in this work.

REFERENCES

[1] A. A. Hamed, W. Tabakoff, R. B. Rivir, K. Das, and P. Arora, “Turbine Blade Surface Deterioration by Erosion,” *J. Turbomach.*, vol. 127, no. July 2005, pp. 445–452, 2005.

[2] W. Tabakoff, A. Hamed, and M. Metwally, “Effect of Particle Size Distribution on Particle Dynamics and Blade Erosion in Axial Flow Turbines,” vol. 113, no. October 1991, pp. 607–615, 1991.

[3] A. Vogel, A. J. Durant, M. Cassiani, R. J. Clarkson, M. Slaby, and A. Stohl, “Simulation of Volcanic Ash Ingestion Into a Large Aero Engine : Particle – Fan Interactions,” vol. 141, no. January, pp. 1–12, 2019.

[4] K. Brun, M. Nored, and R. Kurz, “Particle Transport Analysis of Sand Ingestion in Gas Turbine Engines,” vol. 134, no. January, pp. 1–8, 2012.

[5] P. Mechnich, W. Braue, and U. Schulz, “High-Temperature Corrosion of EB-PVD Yttria Partially Stabilized Zirconia Thermal Barrier Coatings with an Artificial Volcanic Ash Overlay,” vol. 931, no. 28205, pp. 925–931, 2011.

[6] W. L. Cheng and B. Guo, “A Numerical Study of Dust Deposition in a Model Turbine Vane Cooling Passage,” pp. 1–9, 2019.

[7] N. Bojdo and A. Filippone, “A Simple Model to Assess the Role of Dust Composition and Size on Deposition in Rotorcraft Engines,” 2019.

[8] A. Boulanger, H. Patel, J. Hutchinson, W. Deshong, W. Ng, and S. Ekkad, “Preliminary Experimental Investigation of Initial Onset of Sand Deposition in the Turbine Section of Gas Turbines,” pp. 1–10, 2019.

[9] A. Hamed and W. Tabakoff, “Erosion and Deposition in Turbomachinery,” vol. 22, no. 2, pp. 350–360, 2006.

[10] N. D. Cardwell, K. A. Thole, and S. W. Burd, “Investigation of Sand Blocking Within Impingement and Film-Cooling Holes,” *J. Turbomach.*, vol. 132, no. April 2010, pp. 1–10, 2010.

[11] W. Walsh, K. Thole, and C. Joe, “EFFECTS OF SAND INGESTION ON THE BLOCKAGE OF FILM-COOLING HOLES,” *ASME Turbo Expo*, pp. 1–10, 2006.

[12] S. M. Whitaker, B. Peterson, A. F. Miller, and J. P. Bons, “The Effect of Particle Loading, Size, and Temperature on Deposition in a Vane Leading Edge Impingement Cooling Geometry,” *ASME Turbo Expo*, pp. 1–14, 2016.

[13] C. A. Wood, S. L. Slater, M. Zonneveldt, J. Thornton, N. Armstrong, and R. A. Antoniou, “Characterisation of Dirt , Dust and Volcanic Ash : A Study on the Potential for Gas Turbine Engine Degradation.”

[14] L. Obringer, “NASA, Flight and Ground Experimental Test Technologies,” 2017. [Online]. Available: https://www.nasa.gov/feature/flight-and-ground-experimental-test-technologies-0.

[15] J. Dean, C. Taltavull, and T. W. Clyne, “Influence of the composition and viscosity of volcanic ashes on their adhesion within gas turbine aeroengines,” *Acta Mater.*, vol. 109, no. 2016, pp. 8–16, 2016.

[16] B. M. Shinozaki, K. A. Roberts, B. Van De Goor, and T. W. Clyne, “Deposition of Ingested Volcanic Ash on Surfaces in the Turbine of a Small Jet Engine,” no. 10, pp. 986–994, 2013.

[17] M. Kostoglou and A. G. Konstandopoulos, “Particulate Deposit Shape Evolution on Cylinders in Cross-Flow at High Stokes Numbers,” vol. 31, no. 4, pp. 427–436, 2000.

[18] S. M. Scala, M. Konrad, R. B. Mason, J. Semick, and D. Skelton, “Sensor Requirements to Monitor the Real Time Performance of a Gas Turbine Engine Undergoing Compressor Blade Erosion,” *AIAA*, no. July, 2004.

[19] G. Papadopoulos, D. Bivolaru, and J. Lin, “Real Time Gas Turbine Engine Particulate Ingestion Sensor for Particle Size and Composition,” *ASME Turbo Expo*, 2018.

[20] J. D. Weickert, G. Griffin, J. R. Noel, and C. Rickards, “US9714967 United States Patent,” vol. 1, no. 12, 2017.

[21] R. M. Carter, Y. Yan, and S. D. Cameron, “On-line measurement of particle size distribution and mass flow rate of particles in a pneumatic suspension using combined imaging and electrostatic sensors,” vol. 16, pp. 309–314, 2005.

[22] J. Delimont, M. K. Murdock, W. Ng, and S. Ekkad, “Effect of Temperature on Microparticle Rebound Characteristics at Constant Impact Velocity — Part II,” vol. 137, no. November 2015, 2018.

[23] J. W. Jensen, S. W. Squire, J. P. Bons, and T. H. Fletcher, “Simulated Land-Based Turbine Deposits Generated in an,” vol. 127, no. July, 2005.

[24] D. Modarress, H. Tan, and S. Elghobashij, “Two-Component LDA Measurement in a Two-Phase Turbulent Jet,” *AIAA*, vol. 22, no. 5, pp. 624–630.

[25] M. Sommerfeld, “Analysis of collision effects for turbulent gas – particle flow in a horizontal channel : Part I . Particle transport,” vol. 29, pp. 675–699, 2003.

[26] K. O. Fong, O. Amili, and F. Coletti, “Velocity and spatial distribution of inertial particles in a turbulent channel flow,” pp. 367–406, 2019.

[27] B. Van Wachem, M. Zastawny, F. Zhao, and G. Mallouppas, “International Journal of Multiphase Flow Modelling of gas – solid turbulent channel flow with non-spherical particles with large Stokes numbers,” *Int. J. Multiph. FLOW*, vol. 68, pp. 80–92, 2015.

[28] J. Westerweel, G. E. Elsinga, and R. J. Adrian, “Particle Image Velocimetry for Complex and Turbulent Flows,” *Annu. Rev. Fluid Mech.*, vol. 45, pp. 409–436, 2013.

[29] C. Tu, Z. Yin, J. Lin, and F. Bao, “applied sciences A Review of Experimental Techniques for Measuring Micro- to Nano-Particle-Laden Gas Flows,” 2017.

[30] U. Ulusoy and C. Igathinathane, “Particle size distribution modeling of milled coals by dynamic image analysis and mechanical sieving,” *Fuel Process. Technol.*, vol. 143, pp. 100–109, 2016.

[31] C. Di Stefano, V. Ferro, and S. Mirabile, “Comparison between grain-size analyses using laser diffraction and sedimentation methods,” *Biosyst. Eng.*, vol. 106, no. 2, pp. 205–215, 2010.

[32] R. N. Kelly and J. Kazanjian, “Commercial Reference Shape Standards Use in the Study of Particle Shape Effect on Laser Diffraction Particle Size Analysis,” *AAPS PharmSciTech*, vol. 7, no. 2, 2006.

[33] N. Vlachos and I. T. H. Chang, “Graphical and statistical comparison of various size distribution measurement systems using metal powders of a range of sizes and shapes Graphical and statistical comparison of various size distribution measurement systems using metal powders of a range o,” *Powder Metall.*, vol. 54, no. 4, pp. 497–506, 2013.

[34] S. J. Blott and K. Pye, “Particle size distribution analysis of sand-sized particles by laser diffraction : an experimental investigation of instrument sensitivity and the effects of particle shape,” *Sedimentology*, vol. 53, pp. 671–685, 2006.

[35] V. G. Farafonov, V. B. Il, M. S. Prokopjeva, A. R. Tulegenov, and V. I. Ustimov, “A Spheroidal Model of Light Scattering by Nonspherical Particles,” *Phys. Opt.*, vol. 126, no. 4, pp. 443–449, 2019.

[36] A. K. Li, V. McDonell, M. Venaas, G. A. Waldherr, and H. Lin, “DESIGN AND EVALUATION OF A FIBER OPTIC SENSOR FOR PARTICLE AND,” no. Lii, pp. 1–10, 2019.

[37] H. Lin and G. A. Waldherr, "US10359350 United States Patent," vol. 1, 2019.

[38] G. E. Klinzing, F. Rizk, R. Marcus, and L. S. Leung, *Pneumatic Conveying of Solids*, 3rd ed. Springer, 2010.

[39] G. C. Rapp and S. H. Rosenthal, "Problems and Solutions for Sand Environment Operation of Helicopter Gas Turbines Problems and Solutions for Sand Environment Operation of Helicopter Gas Turbines," pp. 1–16, 1969.

[40] D. L. Black, M. Q. Mcquay, and M. P. Bonin, "LASER-BASED TECHNIQUES FOR PARTICLE-SIZE MEASUREMENT : A REVIEW OF SIZING METHODS A N D THEIR INDUSTRIAL APPLICATIONS," vol. 22, no. 96, pp. 267–306, 1996.

[41] A. F. Rawle, "Best practice in laser diffraction – a robustness study of the optical properties of silica," *Procedia Eng.*, vol. 102, pp. 182–189, 2015.

[42] T. T. Allen, *Introduction to Engineering Statistics and Six Sigma*. 2006.

[43] V. P. Astakhov, "Design of Experiment Methods in Manufacturing: Basics and Practical Applications. In: Davim J.P. (eds) Statistical and Computational Techniques in Manufacturing," Springer, 2012.

[44] L. Chen, Z. Liu, P. Sun, and W. Huo, "Formulation of a fuel spray SMD model at atmospheric pressure using Design of Experiments (DoE)," *FUEL*, vol. 153, pp. 355–360, 2015.

[45] R. K. Nekouei, F. Rashchi, and A. A. Amadeh, "Using design of experiments in synthesis of ultra- fine copper particles by electrolysis," *Powder Technol.*, vol. 237, pp. 165–171, 2013.

[46] P. A. Shamlou, *Handling of Bulk Solids*. .

[47] Y. Cengel and J. Cimbala, "Fundamentals of Fluid Mechanics," pp. 321–398.

[48] H. Zhang *et al.*, "Effect of collisions on the particle behavior in a turbulent square duct flow," *Powder Technol.*, vol. 269, pp. 320–336, 2015.

[49] P. L. Johnson, M. Bassenne, and P. Moin, "Turbophoresis of small inertial particles : theoretical considerations and application to wall-modelled large-eddy simulations," vol. 883, no. A27, pp. 1–38, 2020.

[50] S. L. Soo and J. A. Regalbuto, "Concentration Distribution in Two-Phase Pipe Flow," *Can. J. Chem. Eng.*, pp. 160–166, 1960.

[51] R. Israel and D. E. Rosner, “Use of a Generalized Stokes Number to Determine the Aerodynamic Capture Efficiency of Non- Stokesian Particles from a Compressible Gas Flow Use of a Generalized Stokes Number to Determine the Aerodynamic Capture Efficiency of Non-Stokesian Particles from,” *Aerosol Sci. Technol.*, 1983.

[52] F. Salehi, M. J. Cleary, A. R. Masri, and A. Kronenburg, “International Journal of Multiphase Flow PDF-PBE modelling of polydisperse inertial particles in a turbulent recirculating flow,” *Int. J. Multiph. Flow*, vol. 117, pp. 42–52, 2019.

APPENDIX

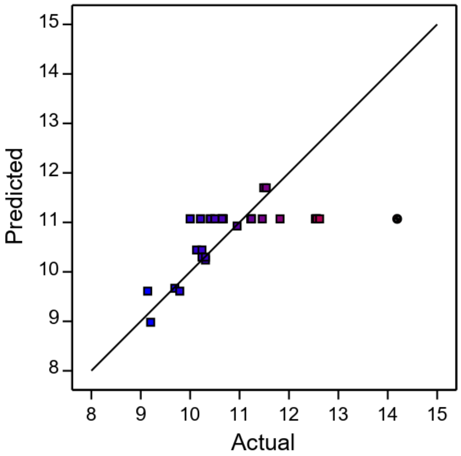

Figure 92. Predicted versus actual DoE3 Dv50 model points.

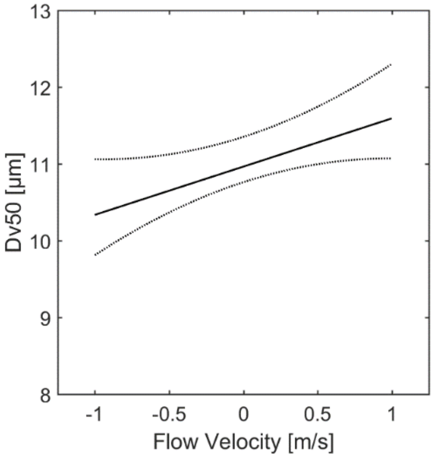

Figure 93. Main effect plot of DoE3 Dv50 versus flow velocity.

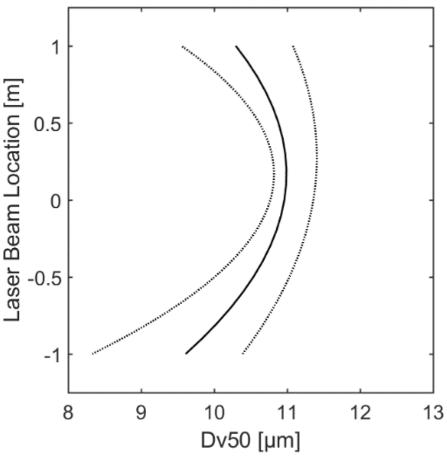

Figure 94. Main effect plot of DoE3 Dv50 versus laser beam location.

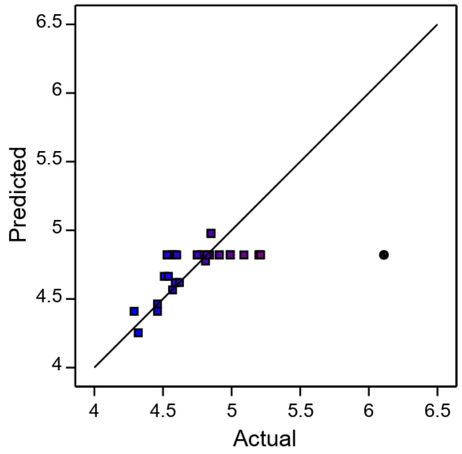

Figure 95. Predicted versus actual DoE3 D32 model points.

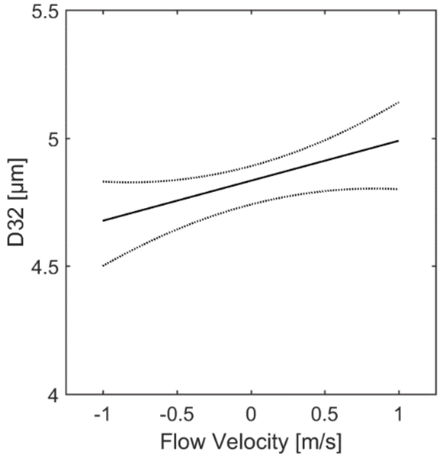

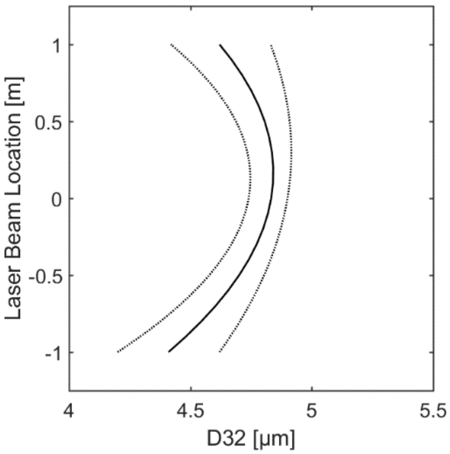

Figure 96. Main effect plot of DoE3 D32 versus flow velocity.

Figure 97. Main effect plot of DoE3 D32 versus flow velocity.

Source	Sum of Squares	df	Mean Square	F-value	p-value	
Model	241.84	5	48.37	9.13	0.0017	significant
A: Flow Velocity	110.62	1	110.62	20.89	0.0010	
B: Laser Beam Location	3.75	1	3.75	0.7088	0.4195	
C: Feed Rate	27.48	1	27.48	5.19	0.0459	
D: Ejector Pressure	70.69	1	70.69	13.35	0.0044	
AB	29.30	1	29.30	5.53	0.0405	
Residual	52.96	10	5.30			
Cor Total	294.80	15				

Table 13. F-test statistics for transmission in DoE1.

Statistical Parameter	Value
Std. Dev.	2.30
Mean	94.09
C.V. %	2.45
R^2	0.8203
Adjusted R^2	0.7305
Predicted R^2	0.5401
Adeq Precision	10.4945

Table 14. Regression statistics for transmission in DoE1.

Source	Sum of Squares	df	Mean Square	F-value	p-value	
Model	5.96	3	1.99	49.90	< 0.0001	significant
A: Flow Velocity	1.97	1	1.97	49.56	< 0.0001	
B: Laser Beam Location	0.5751	1	0.5751	14.45	0.0029	
C: Feed Rate	3.03	1	3.03	76.19	< 0.0001	
Residual	0.4377	11	0.0398			
Cor Total	6.40	14				

Table 15. F-test statistics for Dv10 in DoE1.

Statistical Parameter	Value
Std. Dev.	0.1995
Mean	4.71
C.V. %	4.23
R^2	0.9316
Adjusted R^2	0.9129
Predicted R^2	0.8748
Adeq Precision	19.7225

Table 16. Table 16. Regression statistics for Dv10 in DoE1.

Source	Sum of Squares	df	Mean Square	F-value	p-value	
Model	1178.07	3	392.69	4.77	0.0258	significant
A: Flow Velocity	754.63	1	754.63	9.17	0.0127	
B: Laser Beam Location	98.96	1	98.96	1.20	0.2986	
AB	370.54	1	370.54	4.50	0.0599	
Residual	823.33	10	82.33			
Cor Total	2001.40	13				

Table 17. F-test statistics for Dv50 in DoE1.

Statistical Parameter	Value
Std. Dev.	9.07
Mean	25.56
C.V. %	35.49
R^2	0.5886
Adjusted R^2	0.4652
Predicted R^2	0.1863
Adeq Precision	5.2023

Table 18. Table 16. Regression statistics for Dv50 in DoE1.

Source	Sum of Squares	df	Mean Square	F-value	p-value	
Model	59.81	6	9.97	9.69	0.0042	significant
A: Flow Velocity	23.07	1	23.07	22.43	0.0021	
B: Laser Beam Location	22.76	1	22.76	22.13	0.0022	
D: Ejector Pressure	2.14	1	2.14	2.08	0.1920	
E: Rig Length	2.52	1	2.52	2.45	0.1617	
AB	9.29	1	9.29	9.04	0.0198	
DE	10.68	1	10.68	10.38	0.0146	
Residual	7.20	7	1.03			
Cor Total	67.01	13				

Table 19. F-test statistics for D32 in DoE1.

Statistical Parameter	Value
Std. Dev.	1.01
Mean	9.49
C.V. %	10.68
R^2	0.8925
Adjusted R^2	0.8004
Predicted R^2	0.5931
Adeq Precision	10.8818

Table 20. Table 16. Regression statistics for Dv90 in DoE1.

Source	Sum of Squares	df	Mean Square	F-value	p-value	
Model	228.22	4	57.05	4.11	0.0177	significant
A: Flow Velocity	131.14	1	131.14	9.45	0.0073	
B: Laser Beam Location	17.08	1	17.08	1.23	0.2836	
C: Feed Rate	17.58	1	17.58	1.27	0.2769	
C^2	62.41	1	62.41	4.50	0.0499	
Residual	221.97	16	13.87			
Lack of Fit	47.50	8	5.94	0.2723	0.9580	insignificant
Pure Error	174.47	8	21.81			
Cor Total	450.19	20				

Table 21. F-test statistics for transmission in DoE2.

Statistical Parameter	Value
Std. Dev.	3.72
Mean	85.27
C.V. %	4.37
R^2	0.5069
Adjusted R^2	0.3837
Predicted R^2	0.3047
Adeq Precision	8.0284

Table 22. Regression statistics for transmission in DoE2.

Source	Sum of Squares	df	Mean Square	F-value	p-value	
Model	0.3428	3	0.1143	9.28	0.0007	significant
A: Flow Velocity	0.0450	1	0.0450	3.65	0.0730	
B: Laser Beam Location	0.1682	1	0.1682	13.66	0.0018	
AB	0.1296	1	0.1296	10.52	0.0048	
Residual	0.2094	17	0.0123			
Lack of Fit	0.0778	9	0.0086	0.5258	0.8212	insignificant
Pure Error	0.1316	8	0.0164			
Cor Total	0.5522	20				

Table 23. F-test statistics for Dv10 in DoE2.

Statistical Parameter	Value
Std. Dev.	0.1110
Mean	4.22
C.V. %	2.63
R^2	0.1110
Adjusted R^2	4.22
Predicted R^2	2.63
Adeq Precision	13.4199

Table 24. Regression statistics for Dv10 in DoE2.

Source	Sum of Squares	df	Mean Square	F-value	p-value	
Model	16.92	3	5.64	21.32	< 0.0001	significant
A: Flow Velocity	1.02	1	1.02	3.84	0.0667	
B: Laser Beam Location	7.22	1	7.22	27.29	< 0.0001	
B^2	8.69	1	8.69	32.84	< 0.0001	
Residual	4.50	17	0.2645			
Lack of Fit	1.91	9	0.2122	0.6560	0.7290	insignificant
Pure Error	2.59	8	0.3234			
Cor Total	21.42	20				

Table 25. F-test statistics for Dv50 in DoE2.

Statistical Parameter	Value
Std. Dev.	0.5143
Mean	12.08
C.V. %	4.26
R^2	0.7901
Adjusted R^2	0.7530
Predicted R^2	0.6733
Adeq Precision	13.3067

Table 26. Regression statistics for Dv50 in DoE2.

Source	Sum of Squares	df	Mean Square	F-value	p-value	
Model	38.21	3	12.74	5.38	0.0087	significant
A: Flow Velocity	2.98	1	2.98	1.26	0.2780	
B: Laser Beam Location	9.16	1	9.16	3.87	0.0658	
B^2	26.08	1	26.08	11.00	0.0041	
Residual	40.28	17	2.37			
Lack of Fit	13.86	9	1.54	0.4662	0.8616	insignificant
Pure Error	26.43	8	3.30			
Cor Total	78.50	20				

Table 27. F-test statistics for Dv90 in DoE2.

Statistical Parameter	Value
Std. Dev.	1.54
Mean	54.60
C.V. %	2.82
R^2	0.4868
Adjusted R^2	0.3962
Predicted R^2	0.2992
Adeq Precision	6.8239

Table 28. Regression statistics for Dv90 in DoE2.

Source	Sum of Squares	df	Mean Square	F-value	p-value	
Model	1.23	3	0.4112	10.10	0.0005	significant
A: Flow Velocity	0.1596	1	0.1596	3.92	0.0641	
B: Laser Beam Location	0.7260	1	0.7260	17.84	0.0006	
AB	0.3481	1	0.3481	8.55	0.0095	
Residual	0.6919	17	0.0407			
Lack of Fit	0.2472	9	0.0275	0.4941	0.8430	insignificant
Pure Error	0.4447	8	0.0556			
Cor Total	1.93	20				

Table 29. F-test statistics for D32 in DoE2.

Statistical Parameter	Value
Std. Dev.	0.2017
Mean	7.35
C.V. %	2.75
R^2	0.6407
Adjusted R^2	0.5773
Predicted R^2	0.5337
Adeq Precision	13.5442

Table 30. Regression statistics for D32 in DoE2.

Source	Sum of Squares	df	Mean Square	F-value	p-value	
Model	23.64	3	7.88	14.55	< 0.0001	significant
B: Laser Beam Location	9.35	1	9.35	17.27	0.0007	
C: Feed Rate	1.04	1	1.04	1.91	0.1844	
B^2	13.25	1	13.25	24.46	0.0001	
Residual	9.21	17	0.5417			
Lack of Fit	2.58	9	0.2863	0.3453	0.9330	insignificant
Pure Error	6.63	8	0.8291			
Cor Total	32.85	20				

Table 31. F-test statistics for D43 in DoE2.

Statistical Parameter	Value
Std. Dev.	0.7360
Mean	21.63
C.V. %	3.40
R^2	0.7197
Adjusted R^2	0.6702
Predicted R^2	0.6227
Adeq Precision	10.6996

Table 32. Regression statistics for D43 in DoE2.

Source	Sum of Squares	df	Mean Square	F-value	p-value	
Model	232.45	2	116.22	12.79	0.0002	significant
A: Flow Velocity	163.53	1	163.53	18.00	0.0003	
C: Feed Rate	68.91	1	68.91	7.59	0.0110	
Residual	218.05	24	9.09			
Lack of Fit	67.81	10	6.78	0.6319	0.7649	insignificant
Pure Error	150.24	14	10.73			
Cor Total	450.50	26				

Table 33. F-test statistics for transmission in DoE3.

Statistical Parameter	Value
Std. Dev.	3.01
Mean	87.69
C.V. %	3.44
R^2	0.5160
Adjusted R^2	0.4756
Predicted R^2	0.3967
Adeq Precision	14.8422

Table 34. Regression statistics for transmission in DoE3.

Source	Sum of Squares	df	Mean Square	F-value	p-value	
Model	0.0955	3	0.0318	4.97	0.0083	significant
A: Flow Velocity	0.0136	1	0.0136	2.13	0.1582	
B: Laser Beam Location	0.0098	1	0.0098	1.53	0.2284	
B^2	0.0721	1	0.0721	11.26	0.0027	
Residual	0.1472	23	0.0064			
Lack of Fit	0.0321	9	0.0036	0.4332	0.8952	insignificant
Pure Error	0.1151	14	0.0082			
Cor Total	0.2427	26				

Table 35. F-test statistics for Dv10 in DoE3.

Statistical Parameter	Value
Std. Dev.	0.0800
Mean	1.61
C.V. %	4.97
R^2	0.3935
Adjusted R^2	0.3144
Predicted R^2	0.2773
Adeq Precision	7.4909

Table 36. Regression statistics for Dv10 in DoE3.

Source	Sum of Squares	df	Mean Square	F-value	p-value	
Model	9.84	3	3.28	6.62	0.0022	significant
A: Flow Velocity	3.16	1	3.16	6.38	0.0189	
B: Laser Beam Location	0.9453	1	0.9453	1.91	0.1806	
B^2	5.74	1	5.74	11.57	0.0025	
Residual	11.40	23	0.4958			
Lack of Fit	0.3881	9	0.0431	0.0548	0.9999	insignificant
Pure Error	11.02	14	0.7868			
Cor Total	21.25	26				

Table 37. F-test statistics for Dv50 in DoE3.

Statistical Parameter	Value
Std. Dev.	0.7041
Mean	10.66
C.V. %	6.60
R^2	0.4633
Adjusted R^2	0.3933
Predicted R^2	0.3892
Adeq Precision	9.6327

Table 38. Regression statistics for Dv50 in DoE3.

Source	Sum of Squares	df	Mean Square	F-value	p-value	
Model	0.8553	3	0.2851	8.06	0.0008	significant
A: Flow Velocity	0.1953	1	0.1953	5.52	0.0278	
B: Laser Beam Location	0.0882	1	0.0882	2.49	0.1281	
B^2	0.5717	1	0.5717	16.16	0.0005	
Residual	0.8139	23	0.0354			
Lack of Fit	0.1322	9	0.0147	0.3017	0.9618	insignificant
Pure Error	0.6817	14	0.0487			
Cor Total	1.67	26				

Table 39. Table 37. F-test statistics for D32 in DoE3.

Statistical Parameter	Value
Std. Dev.	0.1881
Mean	4.74
C.V. %	3.97
R^2	0.5124
Adjusted R^2	0.4488
Predicted R^2	0.4260
Adeq Precision	10.1674

Table 40. Regression statistics for D32 in DoE3.